PNNL-14907

Pacific Northwest
National Laboratory
Operated by Battelle for the
U.S. Department of Energy

# Vadose Zone Contaminant Fate-and-Transport Analysis for the 216-B-26 Trench

A. L. Ward
G.W. Gee
Z. F. Zhang
J. M. Keller

October 2004


Prepared for the U.S. Department of Energy
under Contract DE-AC05-76RL01830

## DISCLAIMER



PACIFIC NORTHWEST NATIONAL LABORATORY
*operated by*
BATTELLE
*for the*
UNITED STATES DEPARTMENT OF ENERGY
*under Contract DE-ACO5-76RL01830*

**Printed in the United States of America**

**Available to DOE and DOE contractors from the**
**Office of Scientific and Technical Information,**
**P.O. Box 62, Oak Ridge, TN 37831-0062;**
**ph: (865) 576-8401**
**fax: (865) 576 5728**
**email: reports@adonis.osti.gov**

**Available to the public from the National Technical Information Service,**
**U.S. Department of Commerce, 5285 Port Royal Rd., Springfield, VA 22161**
**ph: (800) 553-6847**
**fax: (703) 605-6900**
**email: orders@nits.fedworld.gov**
**online ordering: http://www.ntis.gov/ordering.htm**

PNNL-14907

# Vadose Zone Contaminant Fate-and-Transport Analysis for the 216-B-26 Trench

A. L. Ward
G.W. Gee
Z. F. Zhang
J. M. Keller

October 2004

Prepared for
the U.S. Department of Energy
under Contract DE-AC05-76RL01830

Pacific Northwest National Laboratory
Richland, Washington 99352

# Summary

The BC cribs and trenches in Hanford's 200 Area are believed to have received about 30 Mgal of scavenged tank waste containing an estimated 400 Ci of $^{99}Tc$ as well as large quantities of $NO_3^-$ and $^{238}U$. Owing to the potential risk, remediation is being accelerated at this site. Developing an effective remediation plan and evaluating remedial options for the site requires a detailed analysis of fate and transport for this site and such an analysis must rely on numerical modeling. The purpose of this study was to develop a conceptual model for contaminant fate and transport at the 216-B-26 Trench site to allow interpretation of the current contaminant distributions and to support identification, development, and evaluation of remediation alternatives.

In developing the conceptual model, the presence of large concentrations of $^{99}Tc$ high above the water table implicated stratigraphy in the control of the downward migration. The resulting conceptual model therefore included 1) small-scale stratigraphy and changes in physical and chemical properties, 2) tilted layers to accommodate the natural slope to the formation, and 3) lateral spreading along multiple strata with contrasting physical properties. Flow and transport properties were derived using physically based pedotransfer functions that were coupled with high-resolution neutron moisture logs taken on a vertical spacing of 0.076 m. Heterogeneity in the longitudinal and transverse horizontal directions was incorporated by using geostatistical methods to overlay the spatial correlation structure of flow variables from the well-characterized 299-E24-111 test site on to the simulation domain. Two approaches were used to compare no-action and capping remedial alternatives. The first approach, based on a simple analytical convolution solution to the convective-dispersive equation, assumed steady downward flow and allowed for spatially averaged or variable water content. This approach was combined with a soil screening protocol to calculate soil screening levels (Tables S1 and S2) and contaminant concentrations reaching hypothetical receptors down gradient of the site. In the second approach the STOMP simulator was used to predict contaminant transport through the vadose zone and into a 5-m thick confined aquifer during transient multidimensional flow.

Both modeling approaches show that leachate concentrations reaching the water table would exceed the MCLs under the no-action alternatives with hypothetical recharge rates of 25 and 3.5 mm/yr. Soil screening levels were exceeded under the no-action alternatives and concentrations of mobile contaminants reaching hypothetical receptor wells consistently exceeded the MCLs (Tables S3 and S4). Owing to the large inventory of $^{99}Tc$ and $NO_3^-$, the high mobility of the two contaminants, and the long half life of $^{99}Tc$, additional measures appear necessary to meet the appropriate soil screening levels. In this respect, on-site capping was evaluated simply by reducing surface recharge to mimic the design performance of hypothetical surface barriers. Both modeling approaches show capping to be an effective technology for remediating the site. Capping successful removed the threat to ground water through a reduction in mass flux to the water table and an increase in residence time in the vadose zone. Consequently, soil screening levels increased and concentrations reaching down-gradient receptor wells declined below the MCLs with three hypothetical caps designed to limit recharge to 0.5, 0.1, and 0 mm/yr. Summaries of arrival times and concentrations at the water table and receptor wells for $^{99}Tc$ and $NO_3^-$ are provided in Tables S3 and S4 respectively.

**Table S1. Soil Screening Levels for $^{99}Tc$ as a Function of Recharge Rate and Distance L to a Receptor Well**

| Recharge Rate (mm/yr) | Soil Screening Level (pCi/g) | | | |
|---|---|---|---|---|
| | L=1 m | L=10 m | L=100 m | L =1000 m |
| 25.0 | 4.50E+00 | 1.37E+01 | 4.29E+01 | 1.35E+02 |
| 3.5 | 3.07E+01 | 9.68E+01 | 3.05E+02 | 9.62E+02 |
| 0.5 | 2.14E+02 | 6.73E+02 | 2.13E+03 | 6.73E+03 |
| 0.1 | 1.07E+03 | 3.37E+03 | 1.07E+04 | 3.32E+04 |

**Table S2. Soil Screening Levels for $NO_3^-$ as a Function of Recharge Rate and Distance L to a Receptor Well**

| Recharge Rate (mm/yr) | Soil Screening Level (mg/g) | | | |
|---|---|---|---|---|
| | L=1 m | L=10 m | L=100 m | L =1000 m |
| 25.0 | 5.00E-02 | 1.52E-01 | 4.76E-01 | 1.50E+00 |
| 3.5 | 3.41E-01 | 1.07E+00 | 3.39E+00 | 1.07E+01 |
| 0.5 | 2.37E+00 | 7.48E+01 | 2.37E+01 | 7.48E+01 |
| 0.1 | 1.19E+01 | 3.74E+01 | 1.12E+03 | 3.69E+02 |

**Table S3. STOMP-Predicted Arrival Times and Concentrations for $^{99}Tc$ at the Water Table and a Hypothetical Receptor Well Located 100 m Down-gradient of the Trench Site**

| Point of Compliance | Solute | Recharge Rate (mm/yr) | First Arrival (yr) | MCL Arrival Time (yr) | Peak Arrival Time (yr) | Peak Concentration (pCi/L) | Mean Arrival Time (yr) |
|---|---|---|---|---|---|---|---|
| Receptor Well | $Tc^{99}$ | 25.0 | 2118.67 | 2142.46 | 2228.50 | 2.09E+04 | 2227.24 |
| | $Tc^{99}$ | 3.5 | 2353.67 | 2600.40 | 2991.50 | 3.15E+03 | 2977.98 |
| | $Tc^{99}$ | 0.5 | 2660.19 | NA | 5975.00 | 4.58E+02 | 5857.26 |
| | $Tc^{99}$ | 0.1 | 2740.01 | NA | 3573.00 | 1.15E+02 | 7034.05 |
| | $Tc^{99}$ | 0.0 | 2761.24 | NA | 3441.00 | 1.09E+02 | >8000.00 |
| Water Table | $Tc^{99}$ | 25.0 | 2095.13 | 2113.36 | 2228.31 | 3.68E+05 | 2228 |
| | $Tc^{99}$ | 3.5 | 2127.68 | 2199.60 | 2991.31 | 3.83E+05 | 2991 |
| | $Tc^{99}$ | 0.5 | 2128.40 | 2205.42 | 5974.30 | 3.88E+05 | 5974 |
| | $Tc^{99}$ | 0.1 | 2129.02 | 2206.46 | >12005 | 3.84E+05 | >8000 |
| | $Tc^{99}$ | 0.0 | 2129.05 | 2206.59 | >12005 | 4.11E+05 | >8000 |

NA—not achieved by the end of the simulation.

**Table S4. STOMP-Predicted Arrival Times and Concentrations for $NO_3^-$ at the Water Table and a Hypothetical Receptor Well Located 100 m Down-gradient of the Trench Site**

| Point of Compliance | Solute | Recharge Rate (mm/yr) | First Arrival (yr) | MCL Arrival Time (yr) | Peak Arrival Time (yr) | Peak Concentration (mg/g) | Mean Arrival Time (yr) |
|---|---|---|---|---|---|---|---|
| Receptor Well | $NO_3^-$ | 25.0 | 2105.77 | 2125.80 | 2228.50 | 1.09E+03 | 2227.23 |
| | $NO_3^-$ | 3.5 | 2237.17 | 2420.39 | 2991.50 | 1.65E+02 | 2978.11 |
| | $NO_3^-$ | 0.5 | 2263.83 | 3640.35 | 5982.00 | 2.43E+01 | 5865.82 |
| | $NO_3^-$ | 0.1 | 2266.29 | NA | 3590.50 | 6.02E+00 | 7062.64 |
| | $NO_3^-$ | 0.0 | 2266.86 | NA | 3453.50 | 5.74E+00 | >8000.00 |
| Water Table | $NO_3^-$ | 25.0 | 2084.37 | 2100.97 | 2228.31 | 1.93E+04 | 2227.24 |
| | $NO_3^-$ | 3.5 | 2100.12 | 2146.82 | 2991.31 | 2.01E+04 | 2977.98 |
| | $NO_3^-$ | 0.5 | 2100.59 | 2148.88 | 5982.31 | 2.06E+04 | 5857.26 |
| | $NO_3^-$ | 0.1 | 2100.64 | 2149.07 | >12005 | 2.07E+04 | 7034.26 |
| | $NO_3^-$ | 0.0 | 2100.65 | 2149.12 | >12005 | 2.22E+04 | >8000 |

NA—not achieved by the end of the simulation.

# Glossary

| | |
|---|---|
| 1-D, 2-D, 3-D | One, Two, or Three Dimensional |
| ARARS | applicable or relevant and appropriate requirements |
| CDE | convective dispersive equation |
| CEC | cation exchange capacity |
| CERCLA | Comprehensive Environmental Response, Compensation and Liability Act of 1980 |
| COC | contaminants of concern |
| DAF | dilution attenuation factor |
| DOE | U.S. Department of Energy |
| DOE-RL | U.S. Department of Energy-Richland Operations |
| Eh | Reduction-oxidation Potential |
| EMSL | Environmental and Molecular Sciences Laboratory |
| EPA | U.S. Environmental Protection Agency |
| FS | feasibility study |
| ILAW | immobilized low-activity waste |
| MCL | maximum contaminant level |
| MNA | monitored natural attenuation |
| OU | Operable Unit |
| PET | potential evapotranspiration |
| PETSc | Portable Extensible Toolkit for Scientific Computation |
| PNNL | Pacific Northwest National Laboratory |
| pH | Concentration of hydrogen ions (protons) in solution |
| REDOX | reduction oxidation |
| RI | Remedial Investigation |

| | |
|---|---|
| SPLIB | library of iterative methods for sparse linear systems |
| SSL | soil-screening level |
| STOMP | Subsurface Transport Over Multiple Phases (simulator) |
| SVOC | semi volatile organic compound |

# Acknowledgements

Funding for this study was provided to Pacific Northwest National Laboratory under work order by Fluor Hanford (FH). The FH point of contact was Mark Benecke. The conceptual model was developed under the FY 2004 Vadose Zone Transport Field Studies managed by Glendon Gee. The Vadose Zone Transport Field Studies are a subtask of the Remediation and Closure Science Project managed by Mark Freshley. Thanks to Ray Clayton, David Lanigan, and Bruce Bjornstad for help in data collection; to Yi-Ju Chen and Chris Murray for their contribution to the incorporation of the spatial correlation structure into the stratigraphic model derived from the C4191 borehole. Pacific Northwest National Laboratory is operated for the U.S. Department of Energy by Battelle under Contract DE-AC06-76RL01830.

# Contents

# Figures

# Tables

# 1.0 Introduction

The BC cribs and trenches form a group of liquid waste disposal sites located south of the 200 East Area of the Hanford Site. This group of disposal sites includes 28 waste sites from the 200-TW-1 operable unit, 4 waste sites formerly in the 200-LW-1 operable unit, and 2 unplanned release waste sites from the 200-UR-1 operable unit. The 200-TW-1 operable unit waste sites received scavenged waste from the uranium recovery and ferrocyanide processes at the 221/224-U Plant, which recovered the uranium from the metal-waste streams at the B and T Plants. The former 200-LW-1 operable unit waste sites received liquid waste from 300 Area laboratory operations and from a 1965 disruption at the Plutonium Recycle Test Reactor. Significant amounts of radionuclides, including uranium, plutonium, and fission products, were released to these waste sites.

Waste discharges to this site contributed perhaps the largest liquid fraction of contaminants to the ground in the 200 Areas. The 200-TW-1 OU waste sites in the BC cribs and trenches area received approximately 30 Mgal of scavenged tank waste, with possibly the largest inventory of $^{99}$Tc ever disposed to the soil at Hanford. To data, monitoring data have shown not verifiable evidence of contaminants in the groundwater, and because of uncertainty about inventory, it was unknown whether the contaminants were still in the vadose zone or whether they had already been flushed from the system. There was, however, evidence of surface contamination attributed to animal intrusion in one of the 200-TW-1 OU waste sites. The 216-B-26 Trench was recently characterized to augment existing information and to reduce uncertainties related to geology and contaminant distribution and to support an accelerated cleanup schedule. Data from the 216-B-26 characterization provided significant insight into the spatial distribution of contamination in the vadose zone. Much of the contamination is now known to still be in the vadose zone, thereby posing a possible long-term source for groundwater contamination. Owing to the potential risk, remediation is being accelerated at the BC cribs and trenches area and the associated BC controlled area. Developing an effective remediation plan and evaluating remedial options require detailed analysis of fate and transport for this site. Such an analysis must rely on numerical modeling.

Historically, liquid-waste disposals to the ground at the U.S. Department of Energy's (DOE's) Hanford Site have relied on models to predict the fate and transport of chemicals discharged in the liquid effluents. Early models used for discharge calculations were relatively simple and based on the concept of specific retention (Haney and Honsted, 1958). It was typically assumed that the waste discharges would move readily into the vadose zone (i.e., zone between the land surface and the groundwater table) and be retained by the sediments. It was also assumed that the recharge was negligible under the hot, dry conditions typical of Hanford. While it was recognized that lateral spreading of contaminants could take place, it was typically ignored in the calculations of specific retention (Haney and Honsted, 1958). Observations of subsurface contaminant distributions show significant discrepancies from predictions from simple models.

Recent groundwater-monitoring data suggest that contaminants associated with liquid discharges and tank leaks are in the groundwater beneath some waste sites at Hanford (Hartman et al. 2004). Yet, at other sites that received similar volumes of effluent discharges of similar chemical composition and exposed to identical meteorological conditions (e.g. rainfall and snowmelt), contaminants are in the vadose zone, high above the water table. A striking example is the difference between the SX tank farm and the BC cribs and trenches area. Tank SX-115 is reported to have leaked approximately $1.90 \cdot 10^6$ L (50,000 gal) of

reduction-oxidation (REDOX) high-level liquid waste in 1965 (Hartman et al. 2004). Although the exact source is unknown, $^{99}$Tc at concentrations over 75,000 pCi $L^{-1}$ were recently reported for a monitoring well near SX-115 (Hartman et al. 2004). In contrast, some $3.686 \cdot 10^6$ L ($9.737 \times 10^6$ gal) of supernatant fluid containing 128 Ci of $^{99}$Tc were discharged to seven trenches over a period of about 1.5 years in the BC cribs and trenches area, yet there is no evidence of groundwater contamination from the cribs or trenches. The current distribution of $^{99}$Tc in the vadose zone beneath 216-B-26 is therefore not easy to explain using current conceptual models. Recent sampling at the 216-B-26 Trench shows a zone of $^{99}$Tc contamination between 18 and 53 m. The peak soil concentration is exceeds 100 pCi/g while the pore water concentration is approximately $1.4 \cdot 10^6$ pCi/L, both at a depth of about 30 m.

Existing conceptual models typically ignore small-scale stratigraphy and treat the porous media as homogenous and isotropic. Simulations with these models suggest that migration of waste from specific retention trenches was typically rapid and vertical with mobile contaminants reaching the unconfined aquifer within weeks of discharge. Current hypotheses for the discrepancy between model predictions and field observations include overestimation of scavenged waste discharges to the trenches and/or extensive lateral spreading of the contaminant plume in the near surface. Confirmation of either hypothesis is essential to developing a remediation strategy for the site. For the BC Trench site, such confirmation may possible with a detailed analysis of the features, processes, and events at the 216-B-26 Trench.

## 1.1 Purpose and Scope

Accelerated remediation of the BC Cribs and Trenches Feasibility Study (FS) may be viewed as occurring in three phases: the development of alternatives, the screening of the alternatives, and the detailed analysis of alternatives. The scope of this study is to identify source-control alternatives that provide an appropriate range of remedial options and sufficient information to support the comparison of alternatives against one another. Owing to site-specific conditions (depth of contaminants, spatial extent of contamination), the range of options may be somewhat limited. Waste was disposed in large volumes, and radioisotopes were co-disposed with metals as well as inorganic and organic contaminants. Because of the extent of the waste site and the heterogeneity of the plume, treatment alternatives may be impractical. Under such circumstances, the U.S. Environmental Protection Agency (EPA) generally considers containment to be the appropriate response action, or the "presumptive remedy," for the source areas. Thus, the analysis will focus on one or more alternatives that involve containment of the waste with little or no treatment. The goal is to identify containment alternatives with the capability to protect human health and the environment by preventing potential exposure and/or reducing the mobility of contaminants.

Remedial alternatives are typically developed concurrently with the remedial investigation (RI) site characterization; thus, the results of one can be expected to influence the other in a feedback mechanism. Site-characterization data collected during the remedial investigation are typically used in the development of alternatives and to screen technologies, whereas the range of alternatives developed guides subsequent site characterization and/or treatability studies. Thus, alternatives that are developed and screened at this stage may very well be used to guide further characterization.

In the following sections, we develop containment alternatives for remedial actions and evaluate these alternatives against a no-action alternative to allow elimination of those that would be unable to meet

preliminary remediation goals. Evaluation of the alternatives requires a good understanding of the active fate-and-transport mechanisms to support development of the most appropriate conceptual model. The retention of large concentrations of $^{99}Tc$ high above the water table is indicative of strong stratigraphic controls on the downward migration. With an accurate conceptual model, it will should be possible to identify the volumes or areas of soil to which general response actions may have to be applied. The alternatives resulting from this study will provide decision-makers with an appropriate range of options and sufficient information to adequately compare alternatives against one another and against a no-action alternative, taking into account the requirements for adequate protection. The site conceptual model on which the evaluation of alternatives is based is described below. This conceptual model was coupled with a numerical model to evaluate the actual and potential magnitude of leachate releases from the vadose zone; and the potential for future horizontal and vertical migration of these contaminants.

# 2.0 Site Conceptual Model

The conceptual model describes the important features, events, and processes controlling fluid flow and contaminant transport at the waste site of interest. Development of the conceptual model is perhaps the most critical step in modeling contaminant fate and transport. The model is dynamic, becoming more refined as more information about the specific site becomes available. The model that is ultimately selected and the assumptions on which it is based can have serious implications for risk assessment. The problem of interest here is the fate and transport behavior of contaminants of concern, primarily $^{99}$Tc, in the vadose zone at the BC cribs and trenches, with special interest in the 216-B-26 trench. Because the conceptual model is dynamic, an important part of the modeling process is to use field data to calibrate and independently test the predictive capabilities of the model. Kincaid et al. (1998) provides a comprehensive compilation of the 1) features (the structure and transport properties of the various pathways), 2) events (e.g., recharge, source releases), and 3) processes (the fate-and-transport processes/mechanisms, including driving forces) considered relevant to contaminant flow and transport within the vadose zone beneath the Hanford Site. In the following sections, we summarize the features, events, and processes relevant to the BC Trench site and present the steps for quantifying their impacts using the Subsurface Transport Over Multiple Phases (STOMP) simulator.

## 2.1 Site Features

Site features include the surface and subsurface physical structure, e.g., hydrostratigraphy, hydraulic, geochemical, and biochemical properties, of the vadose zone that may impact contaminant migration. Field and laboratory measurements on undisturbed and repacked samples show the hydraulic and geochemical properties of Hanford sediments to be highly variable in space, even within apparently homogeneous hydrostratigraphic units.

The scale of resolution of geologic data used to define the nature and extent of various hydrogeologic units beneath most of Hanford's waste sites is based on borehole samples, many of which were generally taken at intervals of about 5 ft vertically and 10s to 100s of feet horizontally (Figure 2.1). Thus, the fine-grained units, many of which are ≤0.15 m thick, are often not identified. There are very few sites that have been subjected to any type of analyses to quantitatively describe the internal structure and heterogeneities in outcrop and core samples. Thus, in many cases, there is a lack of site-specific data to support the development of detailed three-dimensional (3-D) geologic models for a given waste site. In the sections below, we describe the approach used to gain an understanding of the nature of heterogeneity at the 216-B-26 Trench.

### 2.1.1 Hydrostratigraphy

The BC cribs and trenches are located in the 200 East Area of Hanford's central plateau. The geology and hydrology of the 200 Area have been extensively studied because they contain major sources of groundwater contamination (Hartman et al. 2004). The vadose zone beneath the 200 East Area can be subdivided into five principal hydrostratigraphic units, including three Hanford-formation units and two units belonging to the Ringold Formation (Connelly et al. 1992). The Hanford formation units include 1) the upper-gravel-dominated Hanford formation, 2) the sand-dominated Hanford formation, and 3) the lower-gravel-dominated Hanford formation. Over most of the 200 East Area, the Hanford sand facies lay between the upper and lower sequence of the Hanford gravel facies (Connelly et al. 1992).

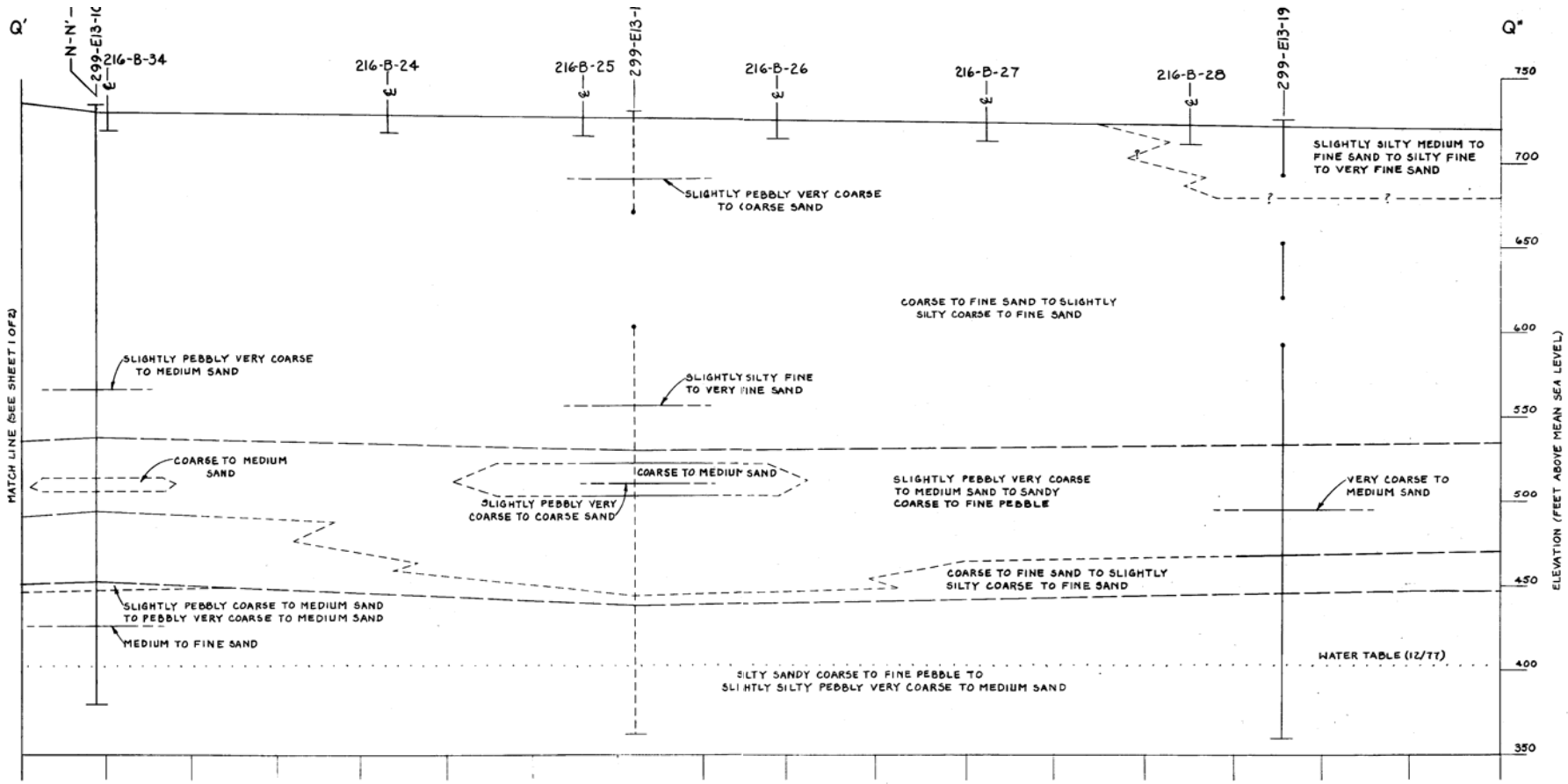


**Figure 2.1. North-South Profile for Cross-Section Dissecting Trenches 216-B-34 Through 216-B-28**

Based on data from borehole samples, the upper and lower gravel sequences appear to have similar physical and chemical properties. The Ringold Formation in the 200 East Area is, for the most part, eroded away in the northern half of 200 East Area. Here, the Hanford formation lies directly on top of basalt bedrock. The water table lies within the Ringold Formation just south of 200 East Area. Because the physical and chemical characteristics of the Ringold Unit A and Ringold Unit E gravels are similar, and because only a small portion of the vadose zone lies within the Ringold Unit A gravel, these units are often combined into a single hydrostratigraphic unit, namely the Ringold gravel unit. In recent years, as the water table has declined in elevation, the basalt bedrock has become unsaturated beneath the northeastern portion of 200 East Area. Other features include clastic dikes which have been observed in the Hanford formation beneath 200 East Area. The vertically oriented clay skins within clastic dikes have been hypothesized to act locally to mitigate lateral flow in adjacent fine-textured strata. Structures that mitigate lateral flow could lead to ponding of the water and the eventual breakthrough to underlying strata.

One of assumptions most frequently made in modeling the infiltration and the redistribution of water into soils and sediments at Hanford is that the porous medium is homogenous and isotropic. Such an assumption is unlikely to be borne out in nature. Soil and rock formation starts with the deposition of sediments and is followed by compaction and alteration processes that can cause drastic changes in morphology of the formation. Such formations show a distinct microscale structure characterized by the presence of multiple sedimentary layers. At the macroscopic scale, the primary manifestation of the microstructure is a complex layered system characterized by anisotropy in mechanical, electrical, and hydraulic properties. Given that many of the samples on which the subsurface hydrostratigraphy is based were taken from vertical sampling depths of 5 ft and horizontal distances on the order of 10s to 100s of feet horizontally, many of the small-scale features controlling transport were typically indiscernible. The method of drilling and sampling also meant that the internal structure of these sedimentary units was difficult to preserve. Thus, it is impossible to rely solely on sparsely sampled grain-size data to accurately describe the subsurface heterogeneity. Consequently, there is a lack of site-specific data on which detailed 3-D hydrostratigraphic models can be developed. Increased knowledge of the internal structure and heterogeneities of many of these units have come from extrapolation of high-resolution geophysical logs and outcrops at representative sites (Figure 2.2).

The Ringold Formation and the Hanford formation typically contain relatively thin fine-textured lenses that can result in lateral spreading of moisture and can slow down the vertical movement of contaminants within the vadose zone. This phenomenon is caused by the Richards' effect in which fine over coarse sediment sequences form capillary breaks that typically limit the downward migration of water and contaminants while enhancing lateral flow under certain conditions. Lateral flow generally occurs until the soil-water potential is sufficient to overcome the entry pressure of the coarse underlying layers, or some other vertical path of lower resistance is found. Fine-textured lenses typically have low vertical permeabilities and relatively high horizontal permeabilities. Paleosols and other fine-grained facies appear to be fairly continuous over ranges of about 100 m and have been found to promote lateral spreading of crib effluent on a similar scale. Low vertical permeability layers, where they exist, often occur as single, relatively thick (meters or more) and continuous layers within the Ringold Formation. Low-permeability layers within the Hanford formation occur more frequently, but are relatively thin (0.5 m or less) and laterally discontinuous with frequent pinch outs (Figure 2.2). Thus, neglecting small-scale textural changes could lead to an underestimation of the extent of lateral spreading, which could lead to erroneous predictions of penetration depth and rate of transport.

**Figure 2.2. Exposed Trench Face Showing Layered Heterogeneity in Hanford's 200 East Area. This trench was located near the south boundary of the ILAW Site.**

At wastes sites characterized by the types of layered heterogeneity shown above, the geometry and configuration of sedimentary, hydrologic, and geochemical facies are difficult to define without extensive excavation and sampling. The structure of these features, however, can be captured by coupling high-resolution geophysical borehole logs with less-frequent grain-size distributions through pedotransfer functions. Figure 2.3 shows the summary geologist's descriptions and geophysical logs for the C4191 borehole at the 216-B-26 Trench. Although Figure 2.1 suggests relatively homogeneous layers that could be easily represented, perhaps by a perfectly stratified model, geophysical logs show a much more heterogeneous profile with a near-surface distribution consistent with Figure 2.2.

Neutron moisture logs have been shown to be useful stratigraphic indicators (Kramer et al. 1995). Theory predicts that coarse-textured soils generate relatively low neutron counts while fine-textured silt and clay layers generate much higher counts. Figure 2.3 shows a small offset between the geologist's descriptive log, the low-frequency laboratory measurements of moisture, and the high-resolution neutron log. High neutron counts and moisture do not always correlate with fine-textured silt lenses in the geologist's log. We believe that the spatial differences between the lab-measured moisture and the neutron logs are caused by the smoothing effect of using grab samples for the measurements in the case of the 216-B-26 trench. There is also a difference between the absolute moisture contents derived from the laboratory measurements and the neutron logs, which may be due to probe calibration errors. Nevertheless, the neutron measurements, which were made in the undisturbed medium at a resolution of about 3 inches, clearly show the effects of small-scale stratigraphy. Thus, neutron logging can be a cost-effective

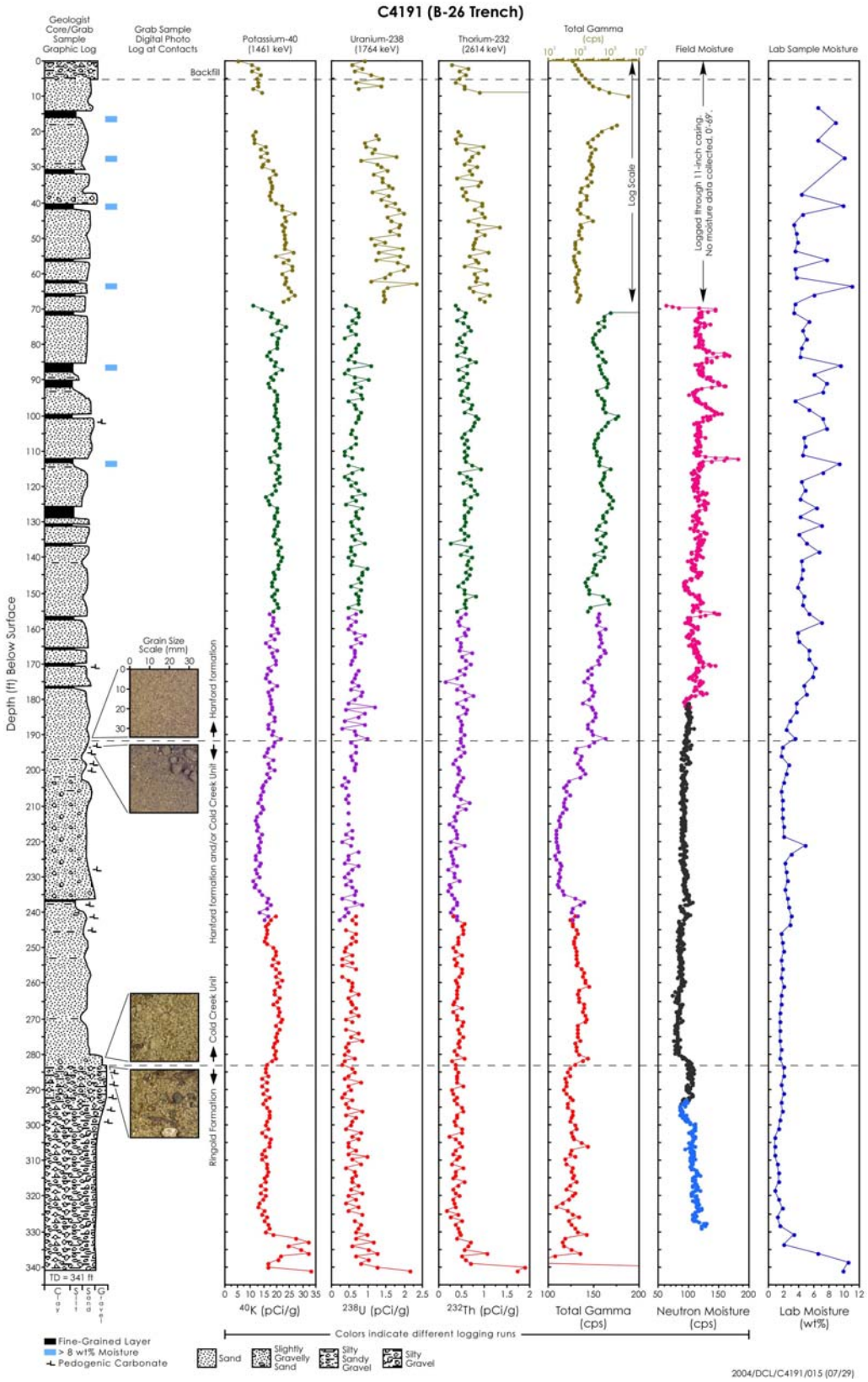


**Figure 2.3. Summary Geologic Log for Borehole C4191 at the 216-B-26 Trench**

reconnaissance tool to locate specific, potential, or suspected flow paths in existing wells or borings that are not continuously cored or sampled (Kramer et al. 1995).

When the $^{99}$Tc data and the neutron moisture logs are reviewed simultaneously, the effect of the subsurface features on flow and transport become more apparent. Naturally occurring fine-textured lenses are abundant in this area (Figure 2.2 and Figure 2.3), and much of the contamination in borehole C4191 found between two fine-textured layers occurs between 18 and 53 m below the surface. The bimodal nature of the mobile contaminant plume reflects the combined effect of textural contrasts and lateral migration. We hypothesize a two-stage transport process. In the first stage, the small-scale stratigraphy led to significant lateral movement in the layers immediately beneath the trench. Such stratigraphic effects on flow are not unprecedented in the Hanford vadose zone. Data from the 216-U-cribs suggest that perched water beneath a the 216-U-16 crib was diverted hundreds of meters horizontally by a caliche layer before contacting uranium-contaminated soils beneath the U-1 and U-2 Crib and migrating down the unsealed annulus of a borehole (DOE-RL (1998). Vadose zone transport field studies conducted under the Remediation and Closure Science project also show similar behavior.

In FY 2000 and 2001, a series of field experiments designed to simulate a subsurface leak were conducted at the Sisson and Lu Site in the 200 East Area. Three-dimensional distributions of water content measured during the experiments show a continuous layer of higher values, indicative of a fine-textured layer, between 5.5 and 7.0 m and sloping upwards in an easterly direction. A similar layer is also observed between 10.5 and 11.5 m. The layer sequence of fine-over coarse layers produces natural capillary breaks resulting in preferential lateral flow within the fine-textured layer until the water-entry pressure of the coarser soil is exceeded. The net effect is an asymmetric wetting front (Figure 2.4).

Figure 2.5 compares the time dependence of the zeroth moment, $M_0$, which is essentially the recovered mass of water derived from neutron logs, with the injected mass of water in kilograms in the FY 2000 test. Until the third injection, the relationship between the injected mass and the recovered mass showed very good agreement. The pump rate during the test was kept relatively constant, and the cumulative injected mass approximates a straight line with some 11,983.37 kg of water injected by the end of the third injection on June 15, 2000, and a total of 19,972.29 kg injected by June 28, 2000. Boreholes were typically logged within 24 hours of each injection. Mass recovery from the June 16, 2000, logging accounted for 11,404 kg or 95.2 percent of the injected mass. Given the 24-hour delay in measurement and the error in the neutron probe resulting from the use of a single calibration curve for a layered system, the mass recovery is quite remarkable. By the fourth injection, 15,977.8 kg of water had been injected, but the recovered mass was only 13,803 kg or 86.4 percent. From this point on, the divergence between the injected and recovered mass continued to increase. By the end of the monitoring period on June 31, 2000, mass recovery was only 10,262 kg, or 51.4 percent of the injected amount.

The only possible explanation for the divergence between the injected and recovered mass of water is in water leaving the monitoring domain. While the boreholes used for monitoring extend to a maximum of 8 m from the injection point, there was no physical subsurface boundary to retain water in the domain, so the water was free to redistribute in 3-D space in response to the potential gradients. Analysis of the first moments, $M_1$, for the lateral and transverse direction at the longitudinal center of mass show that the wetting front moved preferentially in a south-easterly direction in both tests. A more notable observation,

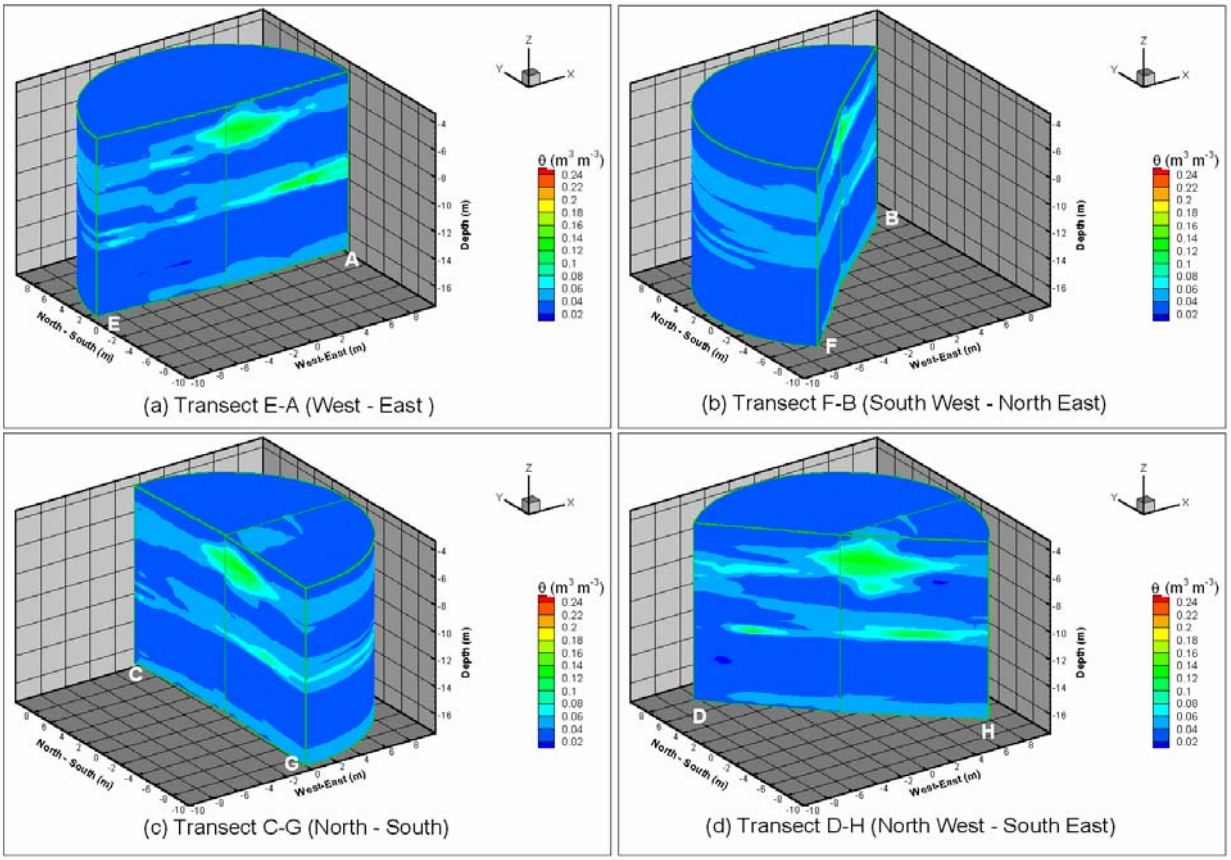


**Figure 2.4. Spatial Distribution of Soil-Water Content, θ, Interpolated from Neutron Probe Measurements in the 32 Wells at the Vadose-Zone Test Site on June 02, 2000, After an Injection of 4000 L (1057 gal) of Salt-Free Water (a) Transect E-A, (b) Transect F-B, (c) Transect C-G, and (d) Transect B-F**

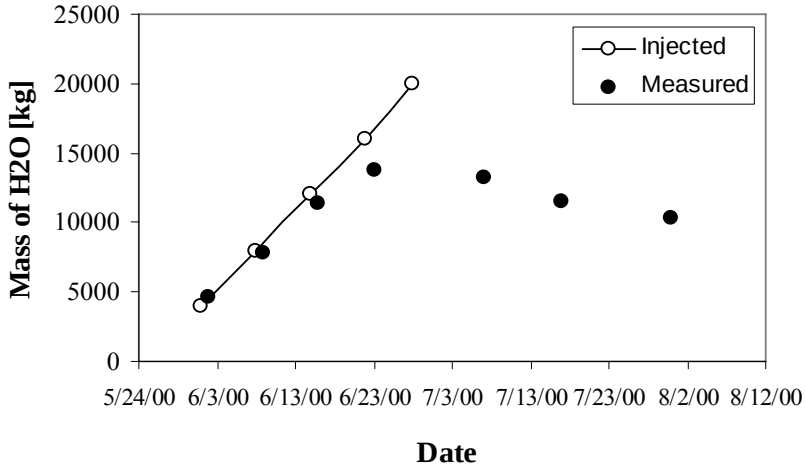


**Figure 2.5. A Comparison of Injected and Recovered Mass of Water from the Monitored Domain of the Field Test Site During the FY 2000 Simulated Tank-Leak Test. The divergence of injected from recovered mass is attributed to water leaving the domain because of lateral flow.**

based on stable isotope analysis, was that none of the injected water ever penetrated the lower fine-textured layers.

It is therefore quite likely that in highly heterogeneous sediments, such as those at the BC trench site, injected water could have redistributed in the shallow subsurface, thereby minimizing the downward migration of the contaminants and keeping them high above the water table. However, a large volume of water could have overcome the multiple capillary breaks and the main one at 34 m. The leading and trailing edges of the plume resulted from the same liquid release event and likely showed similar peak concentrations. After the leading edge crossed the capillary break formed by the fine over-coarse sequence at 34.21 m, the soil water suction likely decreased to a point where further downward migration of the trailing section was curtailed. This would have resulted in a relatively low concentration zone between the 34-m and 36.6-m depths. In the second stage, following the dissipation of the effects of the fluid discharges, the driving force was due mostly to natural recharge and this resulted in a slow downward migration of the mobile contaminants. The leading edge continued its downward movement but was finally stopped by another capillary break formed by the fine over-coarse sequence at 47 m. The lower peak concentration in the leading edge is caused by a combination of lateral spreading above the lower capillary break and the accumulation of contaminants above the 33.5-m depth. The low concentrations of mobile species between the trench bottoms and the 18-m depth suggest that the upper vadose zone may have leached by natural recharge following trench closure. The lack of recharge events or additional liquid discharges that could overcome the natural capillary break at 33.5 m may have led to an accumulation of contaminants and higher concentrations in the trailing edge of the plume. Equalization of the concentrations in the two sections would require a significant increase in water suction to overcome the water-entry pressure of the separating coarse-textured layer.

The neutron moisture logs from C4191 and surrounding boreholes are therefore central to developing the conceptual model of flow and transport at 216-B-26. Accurate simulation of flow and transport must therefore account for the small-scale lithostratigraphy with adequate description of the local-scale hydraulic properties and saturation-dependent anisotropy mechanisms. Failure to account for these heterogeneities, which manifest as thin layers, would likely result in an underestimation of lateral spreading and an overprediction of the penetration depth.

### 2.1.2 Hydraulic Properties

Accurate predictions of flow and transport in the vadose zone require a characterization of the hydrologic properties. In heterogeneous sediments, such as those shown above, detailed characterization of the hydraulic properties and their variability are the minimum requirements for predicting field-scale flow (Ward et al. 2002). Required properties for variably saturated flow include the soil moisture characteristic, i.e., the water content-capillary pressure relationship, $\theta(\psi)$; and the unsaturated hydraulic conductivity versus capillary pressure relationships, $K(\psi)$, including parameters for describing saturation-dependent anisotropy. No hydraulic properties were measured on the samples from the C4191 borehole and no undisturbed samples were available for characterization. Sampling was limited to grab samples, which had undergone considerable mixing, thereby making the interpretation of laboratory measurements a difficult task. Nevertheless, a number of representative samples were selected for grain-size analysis based on observed contrasts in water content. With no site-specific hydraulic properties, the grain-size statistics obtained from the analysis of selected grab samples were used to estimate properties using pedotransfer functions. The pedotransfer functions assume that the relationships between moisture

content, pressure head, and unsaturated hydraulic conductivity are nonhysteretic and can be represented by the Brooks-Corey (Brooks and Corey 1964) water-retention and relative-conductivity model. The pedotransfer functions were used to estimate the saturated hydraulic conductivity, $K_s$; saturated water content, $\theta_s$; the Brooks-Corey pore size distribution index, $\lambda$,; and the Brooks-Corey bubbling pressure, $\psi_b$. Calculated parameters are summarized in Section 3.4.

### 2.1.3 Transport Properties

Accurate predictions of flow and transport also require detailed characterization of the transport parameters, particularly dispersivity, $\alpha$. Dispersivity is well known to be scale-dependent, but there are few data for Hanford sediments, especially at scales relevant to the current problem. Recent field experiments resulted in the estimation of longitudinal and transverse dispersivities at the Army Loop Road site, but transport distances were limited to a maximum of 1 m (Ward and Gee 2003). It is also known that dispersivity is a function of texture. Studies conducted in the 1960s and 1970s showed the dispersivity to vary with mean grain diameter, $d_{50}$ (Harlem and Rumer 1963; Bruch 1970). More recently, Perfect et al. (2002) reported a pedotransfer function approach for predicting longitudinal dispersivity, $\alpha_L$, from existing databases of soil hydraulic properties. They found that $\alpha_L$ increased as the Brooks-Corey bubbling pressure, $\psi_b$, and the Campbell exponent (Campbell 1974), $b$, increased. Thus, $\alpha_L$ tended to increase as soil texture became finer and with increasing clay content or as the Brooks-Corey pore-size distribution index, $\lambda$, decreased.

These values, however, are local-scale values and are expected to be smaller than the values needed to predict field-scale behavior. Effective longitudinal and transverse field-scale dispersivitiy, applicable to both $^{99}$Tc and $NO_3$, were estimated by fitting the observed $^{99}$Tc concentration profile obtained from the C4191 borehole to an analytical solution of the convective dispersive equation (CDE), assuming 1-D advection and 2-D dispersion (Leij et al. 1991). The resulting values represent effective values that reflect the total contribution of the various layers. However, local-scale estimates of $\alpha_L$ can be obtained for individual layers from their $\lambda$ values using the method proposed by Perfect at al. (2002). The transverse dispersivity was assumed to be 0.1 of the longitudinal dispersivity.

### 2.1.4 Geochemical Properties

Detailed characterization of the geochemical parameters used to describe sorption is also needed for predicting the transport of contaminants in heterogeneous sediments. The choice of parameters depends on the nature of the model as some transport models use a distribution coefficient, $K_d$, approach to sorption while other such as the multi-component exchange models require information on cation exchange capacity (CEC) and selectivity coefficients for the contaminant of interest. In general, the finer-grain sediments tend to have a greater tendency to adsorb reactive contaminants. Adsorption is assumed to be the controlling geochemical process in this case and transport model used for the sorption of cations in this study is based on the $K_d$ approach.

The adsorption of Tc(VII) is low under nearly all conditions relevant to the Hanford vadose zone and upper unconfined aquifer, and $K_d$ values range from zero to a high of approximately 1 mL/g (Cantrell et al. 2003). However, the high values also have high standard deviations and the 1 mL/g has not been substantiated by any other studies. Under normal Hanford conditions, zero appears to be the most appropriate value, with a best estimate for the range as 0.0 to 0.1 mL/g (Cantrell et al. 2003). Under

natural Hanford groundwater conditions, U(VI) adsorption is moderate with $K_d$ values ranging from approximately 0.2 to 4 (Cantrell et al. 2003). Thus, uranium migration under natural Hanford conditions is high to moderate with greater migration occurring at high and low pH values. The recommended range suggested in the Immobilized Low-Activity Waste Performance Assessment Far Field for $^{234/235/238}U$ is 0.1 to 8.0 (Cantrell et al. 2003). Based on this analysis, a range of 0.2 to 4 is more likely to be appropriate. For this conceptual model, a linear sorption isotherm model is assumed. Although the ionic strength of the discharged waste can play a role in sorption processes, it is not considered in this study.

## 2.2 Site Events

Site-specific events are also included in developing the conceptual model because these events affect the choice of initial and boundary conditions as well as the spatial extent of the computational domain. Events that are typically included are the natural (e.g., meteoric recharge) and man-made (e.g., accidental and intentional) fluid and contaminant releases. Liquid discharges were of two types, 1) unrestricted, which went to cribs, and 2) restricted, which went to specific retention trenches. The restricted discharges were intended to limit the total volume discharged such that the discharged fluid was retained in the vadose zone based on the concept of specific retention (Haney and Honstead, 1958). In contrast, unrestricted discharges to cribs were assumed to release some of the contaminants to the groundwater. Discharges to most cribs and trenches were completed over relatively short times, ranging from a month to a year. These discharges therefore created a strong driving force for vertical transport through the vadose zone. There are several discharge events that could have impacted the distribution of contaminants beneath the 216-B-26 Trench. These events are summarized in the following sections.

### 2.2.1 Release Events

Release events represent the source terms in the conceptual and numerical models. These events include both intentional and recorded accidental discharges of fluids and contaminants to the vadose zone. These events must be characterized for quantity and duration of the releases. Given the potential for lateral migration of contaminants in these sediments, it is necessary to consider the trenches adjacent to the 216-B-26 trench. Numerous cribs and trenches in the 200-TW-1 OU waste sites received large quantities of wastewater containing significant quantities of mobile radionuclides (e.g., $^{99}Tc$) and chemicals (e.g., $NO_3^-$).

Six trenches in the immediate vicinity of the 216-B-26 Trench were operational during the same time frame as 216-B-26. These include 216-B28 and 216-B-27 to the south and 216-B-25 through 216-B-23 and 216-B-52 to the north. For the most part, the liquid volumes, waste-stream types, and chronology are reasonably well known. Median fluid discharge volumes and contaminant inventories, derived from the SIMS model of Simpson et al. (2001), are summarized in Table 2.1 through Table 2.4. Discharges were generally short, lasting from 30 days to 90 days. The mean volume was just over 4000 $m^3$, except for the much larger 216-B-52 Trench, which received over 8500 $m^3$ of fluid. Trenches 216-B-23 through 216-B-28 received median values of $^{99}Tc$ ranging from 16 to 18 Ci while 216-B-52 received over 25 Ci.

**Table 2.1. 2004 Composite Analysis 10,000-year (Median Inputs)**
**Assessment of Fluid Discharge Volumes**

| Trench | Length (m) | Start Date | End Date | Duration (day) | Vol ($m^3$) |
|---|---|---|---|---|---|
| 216-B-52 | 176.78 | 12/01/57 | 01/01/58 | 31 | 8529.52 |
| 216-B-23 | 152.40 | 10/01/56 | 10/31/56 | 30 | 4519.90 |
| 216-B-24 | 152.40 | 10/01/56 | 11/01/56 | 31 | 4869.87 |
| 216-B-25 | 152.40 | 11/01/56 | 12/01/56 | 30 | 4909.90 |
| 216-B-26 | 152.40 | 12/01/56 | 02/01/57 | 62 | 4745.64 |
| 216-B-27 | 152.40 | 02/01/57 | 04/01/57 | 59 | 4419.88 |
| 216-B-28 | 152.40 | 04/01/57 | 06/30/57 | 90 | 5049.79 |

**Table 2.2. 2004 Composite Analysis 10,000-year (Median Inputs) Assessment for $^{99}Tc$ (Ci)**

| Year | COC | Analyte Influx by Trench | | | | | | |
|---|---|---|---|---|---|---|---|---|
| | | B-52 | B-23 | B-24 | B-25 | B-26 | B-27 | B-28 |
| 1955 | $^{99}Tc$ | 0.0000 | 0.0000 | 0.0000 | 0.0000 | 0.0000 | 0.0000 | 0.0000 |
| 1956 | $^{99}Tc$ | 0.0167 | 0.0000 | 0.0476 | 0.0000 | 14.2491 | 0.0452 | 0.0476 |
| 1957 | $^{99}Tc$ | 6.1197 | 15.3636 | 18.1086 | 18.0399 | 3.3504 | 16.4384 | 17.3002 |
| 1958 | $^{99}Tc$ | 19.3691 | 0.0000 | 0.0000 | 0.0000 | 0.0000 | 0.0000 | 0.0000 |
| 1959 | $^{99}Tc$ | 0.0000 | 0.0000 | 0.0000 | 0.0000 | 0.0000 | 0.0000 | 0.0000 |
| | **Total** | 25.5044 | 15.3636 | 18.1086 | 18.3099 | 17.5995 | 16.4836 | 17.3678 |

**Table 2.3. 2004 Composite Analysis 10,000-Year (Median Inputs) Assessment for $NO_3^-$ (kg)**

| Year | COC | Analyte Influx by Trench | | | | | | |
|---|---|---|---|---|---|---|---|---|
| | | B-52 | B-23 | B-24 | B-25 | B-26 | B-27 | B-28 |
| 1955 | $NO_3^-$ | 0.0 | 0.0 | 0.0 | 0.0 | 0.0 | 0.0 | 0.0 |
| 1956 | $NO_3^-$ | 0.0 | 802052.7 | 959358.7 | 966725.6 | 751029.6 | 0.0 | 0.0 |
| 1957 | $NO_3^-$ | 321183.5 | 0.0 | 0.0 | 0.0 | 177256.6 | 871113.6 | 916344.3 |
| 1958 | $NO_3^-$ | 962740.7 | 0.0 | 0.0 | 0.0 | 0.0 | 0.0 | 0.0 |
| 1959 | $NO_3^-$ | 0.0 | 0.0 | 0.0 | 0.0 | 0.0 | 0.0 | 0.0 |
| | **Total** | 1283924.2 | 802052.7 | 959358.7 | 966725.6 | 928286.2 | 871113.6 | 916344.3 |

**Table 2.4. 2004 Composite Analysis 10,000-Year (Median Inputs) Assessment for $^{238}U$ (Ci)**

| Year | COC | Analyte Influx by Trench | | | | | | |
|---|---|---|---|---|---|---|---|---|
| | | B-52 | B-23 | B-24 | B-25 | B-26 | B-27 | B-28 |
| 1955 | $^{238}U$ | 0.0000 | 0.0000 | 0.0000 | 0.0000 | 0.0000 | 0.0000 | 0.0000 |
| 1956 | $^{238}U$ | 0.0000 | 0.0371 | 0.0355 | 0.0359 | 0.0303 | 0.0000 | 0.0000 |
| 1957 | $^{238}U$ | 0.0162 | 0.0000 | 0.0000 | 0.0000 | 0.0072 | 0.0323 | 0.0408 |
| 1958 | $^{238}U$ | 0.0491 | 0.0000 | 0.0000 | 0.0000 | 0.0000 | 0.0000 | 0.0000 |
| 1959 | $^{238}U$ | 0.0000 | 0.0000 | 0.0000 | 0.0000 | 0.0000 | 0.0000 | 0.0000 |
| | **Total** | 0.0654 | 0.0371 | 0.0355 | 0.0359 | 0.0375 | 0.0323 | 0.0408 |

### 2.2.2 Recharge Events

In the past, it was assumed that natural precipitation did not contribute to recharge in arid and semi-arid environments such as Hanford. It is now known that precipitation has the potential to contribute to recharge. The amount of recharge generated by a precipitation event can be quite site-specific.

The rate of recharge at a particular location is influenced by four main factors: topography, climate, soil type, and vegetation. Potential evapotranspiration (PET)[(a)] is a measure of the capability of the atmosphere to remove water from the surface through the processes of evaporation and transpiration assuming an unlimited water supply. At Hanford, the PET typically exceeds precipitation. Actual evapotranspiration or AE is the quantity of water that is removed from a surface due to the processes of evaporation and transpiration. At Hanford, actual evapotranspiration is generally equal to precipitation (Gee et al. 1988). Therefore, most of the water stored in the soil will eventually be evaporated or transpired. High PET and fine-textured soils with a high water holding capacity combine to limit recharge to the groundwater. Recharge is generally small in vegetated shrub-steppe ecosystems, but it can be very important, particularly when the potential for long-term contaminant remobilization is considered. Without adequate storage capacity in the fine soil layer, there may be times when the storage capacity will be exceeded, and groundwater recharge can occur. In extremely wet years, or in the absence of vegetation, significant amounts of water may move out of the root zone, creating the potential for deep drainage and contaminant transport (Gee et al. 1988). Historical aerial photos show that the site was covered predominantly with grasses and sage brush before installing the trenches. The recharge rate would have been in the 0 to 10 mm $yr^{-1}$ range (Figure 2.6). Thus, a recharge rate of 3.5 mm $yr^{-1}$ was selected as the initial recharge rate.

Depending on the surface conditions, recharge can be diffused or focused and the distribution ultimately affects subsurface transport. Both short-term and long-term rates can affect the behavior of contaminants in the subsurface. Rates could also be expected to show some temporal variation. Before installing trenches, recharge rates would have been consistent with those expected for a mature shrub-steppe community. Construction of the trenches would have resulted in the removal of vegetation and an increase in recharge (Figure 2.7). Thus, during operation and before backfilling, the recharge rate would have increased to values consistent with that of a bare surface (50 to 100 mm $yr^{-1}$). Installation of the

(a) Water extracted by the plant's root system is referred to as transpiration and is no longer available for recharge or contaminant transport. The evapotranspiration process is composed of evaporation and transpiration.

trench would have resulted in land clearing. It appears that the trench surfaces were kept relatively free of vegetation because a more recent aerial photograph from 2002 show an essentially bare surface similar to that in Figure 2.7 except that there is now a finer-textured overburden layer.

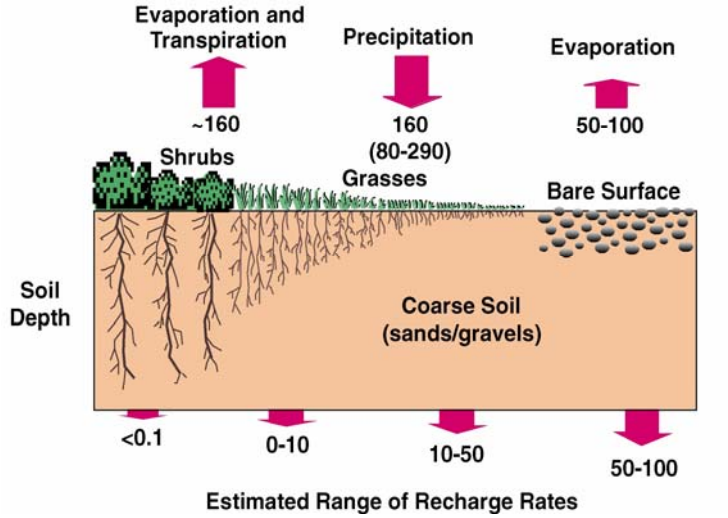


**Figure 2.6. Schematic Representation of Hanford Site Water Balance Showing Variable Recharge Rates**

**Figure 2.7. Aerial Photograph of BC Trenches Shortly After Excavation**

The trenches were backfilled after they were completed, and, over time, vegetation would have invaded the surfaces. Recharge would have decreased to a range consistent with a mixed surface of shrubs and grasses, i.e., between 10 and 50 mm $yr^{-1}$. A meteoric recharge rate of 25 mm $yr^{-1}$ is assumed based on measurements from the Hanford barrier (Ward et al, 2005). These data show an average recharge rate of 18 percent of precipitation on a sparsely-vegetated gravel cover. Backfilling and stabilization would have resulted in a moderate reduction while remediation and closure would bring about a significant reduction,

depending on the chosen remedy. In this study, long-term recharge estimates from natural precipitation (3.5 mm/yr) are based on data reported by Fayer and Walters (1995). Recharge rates subsequent to remediation and closure are based on the performance criterion of the prototype Hanford barrier (Ward et al. 1997).

## 2.3 Fate and Transport

An understanding of the fate-and-transport processes acting on the contaminants beneath the BC trench site is a pre-requisite for predicting the partitioning of the contaminants of concern (COCs) between the different components of the environment (i.e., soil, water, and air). For the majority of contaminants, movement through the vadose zone is in the aqueous phase and therefore depends on the contaminants being dissolved in the infiltrating water. Once this water passes the root zone where evaporation and transpiration can affect the quantity available for transport, it can potentially reach the water table. The rate at which the water and associated contaminants move through the vadose zone is controlled by the interaction between the meteorological forcings and the hydraulic, thermal, and vapor gradients that develop in the sediments.

The extent to which these gradients develop is largely controlled by the sediment thermal and hydraulic properties and to a lesser extent by the fluid properties. Transport is also dependent on biogeochemical conditions (pH, Eh). In many respects, the physical and chemical processes prevailing in the vadose zone differ from those that predominate in surface and groundwater (Runnells 1995). These differences are caused mainly by the presence of a gas phase, a typically oxidizing environment, active biological and biochemical processes, and the relatively large specific surface area of unsaturated soils. There are four main processes that are of potential importance in the vadose zone:

- precipitation/dissolution
- volatilization/condensation
- adsorption/desorption
- degradation/transformation.

In the following sections, we provide a general description of the fate-and-transport processes and their possible role and importance to the behavior of the major COCs at the 216-B-26 Trench. These processes are known to affect the form in which a COC may exist, and, along with the dynamics of the environment, the mobility and biogeochemical availability of the contaminant.

### 2.3.1 Precipitation/Dissolution

The chemistry of water infiltrating from snowmelt and rainfall generally evolves to different chemical compositions as the water moves through the vadose zone to the water table. Thus, the final composition of the vadose zone pore water depends on the mineralogy of the soil as well as the texture and permeability that control the contact time through their effect on permeability (Sparks 1989). This is important for the remobilization of existing plumes as there is net dissolution if the vadose zone water is under-saturated with respect to the mineral or chemical species. There is much experimental evidence to show that precipitation reactions control the aqueous concentration of many contaminants (Runnells 1995). Calcium is known to be controlled by equilibrium with calcite or by ion-exchange on clays. Recent experiments on the migration of strontium conducted under the Vadose Zone Transport Field show that sorption of strontium in Hanford sediments is also strongly influenced by equilibrium

with calcite (Ward et al. 2003). Concentrations of Fe and Mn are commonly controlled by oxyhydroxides in the oxygenated vadose zone. Results of the analysis of samples from the C4191 borehole suggest that precipitation could have been an important fate-and-transport mechanism, particularly for $^{238}U$ (Serne and Mann, 2004).

### 2.3.2 Volatilization

At the BC cribs and trenches, the list of COCs shows several species for which volatilization could be important. These include mercury, sulfate, nitrate, nitrite, and a range of SVOCs. Volatilization is the process by which a contaminant is transferred from soil or water into the atmosphere in the gas phase. Some inorganic species can be transformed into volatile components and move through the vadose zone. A well known example is the bacterial reduction of dissolved $SO_4$ to $H_2S$ gas with the loss of $H_2S$ to the atmosphere (Kellogg et al. 1972). Mercury in solution can also be volatilized in anaerobic environments and by reaction with dissolved humic acids. While the microbial reduction of $NO_3$ to $NH_3$ or $N_2$ is well known, this mechanism has not proven significant enough to prevent the wide-spread pollution of groundwater by nitrate. Gaseous transfer is also an important mechanism affecting the fate and transport of volatile and semivolatile contaminants that can occur in response to concentration gradients in the vadose zone. The importance of volatilization as a transport mechanism depends on the depth to the zone of contamination and the wind velocity at the soil-air interface. However, the COCs at 216-B-26 are at low concentrations (below saturation) and are most likely dissolved in the water phase (i.e., no free non-aqueous phase liquids). While it is likely that volatilization may have been important for the some of the inorganics and the semi volatile organic compounds (SVOCs) during operation of the trench, backfilling of the trench and an increase in near-surface moisture content after operations ceased would have reduced the importance of this mechanism. Volatilization is therefore ignored in this analysis.

### 2.3.3 Sorption/Desorption

Sorption/desorption reactions are based on the principle of attraction between aqueous species and the reactive surfaces of the solid phase of soils and sediments. One of the most common sorption reactions in soils is ion exchange. In its most general meaning, an ion-exchange reaction involves the replacement of one ionic species on a solid phase by another ionic species taken from an aqueous solution in contact with the solid. The sorption of most aqueous-phase inorganic and radionuclides is controlled by ion exchange and surface complexation and therefore depends on the available reactive surface area. Reactive contaminants adsorb to mineral surfaces and the surfaces of chemical precipitates in the soil. Sorption is controlled by a large number of variables, including the pH of the infiltrating water, ionic strength (salinity) of the water, soil particle size distribution, concentrations of the competing ions, mineralogy, and organic carbon content. Aqueous pH affects both the speciation of the metals and the surface charge of the sorbing media. At low pH values, the surfaces of most of the important soil minerals are positively charged and will therefore repel positively charged ions, such as metals, and attract negatively charged ions, such as pertechnetate, $TCO_4^-$. At high pH, the surfaces have a net negative charge and therefore attract the positively charged species and repel the negatively charged species. The speciation of the ions can work against this trend by changing the charge on the ion itself. For instance, at high pH, metals can combine with hydroxide ions in solution, forming an aqueous complex with a neutral or negative charge. Because sorption is a surface phenomenon, the smaller the sediment particle size, the greater the surface area per unit mass of media (specific surface area) and the greater the adsorption. Hanford sediments show a very strong positive correlation between specific surface area and cation exchange capacity and a negative correlation between cation exchange capacity and geometric mean grain diameter (Ward et al.

2005). Sorbed ions can also be desorbed from the surfaces of soils and sediments when introduced to a solution of different chemistry, especially when the salinity is high. A good example, relevant to Hanford in general, and 216-B-26 in particular, where wastes high in sodium were discharged to a system in equilibrium with calcium would be the exchange between $Ca^{++}$ and $Na^{+}$. The ionic strength of the water can decrease the concentration of ions actually seen by the surfaces of the sorbing media, which has the effect of decreasing the $K_d$. This process has been shown to be important in the sorption of $^{137}Cs$ where high $Na^{+}$ reduces the normally high $K_d$ of $^{137}Cs$ (Saiers and Hornberger 1996). In this analysis, sorption is considered only for $^{238}U$ and it is assumed to be described by a linear isotherm.

### 2.3.4 Degradation/Transformation

In addition to the processes described above, contaminants in the vadose zone can also undergo degradation and transformation over time as a result of chemical (abiotic) and microbiological (biotic) reactions. Degradation and transformation may result in compounds that are less toxic, compounds that are more strongly adsorbed and therefore move more slowly through the soil profile, or compounds that are less soluble. In some cases, gaseous products are formed that can be lost to the atmosphere from shallow depths. The degradation and transformation of chemicals from one compound to another can be important in controlling the quantity of a contaminant reaching the groundwater.

Changes in conditions in the subsurface environment can lead to changes in the form and distribution of the contaminant, and this could be of importance to $^{99}Tc$ and $^{238}U$. For example, under oxidizing conditions, $^{99}Tc$ exists as the soluble heptavalent pertechnetate ion, $TcO_4^-$, which, owing to its negative charge, is highly mobile in soils and groundwater (Lieser and Bauscher 1987). However, under reducing conditions, and in the absence of complexing agents, the tetravalent Tc(IV) ion dominates (Francis et al. 2002). In this oxidation state, $^{99}Tc$ is relatively immobile and can form highly insoluble minerals like $TcO_2$ and strong complexes on Al, Fe, and Sb oxides as well as on clays (Lieser and Bauscher 1987; Meyer et al. 1991; Haines et al. 1987; Zhaung et al. 1995). Such changes can be mediated by abiotic and/or biotic processes. For radioactive species, radiolytic decay can result in a reduction in concentration of the contaminant and the production of daughter products. Owing to the long half-lives of the two species of interest, $^{238}U$ and $^{99}Tc$, radiolytic decay and the formation of daughter products are ignored. Biochemical transformations of $NO_3^-$ are also ignored.

### 2.3.5 Evaporation/Transpiration

Water can be removed from the vadose zone via losses to the atmosphere. These losses consist of evaporation from wet soil and plant surfaces as well as from plants through transpiration. Transpiration is the water lost to the atmosphere from small openings on the leaf surfaces and is part of the normal process required for growth and cooling. Significant evaporation from the soil can take place only when the soil's top layer (1 to 2 inches) or plant canopy is wet. Once the soil surface is dry, evaporation decreases sharply. However, deep-rooted plant species can remove water from significant depths in the soil in response to transpiration, making plant water uptake a potentially important fate-and-transport mechanism.

Water loss by evapotranspiration reduces the amount of water available for recharge and the transport of contaminants to the groundwater. Plant uptake is another means by which chemicals in the soil can be removed from the pool available for leaching. Tumble weeds, with roots that can reach down to 20 ft, can take up $^{90}Sr$, break off, and blow off waste sites as reported by Marshall (1987). Transpiration from

shrubs like rabbit brush, sage brush and tumble weed may bring previously distributed dissolved chemicals to the surface through the incorporation into the plant biomass. The importance of plant uptake is dependent on the COC. Nitrates is typically taken up in large quantities and there ample evidence showing the accumulation of radionuclides, including $^{99}Tc$, in plants (Yanagisawa and Muramatsu 1993). Thus, modeling the transport of near-surface contaminants in vegetated waste-management areas should consider the potential uptake of COCs if realistic estimates of quantities migrating to groundwater are required.

While plant uptake can bring dissolved contaminants to the surface where they can become incorporated into plant biomass, water loss from the soil, through passive or active evaporation processes, can lead to a surface accumulation of previously distributed chemicals. This could have a significant effect on contaminant migration and remobilization. In an experimental and modeling study of $^{129}I$ migration in an unsaturated soil with a shallow water table, Elrick et al. (1997) demonstrated the importance of evaporation in the upward migration and surface accumulation of the contaminant over a 4-yr period. Although the COCs are somewhat deeper than the optimum depth for passive evaporation processes to impact transport, active processes in which water is removed from the soil could serve a role in mitigating further transport. Accounting for these processes would require a non-isothermal simulation and consideration of evapotranspiration. At this stage of the investigation, a decision was made to ignore these processes.

## 2.4 Summary of Conceptual Model

With the features, events, and processes described above, a conceptual model can be developed for the subsurface transport at the 216-B-26 trench. Of the numerous contaminants reported in the list of COCs for the BC cribs and trenches, the ones considered the most capable of contaminating groundwater in the future appear to be $^{238}U$, $NO_3^-$, and $^{99}Tc$. Of these three, $^{238}U$ is the least mobile and in the absence of a significant change in site geochemistry, it would remain strongly sorbed. The greatest risk, therefore, comes from $NO_3^-$ and $^{99}Tc$, the most mobile of the contaminants.

Several intentional waste discharges occurred within the 200-TU OU beginning in 1956 and continuing into 1958. By combining the waste-release history for each trench, a gross chronological conceptual model of composite contaminant release to the vadose zone and subsequent distribution can be generated. The earliest releases occurred in 1956 in Trench 216-B-28. The subsequent migration through the vadose zone varied greatly because of the differences in liquid volumes released and perhaps local stratigraphy. High-resolution neutron probe data suggest a highly stratified medium with numerous thin fine-textured layers in the top 12 to 15 m. Essentially all of the reactive species (uranium, phosphate) were retained within the top 12 m (40 ft), close to the point of discharge. Distributions of electrical conductivity and mobile species ($Cl^-$, $NO_3^-$, $^{99}Tc$) were concentrated in a region between 25 and 45 m, dissected by a low concentration and conductivity zone at about 35 m.

Given the large volume of fluids, and their potentially high density, flow was initially vertical. The wetting front soon became asymmetric, spreading beyond the dimensions of the trench. The strong lateral migration resulted from the combination of local stratigraphy (Figure 2.1) and the large liquid discharges from the adjacent trenches that created a strong horizontal gradient. It is likely the cumulative effect of discharges from the adjacent trenches that finally led to penetration of the near surface capillary breaks. The bimodal nature of the mobile contaminant plumes reflects the series of discharge events. The leading

and trailing edges of the plume were initially from the same liquid release event and likely showed similar peak concentrations. After the leading edge crossed the coarse-textured zone at 35 m, soil water suction decreased to a point where further downward migration of the trailing section was curtailed. This resulted in a relatively low concentration zone between the 34-m and 37-m depths. The leading edge continued its downward movement but was finally stopped by another capillary break formed by the fine over coarse sequence at 47 m.

The lower peak concentration in the leading edge is likely caused by a combination of lateral spreading above the lower capillary break and the accumulation of contaminants above the 33.5-m depth. The absence of any significant concentrations of mobile species above the main plume suggests that the upper section has been effectively leached by subsequent natural recharge. This is supported to some extent by the vertical distribution of electrical conductivity and pH at the C4191 borehole. It is possible that the absence of any major recharge events or subsequent liquid discharges that could overcome the capillary break at 33.5 m is responsible for the contaminants accumulating in this region above this coarse-textured zone and resulting in higher concentrations in the trailing edge of the plume. Equalization of the concentrations in the two sections would require a significant decrease in water suction to overcome the water-entry pressure of the separating capillary break. Thus, remedial actions that reduced recharge would effectively slow down the mean vertical migration. It should be noted that reliance on data from a single borehole makes it virtually impossible to predict whether this zone extends across the entire site. Thus, the bimodal nature of the plume could be a local artifact specific to the borehole location, which means that the plume could show different characteristics at different locations.

Past assessments of subsurface transport have ignored the heterogeneity that could lead to the distributions observed at 216-B-26. The hydrogeologic units were typically assumed to be homogeneous and isotropic in character, although in reality, these units display very a complex small-scale structure. It is now well known that the dominant effect of these complex structures is to enhance lateral spreading and impede downward migration. Thus, accurate simulation of flow and transport must account for the small-scale stratigraphy with adequate description of saturation-dependent anisotropy mechanisms. The properties of many fluids discharged at Hanford were typically different from those of pure water. For example, the specific gravity of wastes that have leaked from single-shell tanks ranged from 1.1 to 1.65, which could enhance the transport of contaminants. Increased density has been demonstrated to elongate contaminant plumes vertically and reduce lateral spreading caused by stratigraphic variations in hydraulic properties (Ward et al. 1997; Ward et al. 2002). However, in the interest of simplifying the conceptual model, fluid effects are ignored.

A representative flow-and-transport model of the BC trenches was therefore developed to be multidimensional and included the following features:

- Representation of the small-scale stratigraphy and the site-specific ranges in physical and chemical properties (based on available geologic, soil physics, and geochemical data from nearby boreholes and outcrops)

- Tilted layers to accommodate the natural slope to the formation. Observations at the near-by 299-E24-111 test site suggest a southeasterly dip in the fine-textured layers.

- Representation of lateral spreading along multiple strata with contrasting physical properties (e.g., bedding contacts), which appears to be prevalent within the fine-grained lenses. Lateral spreading can be enhanced by the sloped layers.

Accounting for these features required information on hydraulic and transport properties at a scale that is not typically available. A major challenge, therefore, was in determining flow-and-transport parameters for the small-scale lithofacies. Because the geometry and configuration of various hydrostratigraphic facies and heterogeneities could be adequately characterized, the effects of these features were captured through their impact on the specific retention. A relationship between the specific retention and sediments particle size statistics allowed identification of changes in sediment texture. Properties for the different textures were derived from pedotransfer functions using a combination of data from site measurements (Khaleel and Freeman, 1995; Reidel and Horton, 1999; Murray et al, 2003), and other published data (e.g. Rawls et al., 1982; Carsel and Parrish, 1988) from which relationships between size statistics and hydraulic properties could be derived. For this analysis, it is assumed that water flow can be described by the Richards' equation with gravity and capillary potential gradients.

# 3.0 Technical Approach

This analysis focuses on four major transport elements: 1) contaminant inventory distribution, 2) vadose zone transport, 3) the impact of contaminant concentrations on the quality of groundwater beneath the BC trench field, and 4) the potential impact of remediation alternatives. To estimate the potential concentration of contaminants in the groundwater from the existing inventory distributions, it is necessary to link the inventory distribution with a vadose zone transport model. In general, there are two approaches that can be used to achieve this linkage.

In the first approach, the existing contaminant inventory distribution can be superimposed or convolved with an applicable transport model to predict its transport through the vadose zone under different conditions. This approach requires identifying of the appropriate conceptual model and identifying or developing a system output or response function that can be easily superimposed or convolved with the existing contaminant-inventory distribution. System-response functions, based on analytical solutions to the CDE for 1-D advection and dispersion and for 1-D advection with 2-D dispersion, are readily available in the literature (van Genuchten and Alves 1982; Jury and Roth 1990; Leij et al. 1991). The analysis is focused on estimating the travel times and concentrations at the water table for the non-adsorbed chemicals, such as $^{99}Tc$ and $NO_3^-$.

With the available data limited to a single borehole, initialization of a multidimensional transport model to predict future migration would be a difficult task. The second approach therefore requires simulation of the current contaminant inventory distribution with an appropriate process model using a reconstructed release history. One way to overcome this limitation is to first simulate the distribution of the plume at the time of sampling. The existing plume is then modeled to determine future contaminant migration through the vadose zone and travel time to the unconfined aquifer. This is the approach of choice for complex boundary conditions and heterogeneous subsurface domains in which flow and transport can be transient and multidimensional. This approach also requires identifying the appropriate conceptual model. However, the system response is based on numerical solutions to the Richards' flow equation for variably saturated flow and the CDE for multidimensional advection and dispersion. For this approach, we chose the STOMP simulator developed at Pacific Northwest National Laboratory (PNNL) (White and Oostrom 2000). Modeling the transport of near-surface contaminants in vegetated waste-management areas should consider plant water uptake as well as the potential uptake of COCs if accurate estimates of quantities migrating to groundwater are required. STOMP has capabilities for simulating water loss by evapotranspiration. However plant water uptake was not modeled, instead a constant flux boundary at the surface was specified using the net recharge rate, calculated as the gross precipitation corrected for evaporation and transpiration. Uptake of COCs was also ignored. The analysis is therefore focused on estimating the time required to transport non-adsorbed chemicals, such as $^{99}Tc$ and $NO_3^-$, through the vadose zone to the water table. Data taken from a borehole C4191 drilled near the center of trench B216-B26 (Serne and Mann 2004) were compared with model simulations based on known inventory (discharge volume and concentrations) and estimated recharge rates for the BC trench site.

## 3.1 Transport Under Steady-Flow Conditions

An analytical solution to the CDE was used to examine the rate at which a finite amount of a contaminant initially present in the soil either accumulates at the surface or leaches downward under steady-state flow

conditions. In this analysis, expressions derived by Elrick et al. (1997) were used to describe the spatial and temporal distributions of the resident concentrations of a subsurface pulse input of contaminant. These expressions can take into account linear adsorption and first-order decay as well as the effects of a depth-dependent water-content distribution that is assumed to be invariant with time. Equations for the equilibrium distribution near the surface during evaporation and for movement toward the water table were used to describe the behavior of finite amounts of the contaminant initially present in the system.

Use of this model required certain simplifying assumptions: 1) the soil column is semi-infinite, 2) the transport and chemical properties of the soil are homogenous and isotropic, 3) the initial distribution of contaminant in the soil is non-uniform and given by *f(z)*, 4) the flux density of water is constant, 5) the water content can either be constant with depth or vary with depth, 6) the solute flux is zero at the soil surface and therefore no chemical is lost by evaporation, 7) there is no preferential flow, and 8) where appropriate, constant linear adsorption and first-order chemical decay are assumed.

### 3.1.1 Solution for Contaminant Inventory at Depth, h

For an initial ($t = 0$) depth distribution of contaminant given by

$$C_R(z,0) = f(z);\ z \geq 0 \tag{3.1}$$

the solution to the CDE can be derived in terms of a reduced resident concentration or probability density function, $f_R^{(\delta-h)} = C_R / A_{CL}$, where $A_{CL}$ is the area under the $C_R$ versus depth, $C_R(z)$. $C_R$ is the resident solute concentration as a function of depth $z$ at the time of sampling, i.e., $t$=0, in pCi/m$^3$ or μg/m$^3$. By defining the initial contaminant distribution in terms of $f(z) = \delta(z–h)$, the probability density function of the resident concentration for a soil in which the water content is constant with depth is given by Elrick et al. (1997).

$$\begin{aligned} f_R^{(\delta-h)} &= \frac{1}{2\sqrt{\pi D_z t}} exp\left[\frac{-(z-h-vt)^3}{4D_z t}\right] \\ &+ \frac{1}{2\sqrt{\pi D_z t}} exp\left[\frac{vz}{D_z} - \frac{(z+h+vt)^2}{4D_z t}\right] \\ &- \frac{v}{2D_z} exp\left(\frac{vz}{D_z}\right) erfc\left[\frac{z+h+vt}{2\sqrt{D_z t}}\right] \end{aligned} \tag{3.2}$$

In Equation (3.2)

$h$ = mean depth of the contaminant spike
$D_z$ = longitudinal hydrodynamic dispersion coefficient
$z$ = depth from the surface
$h$ = depth of the contaminant plume
$v$ = pore water velocity
$t$ = time.

For spatially invariant water content, the spatial components of the hydrodynamic dispersion coefficient include dispersive and diffusive elements and are given by

$$D_z = \alpha_z v + D_m \tag{3.3}$$

where $\alpha_z$ is the dispersivity in longitudinal direction, and $D_m$ is the molecular diffusion coefficient.

Equation (3.2) is applicable to homogeneous sediments or sediments in which water content is constant with depth, i.e. $d\theta(z)/dz = 0$. However, spatially invariant water-content profiles are seldom found in field soils. For such conditions, Elrick et al. (1997) derived a solution to the CDE for variable $\theta(z)$ by transforming the space variable in the CDE to a water-storage term and the time variable to $q^*t$. These transformations gave rise to an equivalent dispersion coefficient,

$$D^* = [\theta(z)]^2 \cdot D = \overline{\theta}^2 D \tag{3.4}$$

where $\overline{\theta}$ is the average water content, and $D^*$ is assumed to be constant. A more general solution for the steady-state distribution given a depth-dependent water content, $\theta(z)$, is then given by

$$\begin{aligned} f_R^{(\delta-h)} = & \frac{\theta(z)}{2\sqrt{\pi D_z t}} exp\left[ \frac{-\left( \int_0^z \theta(z)\,dz - \int_0^h \theta(z)\,dz - qt \right)^2}{4D_z t} \right] \\ & + \frac{\theta(z)}{2\sqrt{\pi D_z t}} exp\left[ \frac{q\int_0^z \theta(z)\,dz}{D_z} - \frac{\left( \int_0^z \theta(z)\,dz + \int_0^h \theta(z)\,dz + qt \right)^2}{4D_z t} \right] \\ & - \frac{\theta(z)q}{2D_z} exp\left( \frac{q\int_0^z \theta(z)\,dz}{D_z} \right) erfc\left[ \frac{\left( \int_0^z \theta(z)\,dz + \int_0^h \theta(z)\,dz + qt \right)^2}{2\sqrt{D_z t}} \right] \end{aligned} \tag{3.5}$$

In Equation (3.5), $\theta(z)$ is the volumetric water content as a function of depth, $z$; and $q$ is the constant flux density of water. The remaining variables are as defined above in Eq (3.1).

### 3.1.2 Accumulation of Contaminant Under Steady Evaporation

At long times, as $t \to \infty$, $\delta C_R/\delta t \to 0$, and the CDE reduces to

$$\frac{dC_R}{dz} - \frac{v}{D_z} C_R = 0 \tag{3.6}$$

The solution to Equation (3.5) is given by

$$\frac{C_R}{A_{CL}} = f_R^{(\delta-h)} = -\frac{v}{D_z} \exp\left( \frac{vz}{D_z} \right) \tag{3.7}$$

Equation (3.2) also reduces to Equation (3.5) for t $\rightarrow \infty$, giving the equilibrium distribution of contaminant as a function of depth. Under steady evaporation, *v* is negative, and the upward convective flow counteracts the downward dispersion. The resulting distribution is controlled solely by the ratio $v/D_z$. For a depth-dependent water-content profile, $\theta(z)$, the applicable relationship is given by

$$f_R^{(\delta-h)} = -\frac{q}{D_z} exp\left( \frac{q\int_0^z \theta(z)\,dz}{D_z} \right) \tag{3.8}$$

### 3.1.3 Concentration Crossing the Water Table Based on an Arbitrary Initial Distribution

The concentration crossing a compliance plane at depth *z*, defined by the water table, is equivalent to a flux concentration and is derived from the resident concentration probability density function using the following relationship (Jury and Roth 1990):

$$f_F = f_R - \frac{D_z}{V}\frac{\partial f_R}{\partial z} \tag{3.9}$$

Thus, the $f_F$ can be expressed as

$$\begin{aligned} f_F^{(\delta-h)} &= \frac{CF}{A_{CT}} = \\ &\frac{v}{4\sqrt{\pi D_z t}} exp\left[ \frac{-(z-h-vt)^2}{4D_z t} \right] - \frac{v}{4\sqrt{\pi D_z t}} exp\left[ \frac{vz}{D_z} - \frac{(z+h+vt)^2}{4D_z t} \right] \\ &+ \frac{(z-h)}{4\sqrt{\pi D_z t}} exp\left[ \frac{-(z-h-vt)^2}{4D_z t} \right] + \frac{(z+h)}{4\sqrt{\pi D_z t}} exp\left[ \frac{vz}{D_z} - \frac{(z+h+vt)^2}{4D_z t} \right] \end{aligned} \tag{3.10}$$

where $A_{CT}$ is the area under the *C(t)* curve obtained from $\int_0^\infty C(t)\,dt$. For the depth-dependent water-content profile, the equation for the flux concentration crossing a compliance plane at depth *z* is then given by

$$f_F^{(\delta-h)} = \frac{C_F}{A_{CT}} =$$

$$\frac{q}{4\sqrt{\pi D_z t}} exp\left[\frac{-\left(\int_0^z \theta(z)\,dz - \int_0^h \theta(z)\,dz - qt\right)^2}{4D_z t}\right]$$

$$-\frac{q}{4\sqrt{\pi D_z t}} exp\left[\frac{q\int_0^z \theta(z)\,dz}{D_z} - \frac{\left(\int_0^z \theta(z)\,dz + \int_0^h \theta(z)\,dz + qt\right)^2}{4D_z t}\right]$$

$$+\frac{\left(\int_0^z \theta(z)\,dz - \int_0^h \theta(z)\,dz\right)}{4\sqrt{\pi D_z t}} + exp\left[\frac{-\left(\int_0^z \theta(z)\,dz - \int_0^h \theta(z)\,dz - qt\right)^2}{4D_z t}\right]$$

$$+\frac{\left(\int_0^z \theta(z)\,dz - \int_0^h \theta(z)\,dz\right)}{4\sqrt{\pi D_z t}} exp\left[\frac{q\int_0^z \theta(z)\,dz}{D_z} - \frac{\left(\int_0^z \theta(z)\,dz + \int_0^h \theta(z)\,dz + qt\right)^2}{4D_z t}\right] \quad (3.11)$$

Having defined the probability density functions for the different conditions, the convolution solution is defined simply as

$$C(z,t) = \int_0^z C_i(h,0)\, f_i^{(\delta-h)}(z,t,h)\,dh \quad (3.12)$$

where $C_i(h,0)$ is the initial distribution of contaminant inventory in the soil at time $t = 0$ (time of sampling) and $f_i^{(\delta-h)}$ is the probability density function of the resident ($i = R$) or flux ($i = F$) concentrations defined in Equations (3.2) and (3.5) and in (3.10) and (3.11). With this convolution approach, potential impacts to the groundwater can be easily determined for arbitrary inventory distributions and steady-state water-content ($d\theta(z,t)/dt = 0$.profiles. The probability density functions given in Equations (3.2) and (3.5) and Equations (3.10) and (3.11) form the basis of analytical solutions for more complex inventory distributions that can be obtained by convolution. Depending on the complexity of the initial distribution, the solution of the convolution integral may be obtained by analytical or numerical methods. Thus, convolution can be used to quickly estimate the system response to different inventory distributions and parameter sets. It should be noted, however, that these relatively simple solutions are based on the assumption of steady flow in very complex natural systems in which flow is typically transient. The concentrations predicted at the compliance plane are also leachate concentrations and are therefore not representative of the concentration at a receptor well. Concentrations at a receptor well can be estimated through the subsequent application of an analytical groundwater model or the EPA's soil screening level approach in which a dilution attenuation factor can be used to predict concentrations at a receptor down-gradient of the waste site.

### 3.1.4 Spatial Moment Analysis

In the absence of complex state-variable models, a particularly useful method for analyzing spatial data is the method of spatial moments. Spatial moments allow a simple, physically meaningful description of

overall plume behavior, and in contrast to the state-variable models, moments can be predicted with less uncertainty. The absolute n$^{th}$ spatial moment of resident concentration profile, $C_R(z)$, is defined as

$$M_n = \int_0^L z^n \, C_R(z) \, dz \tag{3.13}$$

The normalized n$^{th}$ spatial moment about the mean of the distribution $C_R(z)$, $m_n$, is defined as

$$m_n = \frac{\int_0^L (z - \bar{z})^n \, C_R(z) \, dz}{\int_0^L C_R(z) \, dz} \tag{3.14}$$

where the denominator is the zeroth moment, $M_0$, which is equivalent to $A_{CL}$. The zeroth moment, $M_0$, is unique in that under conditions when it exists, its value is proportional to the total aqueous phase mass contained in the plume. For tracers, it depends only on the amount of mass injected and the volumetric flow rate; it is independent of the duration of the injection. The first moment, $m_1$, measures the mean location of the plume, which when divided by the mean travel time gives the mean pore-water velocity. The first moment can therefore be used to estimate the mean recharge rate using the following relationship

$$q = \theta_{eff} \cdot v = \theta_{eff} \cdot \frac{m_1}{t} \tag{3.15}$$

where $\theta_{eff} = L^{-1} \int_0^z \theta(z) \, dz$ is the effective water content from the surface to a maximum sampling depth, $L$. The second moment, $m_2$, measures the amount of spreading about the center of mass, $m_1$. Higher moments ($m > 2$) can be calculated but traditionally they are avoided because they are difficult to obtain experimentally and also to interpret. To characterize the $^{99}$Tc concentration profile obtained from the C4191 borehole, the zeroth, first, and second moments were determined.

The convolution solution defined by Equation (3.12) was used in a two-step approach to evaluate the impact of the contaminant inventory on groundwater quality. First, spatial moment analysis was applied to the $^{99}$Tc concentration profile obtained from the C4191 characterization borehole to determine $A_{CL}$ and to calculate the probability density function, $f_R^{(\delta - h)}$, according to Equation (3.7). The analysis of the spatial moments was then extended to $f_R^{(\delta - h)}$ to locate the center of mass and to determine the amount of spreading about the center of mass. The first moment was used to calculate the mean recharge rate, $q$, between the operation of the 216-B-26 Trench and the installation of the borehole. In addition, the data were fitted to the convolution model by inverse methods to determine the effective dispersion coefficient and pore-water velocity. The current water-content profile, $\theta(z)$, was assumed to be steady and representative of an equilibrium condition. Redistribution of the existing plume, including the time needed to reach the water table, was then simulated using the 1-D analytical model under different recharge rates and the effect of different remedial options evaluated. Travel times for releases to the groundwater were calculated as the time at which the center of mass reaches the water table. Analysis of steady transport with the analytical convolution solutions was conducted using MathCAD.

## 3.2 Transport Under Transient Flow Conditions

Simulating the effects of time-varying surface recharge and operation of the trenches required a transient flow solution to be executed with the solute transport calculations. The transient flow-and-transport simulations were initiated using a steady flow solution to the boundary-value problem using the initial boundary values. To simplify the simulations, no attempt was made to account for short-term temporal variations in recharge that would result from temporal variations in natural precipitation. However, recharge rates were allowed to vary between the period before operation of the trenches, during the operation of the trenches, and post operation. Solutions for the transient flow-and-transport problem were obtained numerically using the STOMP simulator in a three-phase approach.

The first phase was meant to simulate the period before construction and operation of the trenches and was used to establish the initial flow condition for subsequent simulations. The initial condition was obtained by simulating steady flow from time zero to the year 1956 with a constant recharge rate representative of the pre-operations phase. The simulation was executed as a transient simulation starting from a unit-gradient initial condition to a steady flow condition in which the surface recharge rate was assumed to be constant. Establishment of the initial condition focused only on the subsurface distribution of water as it was assumed that the contaminant inventory of the radioactive COCs was zero.

In the second phase, the steady flow solution was used as an initial condition for the six transient flow and solute transport cases investigated in this study. To best represent conditions at the site, the transient simulations were simulated in two stages. In the first stage, flow and solute transport were simulated with opened trenches that were subject to natural precipitation. In this stage, nodes representing the trenches were inactive, and the required boundary condition was applied over the trench bottom. The second stage represented the period after trench operations following backfilling of the trenches. During this stage, the inactive trench nodes were converted to active nodes with a material type identical to that surrounding the trenches.

Simulation results were written to three types of output files: 1) files echoing the input and reference node file, 2) a series of plot files to allow tracking of the time history of the plume, and 3) a series of surface-flux files to track the flux of water and contaminants across the water table. The echo of the input and reference node file contains a translation of the input files as interpreted by the simulator (e.g., with unit conversions) and a time sequence of the simulation history and chosen variables (e.g., aqueous pressure, moisture content, solute concentrations, Darcy fluxes) at selected grid locations. Plot files contain variable data for all grid points at selected simulation times. These files are used to generate color-scaled plots and animations through Tecplot.[(a)] A utility program, *PlotTo.pl*, was used to translate STOMP plot files into Tecplot-formatted input files. Surface-flux files contain rate and integral information about fluxes crossing user-defined internal or external boundaries. Solute fluxes and aqueous fluxes across the water table are used to calculate average solute concentrations and source rates. Surface-flux files are also used to generate rate and integral plots of solutes exiting the computational domain and entering the groundwater. A utility program, *SurfaceT.pl*, was used to translate STOMP surface-flux files into formatted input files suitable for plotting. The steady flow and transient simulations were executed on a Linux workstation. For compatibility between platforms, the input, zonation, and inventory files were maintained as ASCII formatted files.

(a) Amtec Engineering, Inc. 2002. Tecplot, Version 9.0. Bellevue, WA.

## 3.3 Solution Domain

The physical domain considered for the simulation is a 2-D north-south cross section through trenches 216-B-52 at the north to 216-B-28 to the south. This section, which is equivalent to section Q`-Q`` in Fecht et al. (1978) provided the gross stratigraphy for the site. Small-scale heterogeneities were derived from grain-size distributions used in conjunction with high-resolution neutron logs from surrounding boreholes. The physical domain was first discretized using a Cartesian grid with variable horizontal and vertical spacing. On average, grid blocks were on the order of 1 m, but were reduced to as little as 0.15 m in fine-textured lenses and at layer interfaces.

Two types of input are required for STOMP simulations: 1) a simulation control and soil material definition file and 2) a zonation file describing the site stratigraphy. The data required to generate these files were derived from a number of sources. Soil zonation was inferred from grain-size analysis of samples from the C4191 borehole, from the geologist's description of grab samples, and visual observation of high-resolution grab-sample photos. These methods led to the identification of six major textural classes for the site. Inevitably, this approach resulted in a layer-cake model with the thin intercalations extending to the domain boundaries. To overcome the limitations of such a stratigraphic model, we made use of geostatistical simulation techniques.

The conditional probability distribution of the soil water content within the computational domain was estimated from a series of equi-probable realizations generated by stochastic simulation. The sequential Gaussian simulation routine **SGSIM** from **GSLIB** (Deutsch and Journel 1998) was used to generate a set of realizations of volumetric water content on a 70 by 1317 node mesh of the computational domain. The parameters of the variogram models developed for the 299-E24-111 Experimental Test Well (Sisson and Lu) Site located in the eastern section of the 200 Area Plateau of the Hanford Site were used as input in the sequential Gaussian simulation. The variogram model for the 299-E24-111 site show that the maximum direction of continuity was in the northeast direction (22.5 degree) with a range on the order of 100 m. The southeast direction (112.5) showed a trend and a much shorter range of about 15-20 m.

The field-measured water contents were assumed equivalent to the specific retention, which is controlled by texture. These data were used to estimate grain-size statistics, which were in turn used to estimate hydraulic properties for the six soil classes using pedotransfer functions. These properties were then converted to the appropriate input information from the STOMP input cards. Graphical representations of the stratigraphy and trenches were converted to soil zonation maps based on a tilted Cartesian grid. Transport property data for the mobile COCs and the eight major textures were also converted for inclusion in the STOMP input cards. The conceptual model was completed by converting boundary conditions and sources into a form that could be used by the model for controlling execution intervals and output generation.

Temporal variations in natural surface recharge and discharges to the trenches required a transient flow solution to be executed with the transport calculations. The transient simulations were initiated using a steady flow solution to the boundary value problem using the initial boundary values. This approach neglected time variations in surface recharge before the start of the simulation. The pre-operations condition was simulated as a transient flow problem, starting with a unit-gradient initial condition, which was run out to a time where flow became steady at the recharge rate of interest. In general, running the model from year zero to the year 1945 was sufficient to achieve steady flow conditions. These conditions

are taken to represent site conditions before the trenches were installed. Solute transport was ignored in this phase of the simulation, and contaminant concentrations were assumed to be zero.

The steady flow solution was then used as an initial condition for the 5 transient flow and solute transport cases analyzed in this study. Simulations were conducted in two stages. In the first stage, flow was simulated with the trenches opened. In this stage, nodes representing the trenches were inactive and recharge was applied directly to the trench bottom. In the second stage, once waste discharges ceased, the trench nodes were converted to active nodes with a material type identical to that surrounding the trenches.

Simulation results were written to three types of output files: 1) a reflected input and reference node file, 2) a series of plot files, and 3) a series of surface-flux files. The reflected input and reference node file contains a translation of the input files as interpreted by the simulator (e.g., with unit conversions) and a time sequence of the simulation history and chosen variables (e.g., aqueous pressure, moisture content, solute concentrations, Darcy fluxes) at selected grid locations. Plot files contain variable data for all grid points at selected simulation times. A number of utilities were developed in-house to convert STOMP plot files into specially formatted input files for graphical presentation using commercial software tools (Tecplot). These files were used to generate contour plots of the primary variables. Surface-flux files contain rate and integral information about fluxes crossing user-defined internal or external boundaries. Solute fluxes and aqueous fluxes at the water table were used to calculate average leachate concentrations and source rates out of the vadose zone into the water table. Surface-flux files were also used to generate breakthrough curves at a hypothetical receptor well 100 m south of the 216-B-28 trench.

## 3.4 Model Parameterization

No measurements of flow-and-transport parameters were available for the BC Crib site, and no samples were collected to determine these parameters during the sampling phase. Meteoric recharge and parameters for vadose zone flow and transport were developed by PNNL based on published site data and experiments conducted onsite. Flow-and-transport parameters were assigned based on the similarity between grain-size statistics of the different soil textures at the site and at previously characterized sites. These parameters (Table 3.1 and Table 3.2) and the rationale for their selection are presented below.

### 3.4.1 Recharge Rates

Groundwater recharge is representative of the soil water flux through a waste zone to the water table and thus strongly impacts estimated rates of contaminant leaching and remobilization that may occur. Understanding the recharge process and the conditions under which it occurs is therefore of critical importance to evaluating contaminant fate and transport. In general, only a few millimeters or less water will move beyond the root zone of vegetated semi-arid and arid ecosystems each year. Nevertheless, recharge on the Hanford Site is quite variable, ranging from 50 to 100 mm $yr^{-1}$ on bare surfaces to less than 0.1 mm $yr^{-1}$ on surfaces vegetated with shrubs (Fayer and Szecsody 2004; Last et al. 2004). For the pre-Hanford period, the plant community was assumed to be sagebrush, and a recharge rate of 3.5 mm/yr was used. This is slightly less than the 4.2 mm $yr^{-1}$ derived from Burbank loamy sand at a site 1 km north of the ILAW site (Prych 1998).

The actual recharge rates for the BC trench site during operations is unknown but may be estimated from the transport behavior of $^{99}$Tc using a combination of spatial moment analysis under the assumption of steady-state transport. The $^{99}$Tc profile, which represents a resident concentration, $C_R(z)$, was first integrated over depth to determine $A_{CL}$ and to calculate the probability density function, $f_R^{(\delta-h)}$. The normalized n$^{th}$ spatial moments were then calculated according to Equation (3.14). The first moment, $m_1$, which locates the center of mass, was then used to estimate the travel time and recharge rate according to Equation (3.15). The effective water content in Equation (3.15) was calculated by integrating the laboratory-measured $\theta(z)$ from the surface to the base of the $^{99}$Tc plume, which was assumed to be at 53.34 m. Table 3.1 summarizes the estimated recharge rates based on the moment analysis method.

**Table 3.1. Estimated Recharge Rates Based on the $^{99}$Tc Profile**

| Plume | Mean Depth (m) | Δt (yrs) | $\bar{v}$ (m/yr) | $\theta_{eff}$($m^3m^{-3}$) | q mm/yr |
|---|---|---|---|---|---|
| Intact | 33.778 | 47.016 | 0.7184 | 0.0910 | 65.3784 |
| Trailing | 29.838 | 47.016 | 0.6346 | 0.0910 | 57.7515 |
| Leading | 39.674 | 47.016 | 0.8438 | 0.0910 | 76.7899 |

Estimated recharge rates range from 57.7 mm yr$^{-1}$ to 76.79 mm yr$^{-1}$ for the deconvolved plume and equaled 65.378 mm yr$^{-1}$ for the intact plume. It is unlikely that the bimodal nature of the plume resulted from a superposition of different input pulses. The layer sequence in the plume constitutes a capillary break; thus, the plume separation is most likely due to a decrease in suction to a value less than the water entry pressure of the coarse layer after the leading edge passed. This would have effectively stopped the further downward migration of the trailing section. If this is the case, the recharge rates from the deconvolved plume would be best for estimating the mean recharge rate during operations. Thus, the estimated recharge rate during trench operations is 77 mm yr$^{-1}$, rounded up from the 76.7899 mm yr$^{-1}$ in Table 3.1.

The recharge rate after trench closure is also unknown. It is likely that vegetation would not have been allowed to become established. Site data for unvegetated Hanford sand contained in a 7.6-m-deep lysimeter suggest an average rate of 55.4 mm yr$^{-1}$ (Fayer and Walters 1995; Fayer and Szecsody 2004). Data from the Hanford barrier show an average recharge of 27.6 percent of annual precipitation from sparsely vegetated side slopes. A rate of 22.3 mm yr$^{-1}$ is chosen for the period 1958 to 1982 when the trenches were stabilized. This was based on observations of decreasing drainage from a sparsely vegetated side slope at the prototype Hanford Barrier reported by Fayer and Szecsody (2004). Recharge after remediation and closure of the site will depend on the chosen remedy. Depending on the remedial action, recharge rates could range from the post-operational 22.3 mm yr$^{-1}$ in a no-action alternative to less than 0.5 mm yr$^{-1}$ for a multilayered capillary barrier such as the Hanford barrier.

### 3.4.2 Flow-and-Transport Properties

Hydraulic properties were estimated based on similarities in grain-size statistics (mean grain size and sorting index) between sediments at the BC Crib site and other characterized sites at Hanford using pedotransfer functions. Grain-size distributions were obtained from the ROCSAN database while measured hydraulic properties were obtained from databases for the immobilized low-activity waste

(ILAW) and Sisson and Lu sites. Fluid flow parameters for the vadose zone include soil-moisture-retention characteristics and saturated hydraulic conductivity. Variable or saturation-dependent anisotropy provides a framework for simulating the effects of saturation on lateral spreading. A recently developed model for saturation-dependent anisotropy attributes differences in direction permeability to directional differences in tortuosity and pore-connectivity. The connectivity parameter ($L$) for the different sediments was derived from centrifuge measurements made on undisturbed directional cores.

Table 3.2 lists the estimated Brooks-Corey parameters for the various strata and the aquifer at the BC trench site. The results of grain-size statistical analyses were used in pedotransfer functions developed for published hydraulic properties to predict properties on a resolution of 3 inches. Solute transport parameters include bulk density, diffusivity, sorption coefficients, and macrodispersivity. Bulk density for the different sediments was also derived from pedotransfer functions. Aquifer hydraulic parameters were assumed to be similar to those identical to those under the B, BX, and BY Tank Farms and used in the simulations for the field investigation report (Freedman et al. 2002). The saturated hydraulic of the aquifer was assumed to be invariant with a value of 1615 m/day in the horizontal direction and 161.5 m/day in the vertical direction. The saturated water content was also assumed to be spatially invariant with a mean value of 0.2688 $m^3$ $m^{-3}$. Aquifer parameters are shown in Table 3.3.

**Table 3.2. Estimated Brooks-Corey Parameters for the Various Strata at the BC Trench Site**

| USDA Texture Class | Mean Diameter (mm) | $\theta_s$ | $\theta_r$ | $\Theta_r$ | $\psi_a$ (cm) | $\lambda$ | $K_s$ cm/hr |
|---|---|---|---|---|---|---|---|
| Sand | 0.6713 | 0.437 | 0.020 | 0.046 | 15.98 | 0.69 | 21.0 |
| Loamy Sand | 0.4357 | 0.437 | 0.035 | 0.080 | 20.58 | 0.55 | 6.11 |
| Sandy Loam | 0.2068 | 0.453 | 0.041 | 0.091 | 30.2 | 0.38 | 2.59 |
| Loam | 0.0576 | 0.463 | 0.027 | 0.058 | 40.12 | 0.25 | 1.32 |
| Silt Loam | 0.0293 | 0.501 | 0.015 | 0.030 | 50.87 | 0.23 | 0.68 |
| Sandy Clay Loam | 0.0915 | 0.398 | 0.068 | 0.171 | 59.41 | 0.32 | 0.43 |
| Clay Loam | 0.0292 | 0.464 | 0.075 | 0.162 | 56.43 | 0.24 | 0.23 |
| Silty Clay Loam | 0.0129 | 0.471 | 0.04 | 0.085 | 70.33 | 0.18 | 0.15 |

**Table 3.3. Aquifer Parameters for the BC Trench Site**

| Parameter | Value |
|---|---|
| Aquifer Hydraulic Conductivity | 1,615 m/day |
| Effective Porosity | 0.26 |
| Hydraulic Gradient | 0.001486 |
| Groundwater Velocity | 0.24 m/day |
| Aquifer Thickness | 5 m |
| Dispersivity | 1.0 m |

### 3.4.3 Bulk Density and Distribution Coefficient

Both bulk density ($\rho_b$) and the distribution coefficient ($K_d$) estimates are needed to calculate retardation factors for different COCs. The effective, field-scale estimate for the distribution coefficient was derived by calculating the average of the small-scale laboratory measurements (Cantrell et al. 2003). The primary COCs in this study are $^{99}Tc$ and $NO_3^-$ with the behavior of $^{99}Tc$ being redox sensitive.

Under oxidizing conditions, $^{99}Tc$ exists as the soluble heptavalent pertechnetate ion, $TcO_4^-$. Owing to its negative charge, pertecnetate is highly mobile in soils and groundwater and is known to show anion exclusion effects (Lieser and Bauscher 1987; Zhuang et al. 1988; Schroeder et al. 1993). The existence of oxidizing conditions, however, does not necessarily result in high mobility. In a study of $^{99}Tc$ transport in unsaturated Chinese loess under artificial recharge, Liu et al. (2001) reported a slight retardation relative to $^3H$. An average retardation coefficient of $1.14 \pm 0.23$ corresponding to an apparent distribution coefficient of $1.98 \pm 0.42 \times 10^{-2}$ mL $g^{-1}$ was calculated for the medium. In general, sorption ratios for natural sediments are of the order of 0.1 mL $g^{-1}$.

Under reducing conditions and in the absence of complexing agents, the tetravalent Tc(IV) ion dominates (Francis et al. 2002). In this oxidation state, $^{99}Tc$ is relatively immobile and can form highly insoluble minerals like $TcO_2$, as well as strong complexes on Al, Fe, and Sb oxides as well as clays (Lieser and Bauscher 1987; Meyer et al. 1991; Haines et al. 1987; Zhaung et al. 1995).

While these findings provide bounds for $K_d$ values that can be used in a sensitivity analysis of fate and transport, there is no current evidence to support the sorption of $^{99}Tc$ in Hanford sediments. Thus, a $K_d = 0$ mL $g^{-1}$ was assumed for this study. The field-scale estimate of bulk density was calculated as the average of small-scale estimates derived using pedotransfer functions. Effective large-scale estimates of bulk density are listed in Table 3.4 for the different soil types.

### 3.4.4 Diffusivity and Dispersivity

Effective, large-scale diffusion coefficients for the different textures were assumed to be a function of volumetric moisture content, expressed with the Millington and Quirk (1961) empirical relation, as shown in Equation (3.16):

$$\boldsymbol{D_e}(\theta) = \boldsymbol{D_o} \frac{\theta^{\frac{10}{3}}}{\theta_s^2} \tag{3.16}$$

where $D_e$ = effective diffusion coefficient of an ionic species
$D_o$ = molecular diffusion coefficient for the species in water
$\theta$ = water content
$\theta_S$ = saturated water content.

The molecular diffusion coefficient for the different species in pore water was derived from literature values (Kemper 1986). In the STOMP model, dispersivity estimates are needed for all COCS. Owing to the hierarchical nature of heterogeneity that exists in natural soils, it has been suggested that dispersivity is dependent on the scale of observation (Beven et al. 1993). There are very few data for Hanford sediments, especially at scales relevant to the current problem. Recent field experiments resulted in the estimation of longitudinal and transverse dispersivities at the Army Loop Road site, but transport

distances were limited to a maximum of 1 m (Ward and Gee 2003). Table 3.4 presents a summary of the texture-dependent values of longitudinal dispersivity recently reported by Perfect et al. (2002). In general, dispersivity increased as the soil textured became finer and as the Brooks-Corey pore-size distribution index, $\lambda$, decreased.

**Table 3.4. Estimated Dispersivity for Different Textural Classes**

| USDA Texture Class | $\alpha_L$(m) | $\alpha_T$(m) |
|---|---|---|
| Sand | 0.0073 | 0.00073 |
| Loamy Sand | 0.0154 | 0.00154 |
| Sandy Loam | 0.0291 | 0.00291 |
| Loam | 0.0516 | 0.00516 |
| Silt Loam | 0.0753 | 0.00753 |
| Sandy Clay Loam | 0.0291 | 0.00291 |
| Clay Loam | 0.0516 | 0.00516 |
| Silty Clay Loam | 0.0681 | 0.00681 |

In heterogeneous soils, the variation of velocity at the field scale tends to be much larger than at the local scale. Thus, dispersivity should be small compared to the field-scale dispersivity. An estimate of field-scale dispersivity was derived from the observed $^{99}$Tc distribution by fitting the concentration data to Equation (3.2). As with hydraulic properties, local-scale longitudinal dispersivities were estimated from grain-size statistics using the data from Perfect et al. (2002). The dispersion process is characterized by a local dispersion tensor, $D$, which is related to the longitudinal and transverse local dispersivity, $\alpha_l$ and $\alpha_t$, respectively (Bear 1972). Transverse dispersivities were assumed to be 10 percent of the longitudinally values. Effective longitudinal and transverse field-scale dispersivities, applicable to both $^{99}$Tc and $NO_3$, were estimated by fitting the observed $^{99}$Tc concentration profile obtained from the C4191 borehole to an analytical solution of the CDE, assuming 1-D advection and 2-D dispersion. The resulting values represent effective values that reflect the total contribution of the various layers.

## 3.5 Input File Generation

Two types of input files were used to drive the STOMP simulator: 1) a simulation control file and material definition (input) and 2) a soil zonation file (zonation). All input files were written and stored in ASCII text format. The simulation control and material definition input files were assembled using a conventional text editor, whereas the zonation file was generated with a utility program.

### 3.5.1 Input File

As described in the STOMP User's Guide (White and Oostrom 2000), the input file is divided into cards that group common data (e.g., solution control, hydraulic properties, output control, boundary conditions).

### 3.5.2 Zonation File

The zonation file is an ordered listing (i.e., i,j,k indexing) of integers that identify the rock/soil type for every grid cell in the computational domain. Inactive nodes were assigned an integer value of zero, and rock/soil types were assigned numbers in accordance with the ordered listing of rock/soil types in the

rock/soil zonation card of the STOMP input file. A single zonation file was created for all simulation cases to cover a 3-D computational domain. The computational domain extended from the area south of Trench 216-B-28, bounded by Well 299-E33-19 north through 216-B-23 to Well 299-E13-8, located north of Trench 216-B-52 (Figure 3.1).

The domain was bounded on the south by Well 299-E13-12 and on the east by Well 299-E13-51. The zonation file was generated using information from the geologist's descriptions of borehole cuttings and geophysical logs. The domain consists of 78 nodes in the x-direction; 71 in the y-direction, and 1322 in the vertical, giving a total of 7,321,236 nodes. The computational domain extended over a distance of 200 m in the west-to-east direction, and 250 m in the north-south direction. The stratigraphy at this site shows extensive layering resulting from an alluvial depositional environment. The water table is located at 103.17 m below the surface and a 5-m thick confined aquifer was assumed beneath the water table. Thus, the vertical extent of the computational domain was set at 108.17 m. The vertical spacing in the current model is 0.075 m, but can be increased by upscaling the properties.

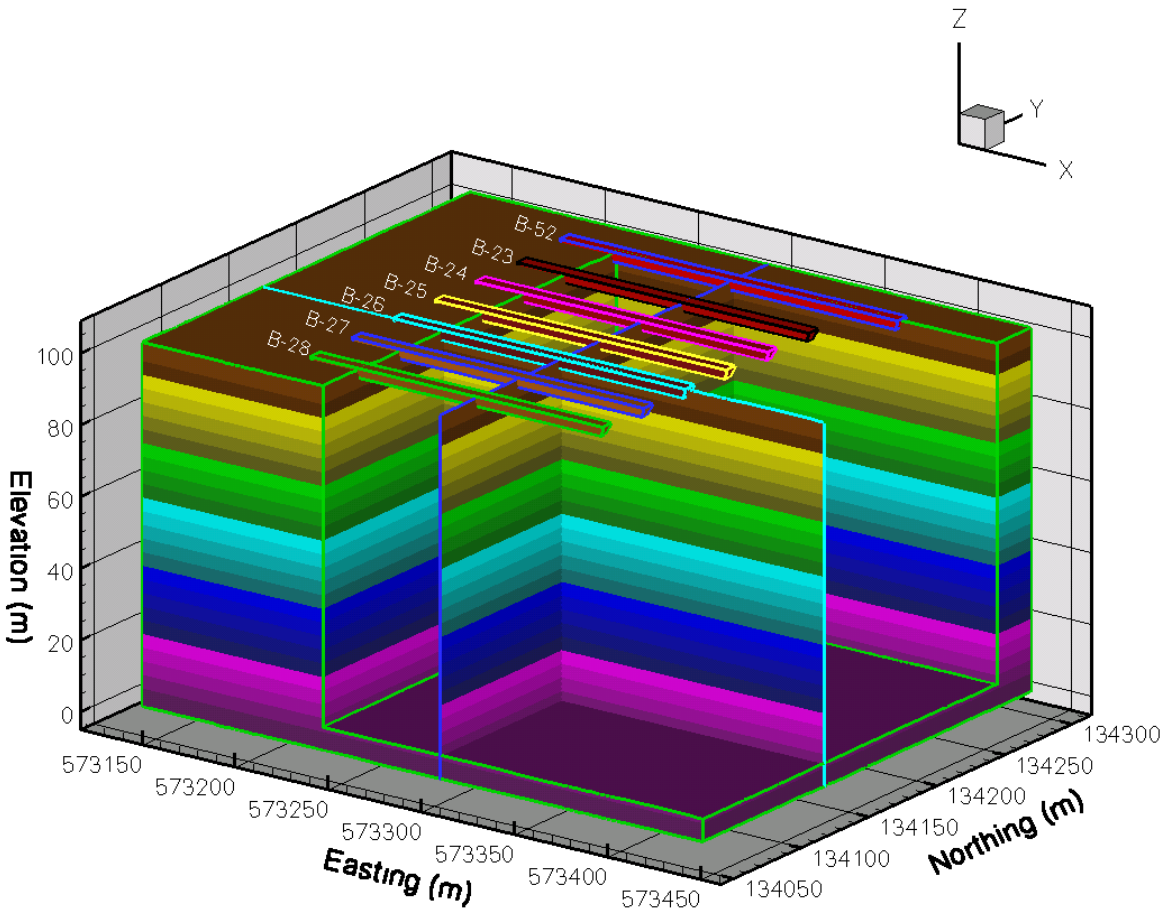


**Figure 3.1. Three-Dimensional Simulation Domain for the BC Trench Site**

The color-coded contour plot of the zonation file for the 2-D domain east-west transect is shown in Figure 3.2. This transect dissects the 216-B-26 Trench and runs parallel to the adjacent trenches. The size of this domain is 78 nodes in the x-direction and 1322 in the vertical, giving a total of 103,116 nodes.

A similar plot for a north-south dissecting the series of trenches is shown in Figure 3.3. This domain consists of 71 nodes in the y-direction and 1322 in the vertical direction, giving a total of 93,862 nodes. Both plots represent the current cross section with the trenches backfilled and covered with "top soil" used for stabilization as described in the waste information data system.

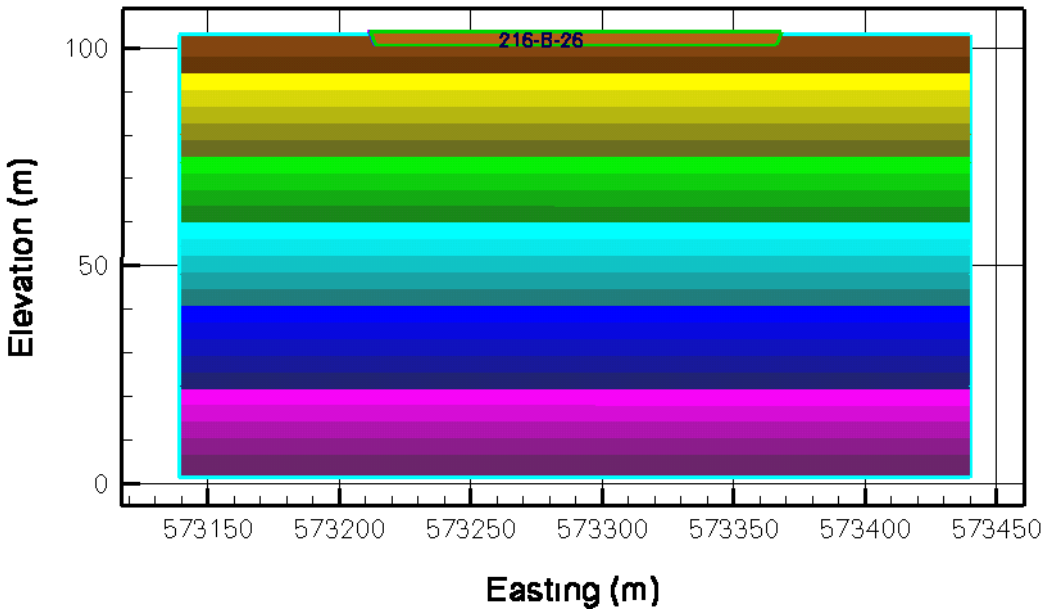


**Figure 3.2. Two-Dimensional Simulation Domain From an East-West Transect Through the 216-B-26 Trench**

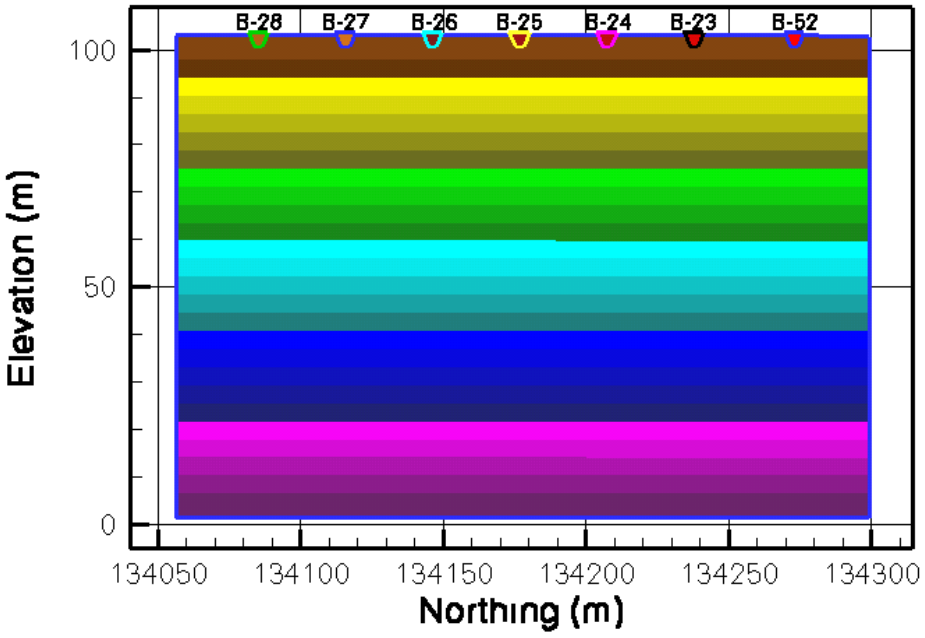


**Figure 3.3. Two-Dimensional Simulation Domain From a North-South Transect Through the BC Trench Site**

### 3.5.3 Boundary Conditions

In all of the simulations, a no-flow boundary was imposed at the bottom of the domain, representing the base of the 5-m thick confined aquifer at 108.17 m. Owing to observation of water leaving the monitored domain at the 299-E24-111 test site via the fine-textured layers (Figure 2.5), the horizontal scale of the modeling domain was increased by 200 m on the side boundaries (north, east, south, and west). These boundaries were designated as zero-flux boundaries for water flow and solute transport. For the 2-D north-south transect, groundwater was assumed to flow in a southerly direction under a gradient of $1.486 \cdot 10^{-3}$ m/m. Thus, the south boundary of the aquifer was treated as a hydraulic gradient boundary that allowed water and solutes to flow out. The north boundary of the aquifer was treated as a Neumann boundary with a steady influx of water at a Darcy velocity of 0.24 m/day.

### 3.5.4 Source Terms

The source terms consisted of fluid and contaminant discharges to the series of trenches during trench operations. Estimated fluid volumes and inventory are defined by the median values predicted by the SIM model run for August 18, 2004. The time history of fluid discharges and inventory are summarized in Table 3.5. Fluid discharges are reported to have started in late 1956 and ended in early 1957 for most trenches, except for the 216-B-52 Trench, which was operational into 1958. A total of 37,044 $m^3$ (37 million liters) of fluids were applied during the operational period. On average, Trenches B-23 through B-28 received around 4752 $m^3$, while the much longer B-52 received 8529 $m^3$.

**Table 3.5. 2004 Composite Analysis 10,000-year (Median Inputs) Assessment of Fluid Influx ($m^3$)**

| Year | Fluid Influx by Trench ($m^3$) | | | | | | |
|---|---|---|---|---|---|---|---|
| | **B-52** | **B-23** | **B-24** | **B-25** | **B-26** | **B-27** | **B-28** |
| 1955 | 0.0 | 0.0 | 0.0 | 0.0 | 0.0 | 0.0 | 0.0 |
| 1956 | 4.4931 | 4519.9 | 4869.87 | 4909.9 | 3842.19 | 12.1091 | 13.8349 |
| 1957 | 1654.39 | 15.3636 | 17.3203 | 0.0 | 903.448 | 4407.77 | 5035.95 |
| 1958 | 6870.64 | 0.0 | 0.0 | 0.0 | 0.0 | 0.0 | 0.0 |
| 1959 | 0.0 | 0.0 | 0.0 | 0.0 | 0.0 | 0.0 | 0.0 |
| **Total** | 8529.523 | 4519.9 | 4869.87 | 4909.9 | 4745.638 | 4419.879 | 5049.785 |

To facilitate the evaluation of the impact fluids and contaminants originating from one trench on another, the fluids were injected into each individual trench. All fluid releases in the simulations originated at the base of the trench, and no ponding was allowed. The injection rate for input into STOMP was calculated by dividing the injection rate by the number of nodes covering the source area. The rate per unit linear length of trench was then divided by the number of nodes (n = 6) extending over the width of the trench bottom to generate the source strength for each node. The resulting nodal source strengths and duration of the source are summarized in Table 3.6 for each trench. Exact start dates and times are currently unknown, so start and end dates were set at the beginning and end of the reported months.

**Table 3.6. Summary of Nodal Fluid Source Strength and Duration**

| Trench | Length (m) | Start Date | End Date | Duration (day) | Vol ($m^3$) | Rate ($m^3$/day) | $R_{Node}$ ($m^3$/day) |
|---|---|---|---|---|---|---|---|
| 216-B-52 | 176.78 | 12/01/57 | 01/01/58 | 31 | 8529.523 | 275.1459 | 0.25941 |
| 216-B-23 | 152.40 | 10/01/56 | 10/31/56 | 30 | 4519.9 | 150.6633 | 0.16477 |
| 216-B-24 | 152.40 | 10/01/56 | 11/01/56 | 31 | 4869.87 | 157.0926 | 0.17180 |
| 216-B-25 | 152.40 | 11/01/56 | 12/01/56 | 30 | 4909.9 | 163.6633 | 0.17898 |
| 216-B-26 | 152.40 | 12/01/56 | 02/01/57 | 62 | 4745.638 | 76.5425 | 0.08371 |
| 216-B-27 | 152.40 | 02/01/57 | 04/01/57 | 59 | 4419.879 | 74.9132 | 0.08193 |
| 216-B-28 | 152.40 | 04/01/57 | 06/30/57 | 90 | 5049.785 | 56.1087 | 0.06136 |

All contaminant inventory was assumed to be dissolved in the discharged fluids; thus, the time history is identical to that of the fluid releases. The $^{99}Tc$ inventory generated by the SIMS model for the operation period totaled some 128.74 Ci while the total nitrate inventory was estimated at 6.7 million kg. For solute sources, STOMP requires specification in terms of a mass per unit time per source node. Thus, a procedure similar to that used for the fluid was used to calculate the solute density for the input file. The total inventory for each COC was first divided by the linear length of the trench to give a mass rate per unit length of trench. This rate was then divided by the number of nodes (n = 6) extending over the width of the trench bottom to generate the solute density for each node. The resulting node densities for $^{99}Tc$ and $NO_3^-$ as well as the duration of each injection are summarized for each trench in Table 3.7.

**Table 3.7. Summary of Nodal Solute Strength and Duration for Contaminant Inventories Based on the 2004 Composite Analysis 10,000-Year (Median Inputs) Assessment**

| Trench | Length (m) | Start Date | End Date | Duration (day) | $^{238}U$ (Ci) | $^{238}U$ Rate (Ci/day) | $^{99}Tc$ (Ci) | $^{99}Tc$ Rate (Ci/day) | $NO_3^-$ (kg) | $NO_3^-$ Rate (kg/day) |
|---|---|---|---|---|---|---|---|---|---|---|
| 216-B-52 | 176.78 | 12/01/57 | 01/01/58 | 31 | 0.0654 | 1.19E-05 | 25.504 | 4.65E-03 | 1.28E+06 | 2.34E+02 |
| 216-B-23 | 152.40 | 10/01/56 | 10/31/56 | 30 | 0.0371 | 8.10E-06 | 15.364 | 3.36E-03 | 8.02E+05 | 1.75E+02 |
| 216-B-24 | 152.40 | 10/01/56 | 11/01/56 | 31 | 0.0355 | 7.52E-06 | 18.109 | 3.83E-03 | 9.59E+05 | 2.03E+02 |
| 216-B-25 | 152.40 | 11/01/56 | 12/01/56 | 30 | 0.0359 | 7.85E-06 | 18.310 | 4.00E-03 | 9.67E+05 | 2.11E+02 |
| 216-B-26 | 152.40 | 12/01/56 | 02/01/57 | 62 | 0.0375 | 7.62E-07 | 17.510 | 1.86E-03 | 9.28E+05 | 9.82E+01 |
| 216-B-27 | 152.40 | 02/01/57 | 04/01/57 | 59 | 0.0323 | 3.59E-06 | 16.484 | 1.83E-03 | 8.71E+05 | 9.69E+01 |
| 216-B-28 | 152.40 | 04/01/57 | 06/30/57 | 90 | 0.0408 | 2.98E-06 | 7.3678 | 1.27E-03 | 9.16E+05 | 6.68E+01 |

## 3.6 STOMP Execution

Owing to the size of the 3-D computational domain (71 × 78 × 1317 =7,293,546 nodes), STOMP transient simulations of field-scale flow on this domain were conducted on the Environmental and Molecular Sciences Laboratory's (EMSL's) MPP2 super computer. Two-dimensional transient flow simulations were performed with STOMP77 on a Linux workstation while the 3-D simulations were performed on STOMP90 on EMSL's MPP2 computer. In both cases, the executable form of the code

was generated from the source code that is under version control by PNNL. Executing the simulator was a three-step process. First, the input file was used to generate a parameters definition file containing the information necessary for dimension arrays and to allocate memory. Next, the source code was compiled and linked using the previously generated parameters definition file and the appropriate libraries to generate the executable form of the code. Finally, the compiled code was executed with the input file corresponding to the case of interest.

Simulations with the 3-D domain were made using the parallel STOMP90 with the Portable Extensible Toolkit for Scientific Computation (PETSc) solver. The 2-D simulations were done with the serial STOMP77 using the library of iterative methods for sparse linear systems (SPLIB) (Bramley and Wang 1995) iterative linear system solver. The SPLIB solver is a collection of libraries that must be assembled on the executing computer and linked to the STOMP simulator during compilation. This solver, which is based on the conjugate gradient method, has a compact storage scheme for the Jacobian matrix and is preferable to the direct band solver for problems over 35,000 nodes. In the typical simulation, the STOMP simulator reads a series of input files and generates an output file, surface flux files, and a series of plot files.

## 3.7 Soil-Screening Process

Simulated concentrations of residual soil contaminants must be evaluated to determine if the contaminants will eventually migrate to the underlying aquifer. For such an analysis, the EPA recommends the use of soil-screening levels (SSLs). The EPA's final soil-screening guidance can be found in EPA (1996; 2000). The EPA's methodology relies upon using simplified contaminant fate-and-transport equations to determine a threshold value, the SSL, for a contaminant of concern in the soil. The SSLs are intended to correspond to levels of radionuclides in soil such that MCLs will not be exceeded in the underlying ground water beyond the edge of the waste area. Thus, if the SSL is not exceeded by the waste-site soil concentrations, then under the Comprehensive Environmental Response, Compensation and Liability Act of 1980 (CERCLA), there is no concern for remedial action.

The concept of the SSL is relatively easy to understand and apply. As contaminants move through the soil and beyond the water table entry point, they are subjected to physical, chemical, and biological processes. These processes include adsorption onto the porous medium, chemical transformation, biological degradation, and dilution due to mixing of the leachate with ground water. These processes typically reduce the concentration of contaminant concentrations at a receptor point such as a drinking water well down stream of the source. The reduction in concentration can be expressed through the dilution attenuation factor (DAF). The DAF is essentially the ratio of contaminant concentration in leachate out of the vadose zone to the concentration in ground water at the receptor point. The underlying assumptions in the screening process include 1) the conceptual site model is well developed, 2) site-specific data required by the model are available and meet data quality standards, and 3) the unsaturated zone model for radionuclide migration is properly applied.

The SSL methodology was designed for use during the early stages of a site evaluation when information about subsurface conditions may be limited and is therefore quite conservative. In addition, the following assumptions are made: 1) equilibrium between contaminants and soil/water is instantaneous, 2) the adsorption isotherm is linear with concentration, 3) volatilization is negligible, 4) contaminants are homogenous at the source, and 5) the receptor is located at a hypothetical well downstream of the waste

site, and (6) the system is isotropic. Because of this constraint, the methodology is based on simplifying assumptions about the release and transport of contaminants in the subsurface. Using SSLs based on simple models could lead to higher costs for additional site characterization or could lead investigators to use a more detailed and often more complex vadose zone transport model. Such detailed modeling may ultimately lead to a less restrictive, but still protective, SSL.

Both modeling approaches described above can be used to predict contaminant concentrations as a function of time (breakthrough curves) of the COCs entering the groundwater, the required input for the soil screening process. The predicted concentrations are then used to estimate groundwater concentrations at the receptor point of interest. The resulting receptor point concentrations are then compared with the acceptable maximum contaminant level (MCL) to determine if the soil concentrations at the site exceed the SSLs. Concentrations less than the acceptable groundwater concentrations suggest no need for concern for human health and ecology at the site.

### 3.7.1 Soil-Screening Levels

Two methods can be used to calculate the receptor point concentration using the leachate radionuclide concentrations to ground water provided by the unsaturated model. One method uses a dilution/attenuation factor (DAF) to account for the mixing of leachate with ambient ground water. In this study, we used both the simple convolution model and the more complex flow and transport model implemented in STOMP to calculate the SSLs. With the convolution model, the default value of 20 for DAF was used as proposed in the technical background document for SSLs (EPA 2000).

According to the EPA method, the basic equation used to calculate the SSL is a modified form of the Freundlich equation written as (EPA 2000)

$$SSL = C_{wt} \cdot DF \cdot CF \cdot (k_d + \theta / \rho_b) \tag{3.17}$$

where $SSL$ = soil screening level (pCi/g)
$C_w$ = groundwater concentration (pCi/L)
$DF$ = dilution attenuation factor ( )
$CF$ = conversion factor, (1 kg/1000g)
$k_d$ = soil water partition coefficient (kg/L)
$\theta$ = volumetric water content ($m^3$ $m^{-3}$)
$\rho_b$ = soil bulk density ($kg/m^3$)

A default value of 20 for DAF was proposed in the technical background document for SSLs for radionuclides. However, a site-specific estimate that can be used for the convolution model can be derived using the following equation:

$$DF = 1 + \left( \frac{K \cdot i \cdot d}{I \cdot L} \right) \tag{3.18}$$

where $DF$ = Dilution attenuation factor ( )
$K$ = Aquifer hydraulic conductivity (m/yr)
$i$ = Hydraulic gradient (m/m)
$I$ = Recharge rate (m/yr)
$d$ = Mixing zone depth (m)
$L$ = Source length parallel to groundwater flow (m)

The mixing zone depth depends on several variables and can be estimated as follows (EPA, 2000)

$$d = (2\alpha_v L)^{0.5} + d_a \left\{1 - \exp\left[(-L \cdot I)/(V_s \cdot n_e \cdot d_a)\right]\right\} \quad (3.19)$$

where $d$ = Mixing zone depth (m)
$L$ = Source length parallel to groundwater flow (m)
$\alpha_v$ = Vertical dispersivity (m)
$d_a$ = Aquifer depth (m)
$I$ = Recharge rate (m/yr)
$V_s$ Horizontal seepage velocity (m/yr)
$n_e$ = effective aquifer porosity ($L_{pore}/L_{aquifer}$)

The first term, in Equation (3.19) estimates the depth of mixing due to vertical dispersivity along the length of ground water travel. Defining the point of compliance with ground water standards at the down-gradient edge of the source, this travel distance becomes the length of the source parallel to flow $L$, assumed to be 100 m in this case. Aquifer parameters in Table 3.3 were used to estimate the site-specific dilution factors for use with the convolution model. The resulting dilution attenuation factors are summarized in Table 3.8.

**Table 3.8. Dilution Attenuation Factors for the for Various Distances to a Receptor Well at the BC Trench Site**

| Recharge Rate (mm/yr) | Dilution Attenuation Factor | | | |
|---|---|---|---|---|
| | L=1 m | L=10 m | L=100 m | L =1000 m |
| 25.0 | 4.96E+03 | 1.57E+03 | 5.00E+02 | 1.61E+02 |
| 3.5 | 3.54E+03 | 1.12E+04 | 3.54E+03 | 1.13E+03 |
| 0.5 | 2.48E+05 | 7.84E+04 | 2.48E+04 | 7.84E+03 |
| 0.1 | 1.24E+06 | 3.92E+05 | 1.24E+05 | 3.92E+04 |

Use of the STOMP simulator for SSL calculation requires more site-specific data and a greater modeling effort than using the simple site-specific SSL calculation. Because the model takes into account the complex site conditions and requires fewer assumptions than using the simple site-specific SSL calculation, it should provide more accurate SSL calculations. Inclusion of a confined aquifer at the base of the simulation domain allowed direct simulation of flow and transport in the saturated zone. Thus, the model was used to calculate the resulting concentration at the receptor taking into consideration the

processes of advection and dispersion in the ground water. In both methods, the receptor well is assumed to be located 100 m down gradient of the source.

### 3.7.2 Steady-State Convolution Solutions

Dimensional analysis of the 1-D steady-state convolution solution shows the units of the resident concentration, $C_R$, to be pCi per cubic meter of soil, pCi $m_b^{-3}$. The units of the flux concentration, $C_F$, were pCi per cubic meter of soil, pCi $m_b^{-3}$. To allow direct comparison with the measured $^{99}$Tc profile, simulated $C_R$ values were converted to pCi $g^{-1}$ of soil as follows:

$$C_R^*(z,t) = \frac{C_R(z,t)}{10^3 \cdot \rho_b} \tag{3.18}$$

where $\rho_b$ is the dry bulk density of the soil. In the analysis, the mean bulk density for the entire simulation domain is used. To convert the predicted $C_R$ to concentration per unit volume of pore water, the following relationship was used:

$$C_R^*(z,t) = \frac{C_R(z,t)}{10^3 \cdot \theta} \tag{3.19}$$

With this model, the required concentration is predicted directly by the simple convolution solution. Uncertainty in the SSL estimates due to uncertainty in the input parameters can be easily accommodated by incorporating probability density functions for the parameters into the solution.

### 3.7.3 STOMP Simulations

The STOMP simulator requires fewer assumptions than the simple site-specific SSL calculation based on the convolution solution. It also allows consideration of more complex fate-and-transport processes and site conditions and should result in more accurate SSLs, provided that the input data are sufficient and the model is properly applied. The STOMP simulator does not perform the required calculations directly. Calculation of the breakthrough curves of contaminant concentration at the water table from STOMP simulation results requires some additional processing. Average contaminant concentrations at the water table are calculated by scaling the solute mass flux at the water table with the corresponding water mass flux. Thus, average concentrations at the water table, $C_{wt}$ (pCi/L) were calculated from the STOMP surface flux files as

$$C_{wt} = \frac{\text{Solute Mass Flux at Water table (pCi/day)}}{\text{Water Mass Flux at Watertable (L/day)}} \tag{3.20}$$

# 4.0 Identification of Alternatives

CERCLA § 121(b)(1), 42 U.S.C. § 9621(b)(1), mandates that remedial actions must be protective of human health and the environment, cost-effective, and use permanent solutions and alternative treatment technologies and resource recovery alternatives to the maximum extent practicable. Section 121(b)(1) also establishes a preference for remedial actions that employ, as a principal element, treatment to permanently and significantly reduce the volume, toxicity, or mobility of the hazardous substances, pollutants, and contaminants at a site. CERCLA § 121(d), 42 U.S.C. § 9621(d), further specifies that a remedial action must attain a level or standard of control of the hazardous substances, pollutants, and contaminants, which at least attains applicable or relevant and appropriate requirements (ARARs) under federal and state laws, unless a waiver can be justified pursuant to CERCLA § 121(d)(4), 42 U.S.C. § 9621(d)(4). Remedial-action objectives are therefore specific goals to protect human health and the environment. These objectives are based on available information and standards, such as ARARs and risk-based levels established using the risk assessments.

A major remedial-action objective of relevance to the BC trench site is to maintain $^{99}$Tc levels in the groundwater at values below the groundwater ARARs. The ARARs for groundwater are 900 pCi/L for $^{99}$Tc and 10 mg/L for $NO_3^-$. There are a number of potentially suitable treatment technologies and process options for radiologically contaminated soils that could be applied to the BC trench site to minimize the long-term downstream transport of $^{99}$TC and $NO_3^-$. These general response actions include:

- no action
- monitored natural attenuation
- soil excavation
- offsite disposal
- soil washing
- *in situ* vitrification
- onsite containment and capping.

To support the FS, such general response actions must be screened for effectiveness, implementability, and relative cost. The scope of this study is to screen these alternatives to identify those that would minimize the long-term downstream transport of $^{99}$TC and $NO_3^-$ through the vadose zone. This limits the analysis to onsite containment and capping. For completeness, the no-action and monitored natural attenuation alternatives are included for comparison. In evaluating the possible cleanup alternatives, the goal is to determine the extent of chemical impacts on soil and groundwater; identify underlying soil and groundwater flow patterns, and select the most feasible cleanup alternative.

## 4.1 Detailed Analysis

The alternatives are analyzed individually against a set of evaluation criteria and then compared against one another to determine their respective strengths and weaknesses and to identify the key trade-offs that must be balanced for the site. The results of the detailed analysis are summarized so that an appropriate remedy consistent with CERCLA can be selected. The results of the detailed analysis are summarized so that the most effective capping strategy can be pursued.

### 4.1.1 No-Action Alternative

The no-action alternative provides an environmental baseline against which impacts of any proposed action and the alternatives can be compared. The no-action alternative, however, may have environmental impacts. In general, these would include any environmental impacts associated with not satisfying the underlying purpose and need for action. In the case of the BC cribs and trenches, the no-action alternative consists of refraining from the active application of any remediation technology to the BC trench site. At present, the trench surfaces are bare to sparsely vegetated with no infiltration controls. The no-action alternative also assumes no source-control removal action, no infiltration control, no revegetation, no administrative actions (including institutional controls), and no monitoring. A review of site conditions would be conducted at 5-year intervals, as required by CERCLA. The no-action alternative may or may not be a reasonable alternative. It is sometimes coupled with monitored natural attenuation, which relies on natural processes to attenuate contaminants in soil and groundwater. Natural attenuation may occur at most polluted sites. However, the right conditions must exist in the subsurface for this alternative to have significant impact on contaminant concentrations. Natural attenuation processes may include biodegradation, biotransformation, diffusion, dilution, adsorption, volatilization, chemical reaction or destruction, downstream transport, evaporation, and plant uptake. Long-term monitoring (monitored natural attenuation [MNA]) could be conducted to confirm that contaminant reduction is occurring and that the reduction is achieving remedial action objectives. One simulation, Case 1, was performed to evaluate the no-action alternative (Table 4.1).

### 4.1.2 Capping Alternative

This alternative includes remediation by capping without removing any of the contaminated sediments. Capping involves placement of an engineered cap consisting of fine-textured high-storage capacity material on top of the contaminated site after placement of a layer of fill. The fine-textured material minimizes recharge by storing precipitation until it can be recycled to the atmosphere by plants. This alternative would also rely on naturally occurring attenuation processes to reduce the toxicity, mobility, and mass of the contaminants in the subsurface. A review of site conditions would be conducted at 5-year intervals, as required by CERCLA. It is expected that the area would be remediated as a single unit. However, the total area to be remediated would depend on the results of the model analysis and the geophysical investigations. At the time of this analysis, capping alternatives had not been identified. Consequently, no specific candidate designs are considered. Modeling was conducted to evaluate the impact of infiltration control on the target levels for groundwater over a 10,000-yr period. Table 4.1 summarizes the assumptions about recharge.

### 4.1.3 Summary of Simulation Cases

Table 4.1 summarizes the simulation cases. In all cases, the pre-Hanford (year 0 to 1945) recharge rate and the rate up to trench construction is assumed to be 3.5 mm $yr^{-1}$. During the trench operations and up to the point of stabilization (1956–1982), a mean recharge rate of 77 mm $yr^{-1}$ is assumed. For stabilization, it is reported that “top soil” was added to the surface. Although very little is known about the top soil, it is assumed to be sandy material with some water-holding capacity that eventually developed some sparse vegetation. Thus, a recharge rate of 25 mm $yr^{-1}$ is assumed to exist through the end of simulation. For Case-1, no remedial action is considered beyond the stabilization done in 1982. Thus after stabilization, a recharge rate of 25 mm $yr^{-1}$ is assumed for the duration of the 10,000-yr simulation.

**Table 4.1. Summary of Simulation Cases for Evaluation of Alternatives**

| Case | Description | Start Date | End Date | Recharge Rate (mm/yr) | | | |
|---|---|---|---|---|---|---|---|
| | | | | Pre-op | Operation | Post-Op | Remedial |
| 1 | No Action | 2012 | 10012 | 3.5 | 77.0 | 25.0 | 25.0 |
| 2 | No Action | 2012 | 10012 | 3.5 | 77.0 | 25.0 | 3.5 |
| 3 | Cap A | 2012 | 10012 | 3.5 | 77.0 | 25.0 | 0.5 |
| 4 | Cap B | 2012 | 10012 | 3.5 | 77.0 | 25.0 | 0.1 |
| 5 | Cap C | 2012 | 10012 | 3.5 | 77.0 | 25.0 | 0.0 |

Case 2 also considers a no-action alternative but with a recharge rate of 3.5 mm $yr^{-1}$. These two rates are intended to reflect the uncertainty in recharge at the site and demonstrate the possible effects on transport.

Cases 3 through 5 consider the onsite capping alternatives. In all cases, a surface barrier is assumed to be constructed in 2012. As in the no-action alternative, the recharge rate before operations is assumed to be 3.5 mm $yr^{-1}$. During the time the trench was in operation, a mean recharge rate of 77 mm $yr^{-1}$ is assumed and remains constant through 1982 when the trenches were stabilized. Following stabilization, the recharge rate was reduced to 25 mm $yr^{-1}$ and remains fixed until 2012. In 2012, it is assumed that a surface cover of infinite dimensions is constructed over the surface. The assumption of an infinite cover is made to avoid choosing any one design over the other from the several candidate designs being considered for Hanford and to avoid issues related to side-slope recharge. It has been shown that recharge from current side-slope designs can be a significant portion of precipitation; however, there is no standard design or practice (Ward et al. 2004). Owing to the absence of any rigorous scientific basis for long-term changes in barrier performance due to degradation, degradation is ignored, and it is assumed that cover performance remains unchanged for the duration of the simulation.

The difference between the five cases results from differences in the drainage criterion for the covers, which are assumed to be of different degrees of robustness. Cap A is the least robust of the covers and is assumed to restrict recharge to 1.0 mm $yr^{-1}$ for the duration of the simulation. Cap B is assumed to limit recharge to 0.5 mm $yr^{-1}$, the same as the prototype Hanford barrier. Cap C is the most robust of the three with a drainage criterion of 0.0 mm $yr^{-1}$. It should be noted that Cap C was not simulated with the 1-D convolution model.

For each remedial alternative, model simulations were performed to determine the extent of chemical impacts on soil and groundwater; to identify underlying soil and groundwater flow patterns, and to select the most feasible alternative. Simulations were executed for a periods of compliance ranging from 500 years to 10,000 years. Initial flow conditions for the first stages of the simulation were established with a steady-state flow simulation that assumed a natural infiltration rate of 3.5 mm $yr^{-1}$.

# 5.0 Evaluation of Alternatives

This section discusses the key findings from the fate-and-transport behavior analysis and presents contaminant breakthrough curves, soil screening levels, and mass balances at the entrance to the water table. Steady-state predictions based on the 1-D analytical convolution solution and 2-D simulations with STOMP were used to determine fluid flow and solute transport behavior to the water table for a cross section through Trenches B-28 through B-52. Resulting concentrations and fluxes were used to calculate soil screening levels for $^{99}Tc$ and $NO_3^-$ associated with the migrating plume. The results of these simulations were then used to evaluate remedial alternatives consisting of a no-action alternative and a capping alternative.

## 5.1 Steady-State Transport Simulation Results

The steady-state convolution solutions considered either 1) a depth invariant, $\theta(z)$, represented by a mean water content 0.08294 $m^3\ m^{-3}$, or 2) a depth-dependent water content, $\theta(z)$, derived from the neutron-log measurements. Two approaches were used to compare the observed data to the model predictions. In the first approach, the plume was treated as a single entity, and the mean recharge rate was estimated from the location of the center of mass and the travel time to the center of mass of the complete plume. In the second approach, the plume was decomposed into leading and trailing components, and the analysis was repeated for the two components. The results for the depth invariant water content are summarized below.

### 5.1.1 Fitting the Observed Data

The field data from the C4191 borehole were fitted to the analytical solution to estimate the mean pore-water velocity, from which the recharge rate can be inferred when the mean water content is known as well as the dispersivity. Figure 5.1a shows the result when only the longitudinal dispersion coefficient, *D*, and the pore-water velocity were fitted to the data. When only *D* and *v* were fitted, the results were far from satisfactory. The measured water content was used to calculate *v* and estimate the mean recharge rate. The calculated *v* allows the center of mass to be matched quite well. Based on the 1-D analysis, the center of mass is located at 33.462 m, compared to 33.778 m derived from spatial moment analysis. In contrast, the fitted dispersion (1.058 $m^2\ yr^{-1}$) appears too large. The fitted profile shows a much larger concentration between the surface and the peak and between the peak and the leading edge of the plume.

A number of features of the transport problem cannot be captured with a 1-D model. Indeed, the problem is 3-D, and successful application of a 1-D model would require assumptions about the effective area over which spreading occurs to match the mean velocity, the effective dispersion coefficient, and the peak concentrations. Better simulations were obtained on fitting three parameters by assuming 1-D advection and 2-D dispersion (Figure 5.1b). By allowing the plume to spread in a second dimension, the center of mass is now located at 32.88 m. In addition, the longitudinal dispersion coefficient decreases significantly to 0.468 $m^2\ yr^{-1}$, and a transverse dispersion coefficient of 0.019 $m^2\ yr^{-1}$ results. The discrepancy between the predicted and observed peak concentrations also decreased.

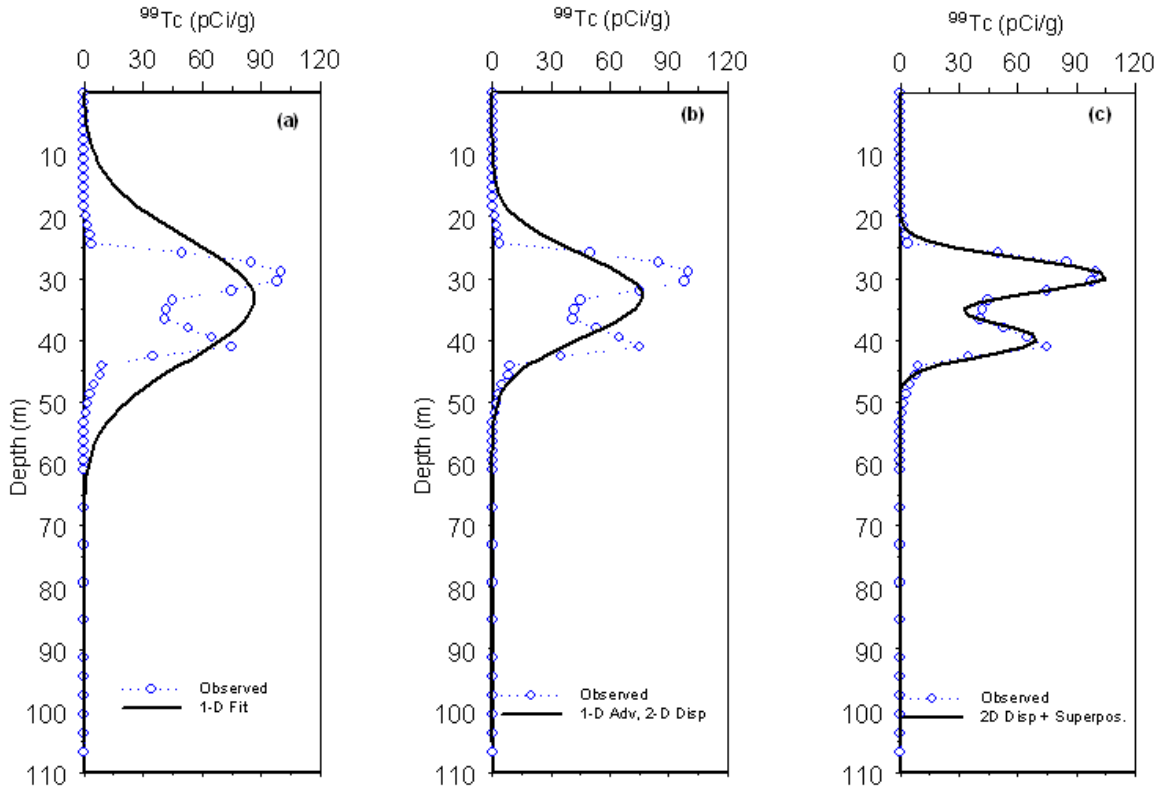


**Figure 5.1. Measured and Fitted Resident Concentrations of $^{99}$Tc, (a) 1-D advection, 1-D Dispersion, (b) 1-D Advection, 2-D Dispersion, and (c) 1-D Advection, 2-D Dispersion with Superposition**

Given the bimodal nature of the $^{99}$Tc plume, it became clear that physical heterogeneity played an important role in the transport process. The region of low $^{99}$Tc concentration between the two peaks observed in the field data necessitated a two-zone application of the model. The final solution represents a superposition of the individual solutions for a fast and slow zone. Although this is perhaps an oversimplification of the physics of flow, at both depths, the predicted concentration and the amount of spreading are reasonably close to the observed. The fitted velocities correspond to mean travel depths of 39.837 m for the leading edge and 29.694 m for the trailing edge. The results compare well with 39.674 m and 29.838 m, calculated by moment analysis for the leading and trailing edges, respectively.

Despite the reasonably good fits of the data to the analytical steady-state models, it is important to note the limitations of this approach, especially for predictive purposes. With only the information on inventory and trench dimensions, it would be virtually impossible to predict the subsurface distribution without *a priori* information on the contaminant distribution *and* the small-scale stratigraphy that controls spreading. In fact, application of the simple models with accepted recharge estimates and mean soil water content while ignoring the spreading effect would result in the plume reaching the water table in a short period of time after trench closure. While STOMP and other mechanistic models are based on independently derived parameters, the simple models presented here are only fitted to the data and in no way render validity to the model, especially for predictive purposes. Using steady 1-D models to predict flow in more complex natural transient flow situations will require independent means for estimating the

effective area over which transport occurs. Such information, which provides insight into the physical heterogeneity and the relationships between recharge rate and flow anisotropy, can only come for subsurface characterization or field experiments at representative sites.

### 5.1.2 Soil-Screening Levels Following Remediation

Although the simple 1-D models are of limited use for predicting surface transport in the presence of physical heterogeneity, the convolution models are of greater utility for predicting the potential migration of contaminants initially present in the soil. Here the convolution solutions are applied to the $^{99}$Tc initially present in the soil to predict soil $^{99}$Tc concentrations following the various remedies and ultimately the travel time to the groundwater table at 103 m.

Figure 5.2 through Figure 5.5 show comparisons of measured $^{99}$Tc concentrations in the soil profile at sampling with the predicted concentrations following application of different remedial actions. The no-action alternative is shown in Figure 5.2. The surface is assumed to be sparsely vegetated with a water flux of 25 mm yr$^{-1}$ exiting the root zone. The rate of 25 mm yr$^{-1}$ is consistent with that of a sparsely vegetated coarse-textured surface observed at the prototype Hanford barrier. If the surface remained bare to sparsely vegetated, the peak concentration in the soil would decrease by about 30 percent in as little 10 years. In 100 years, the plume would impact the groundwater and by the year 3005, the entire plume would have entered the groundwater. A water flux of 3.5 mm yr$^{-1}$ is equivalent to the recharge rate from an established shrub steppe ecosystem and therefore assumes a healthy stand of shrubs and grasses on the trench surfaces. At 3.5 mm yr$^{-1}$, there is significant distribution about the center of mass after 100 years, although there is significant redistribution about the center of mass (Figure 5.3). By the year 3005, the plume would have entered the groundwater.

The impact of the recharge rate resulting from the different remedial actions is manifested primarily through its effect on the pore-water velocity, which controls the advective movement of the plume, and secondarily through its effect on the dispersion coefficient, which also varies with pore-water velocity. Here, the average water content, derived from the corrected neutron probe measurements, was 0.08 m$^3$ m$^{-3}$. The pore-water velocity, $v$, was calculated from the recharge rate as $q/\theta$ to give velocities ranging from 10.375 mm yr$^{-1}$ to 1.25 mm yr$^{-1}$. Because of the long half life of $^{99}$Tc and its zero $K_d$, the only mechanism by which the concentration is reduced is by hydrodynamic dispersion. With a 1-D model, a reduction in the soil concentration to the SSL can only come about through movement of the plume into the water table.

As can be expected, as the mean recharge rate decreases, the pore-water velocity decreases the rate of advance of the plume. An assumption of the same water content at all depths is not very realistic, especially in soils that are highly stratified. Simulations with the 1-D model in which measured water content variations with depth taken into consideration resulted in somewhat lower soil concentrations at equivalent times. However, the lower concentrations result from higher velocities that occur when $\theta(z)$ is allowed to vary. This result is consistent with the findings of Schoen et al. (1999) who found that accurate predictions of $Br^-$ transport in a large lysimeter using 1-D analytical solutions required taking into account the highly stratified characteristics of the soil. Nevertheless, in all cases except the no-action alternative at 25 mm yr$^{-1}$, the soil screening levels would exceed the current standards for $^{99}$Tc even after 1000 years.

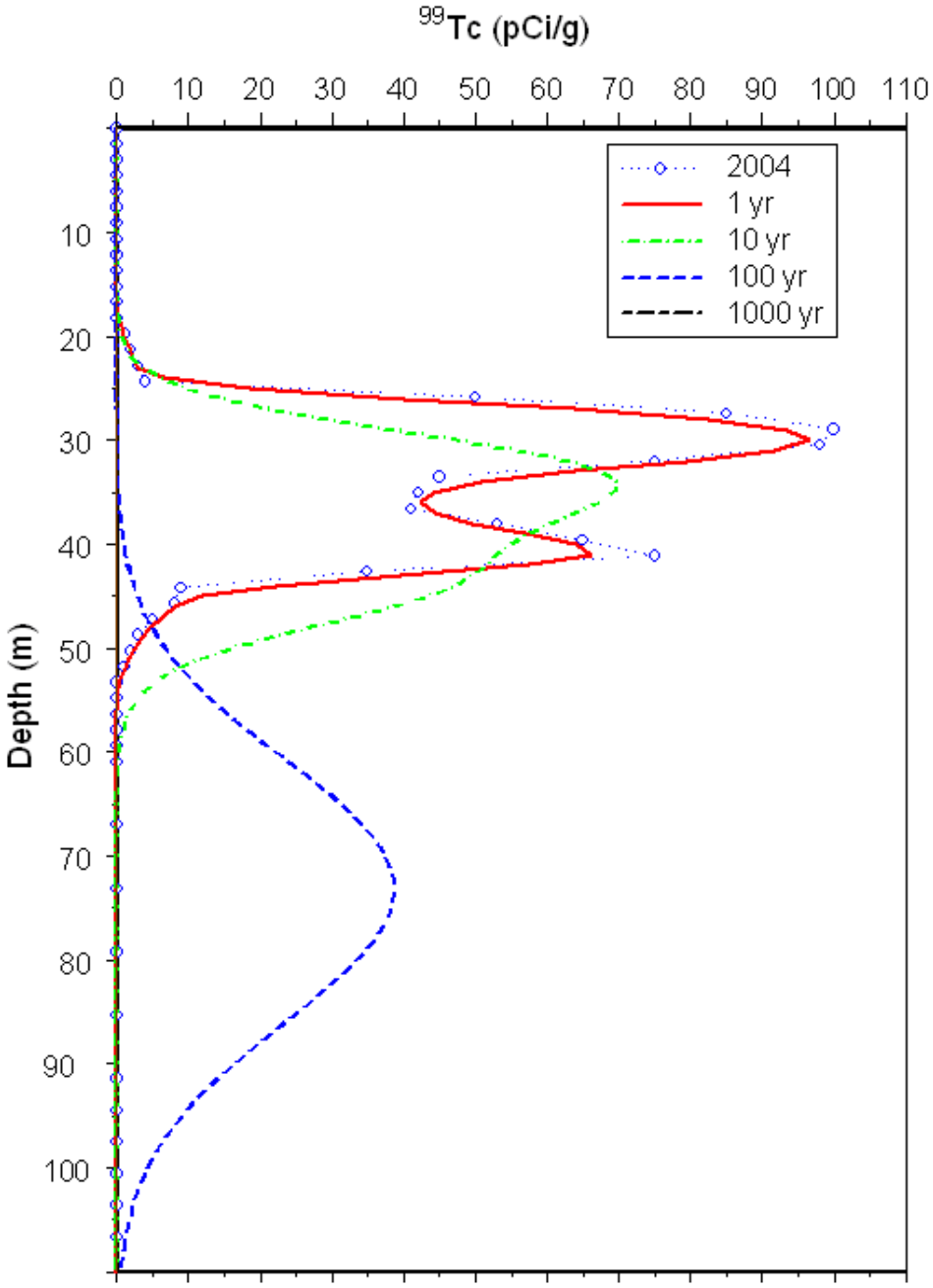


**Figure 5.2. A Comparison of Measured and Predicted $^{99}$Tc Concentrations Based on a 1-D Convolution Solution to the Convection-Dispersion Equation. The assumed recharge rate is 25 mm yr$^{-1}$ under the no-action alternative.**

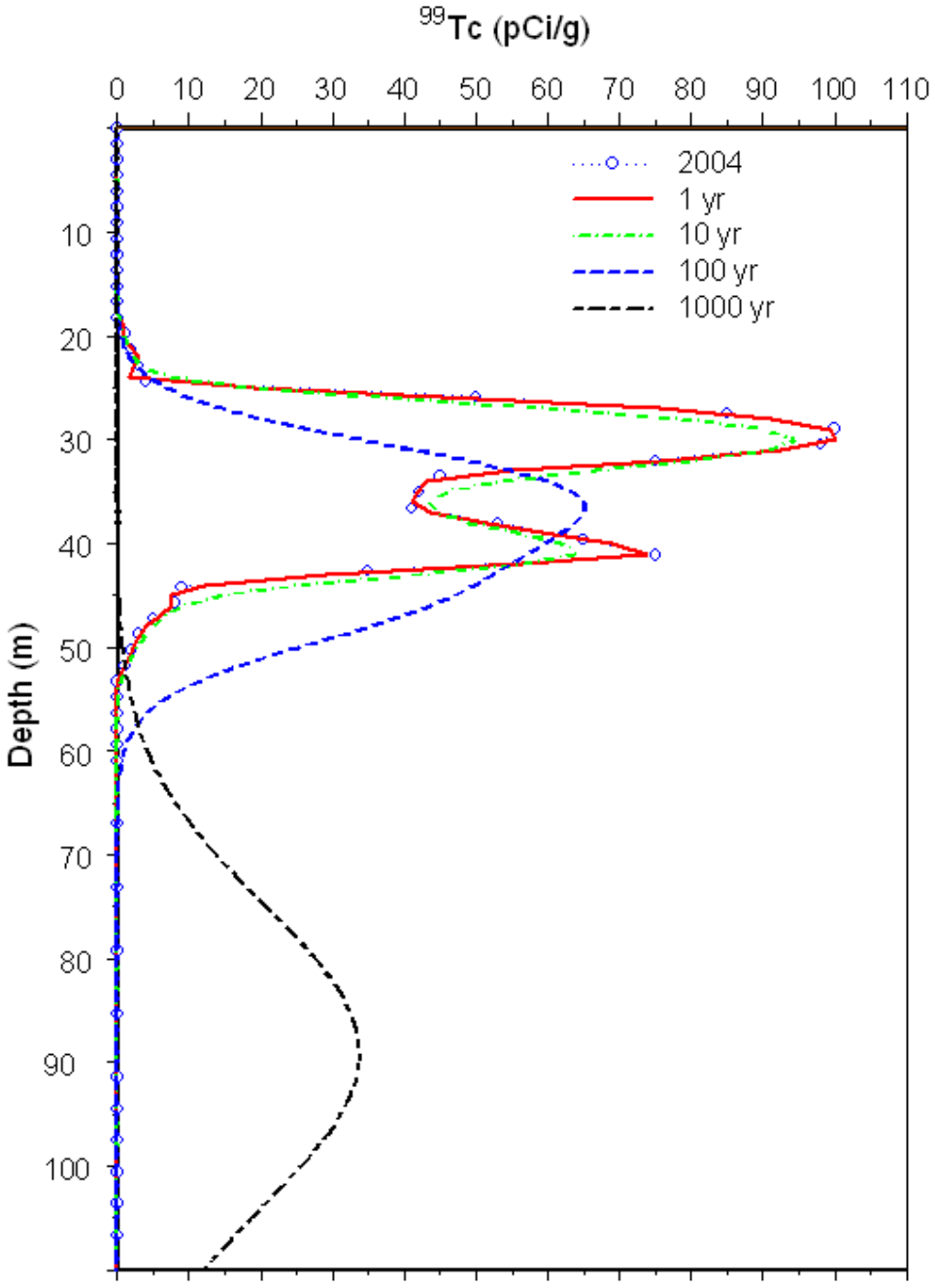


**Figure 5.3. A Comparison of Measured and Predicted $^{99}$Tc Concentrations Based on a 1-D Convolution Solution to the Convection-Dispersion Equation. The assumed recharge rate is 3.5 mm yr$^{-1}$ under the no-action alternative.**

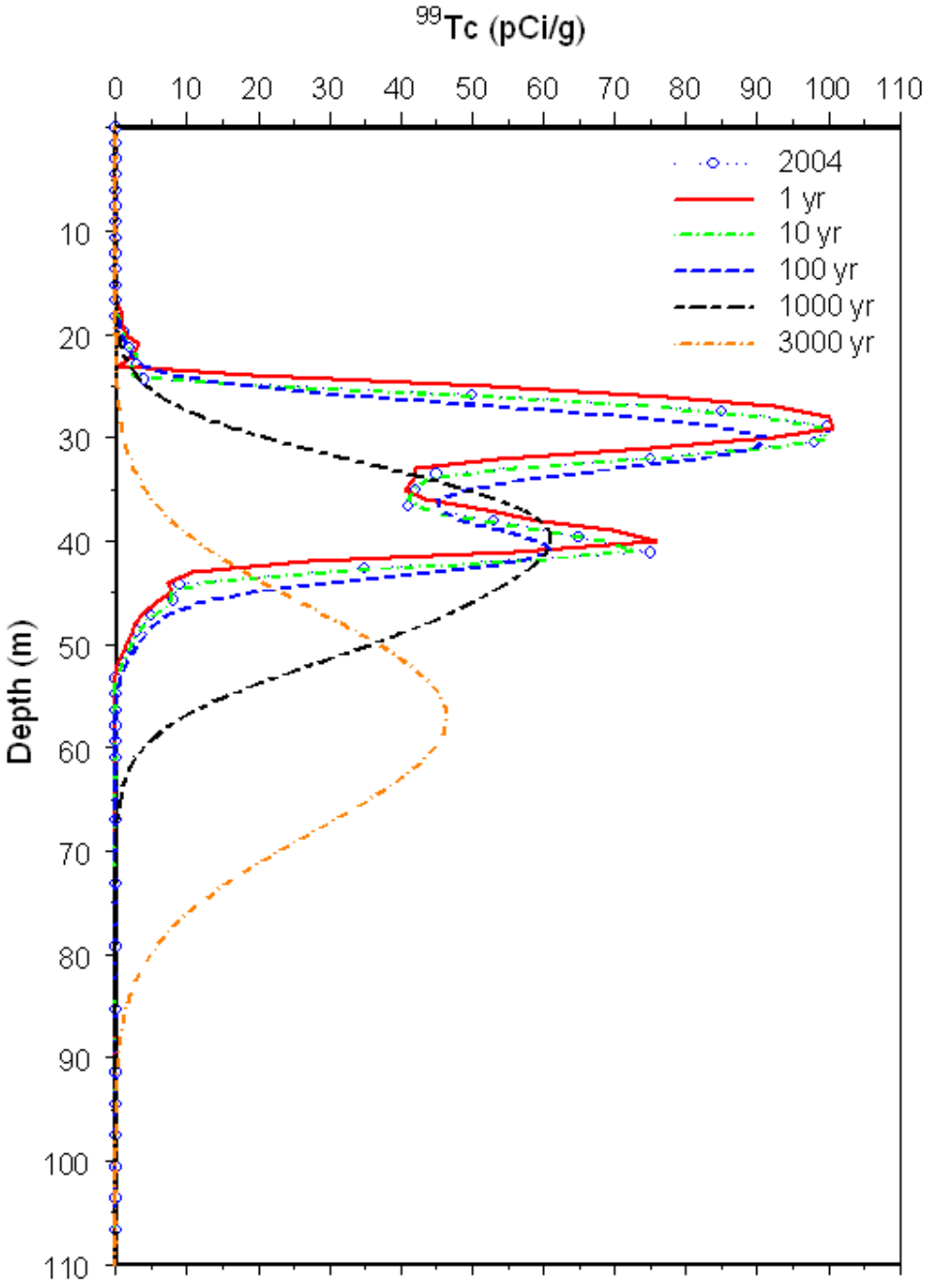


**Figure 5.4. A Comparison of Measured and Predicted $^{99}$Tc Concentrations Based on a 1-D Convolution Solution to the Convection-Dispersion Equation. The assumed recharge rate is 0.5 mm yr$^{-1}$ under capping alternative.**

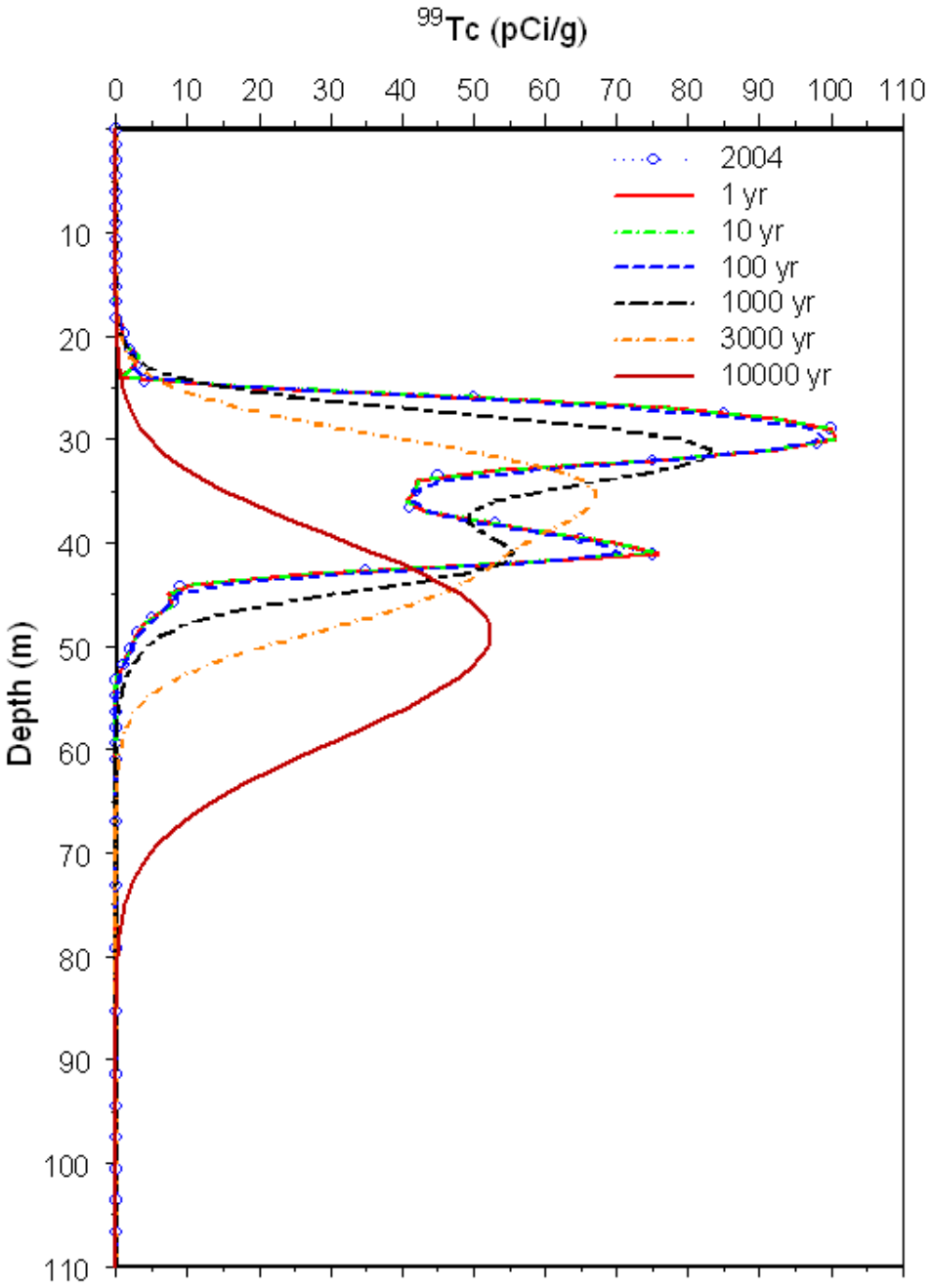


**Figure 5.5. A Comparison of Measured and Predicted $^{99}$Tc Concentrations Based on a 1-D Convolution Solution to the Convection-Dispersion Equation. The assumed recharge rate is 0.1 mm yr$^{-1}$ under the capping alternative.**

Soil screening levels were calculated for $^{99}Tc$ and $NO_3^-$ for each alternative for assuming the distances from the hypothetical receptor well. The results are summarized in and the results are summarized in Table 5.1. The results for NO3- are summarized in Table 5.2. In general, as the recharge rate decreased, the dilution attenuation factor increased and the soil screening levels for each contaminant increased. Based on inventory recovered from beneath 216-B-26 and assuming a receptor 100 m down-gradient from the trench site, current soil concentrations of $^{99}Tc$ exceed screening levels for the no-action alternatives. However, current concentrations and predicted concentrations under the capping alternative all fall below the calculated screening levels.

**Table 5.1. Soil Screening Levels for $^{99}Tc$ as a Function of Recharge Rate and Distance, L, to a Receptor Well**

| Recharge Rate (mm/yr) | Soil Screening Level (pCi/g) | | | |
|---|---|---|---|---|
| | L=1 m | L=10 m | L=100 m | L =1000 m |
| 25.0 | 4.50E+00 | 1.37E+01 | 4.29E+01 | 1.35E+02 |
| 3.5 | 3.07E+01 | 9.68E+01 | 3.05E+02 | 9.62E+02 |
| 0.5 | 2.14E+02 | 6.73E+02 | 2.13E+03 | 6.73E+03 |
| 0.1 | 1.07E+03 | 3.37E+03 | 1.07E+04 | 3.32E+04 |

**Table 5.2. Soil Screening Levels for $NO_3^-$ as a Function of Recharge Rate**

| Recharge Rate (mm/yr) | Soil Screening Level (mg/g) | | | |
|---|---|---|---|---|
| | L=1 m | L=10 m | L=100 m | L =1000 m |
| 25.0 | 5.00E-02 | 1.52E-01 | 4.76E-01 | 1.50E+00 |
| 3.5 | 3.41E-01 | 1.07E+00 | 3.39E+00 | 1.07E+01 |
| 0.5 | 2.37E+00 | 7.48E+01 | 2.37E+01 | 7.48E+01 |
| 0.1 | 1.19E+01 | 3.74E+01 | 1.12E+03 | 3.69E+02 |

### 5.1.3 Peak Concentrations and Arrival Times at the Water Table

Figure 5.6 through Figure 5.9 show the temporal variations in $^{99}Tc$ at the water table predicted by the 1-D convolution model. To capture the wide range in concentrations, $^{99}Tc$ is plotted on a logarithmic scale. The 900 pCi/L MCL is included on each graph for a reference. The peak concentrations and the corresponding arrival times at the water table are presented in Table 5.3. Because the model simply propagates the existing inventory downward, the resulting concentrations reaching the water table are based on the assumption that the initial contaminant distribution observed at C4191 is applicable to the entire site. As the plume moves downward, the model predicts increasing symmetry in the shape of the curve as the bimodal feature caused by statigraphy is lost. Although the model can account for vertical changes in water content, water can only move in one direction, and the net effect is a smoothing of the breakthrough curve.

The recharge rate is clearly the dominant factor in the 1-D model affecting the arrival time of the MCL, the arrival time of the peak, and the peak concentration. First, a reduction in recharge rate reduces the effective velocity as well as the peak concentration entering the water table. In should be noted that the 1-D convolution model assumes an average recharge rate and does not take into account episodic high-intensity events that could have a greater short-term impact. As recharge rate decreased, the arrival time of the MCL (900 pCi/L), the peak arrival time, and the arrival time of the center of mass increased (Table 5.3). The time to arrival of the MCL decreased from the year 2083, only 78 years from the present, under an assumed no-action recharge rate of 25 mm $yr^{-1}$, to the year 7792 when a barrier limiting the recharge to 0.5 mm $yr^{-1}$ was assumed. A more robust barrier that limits recharge to 0.1 mm $yr^{-1}$ pushed the arrival time of the MCL to the year 39,686.

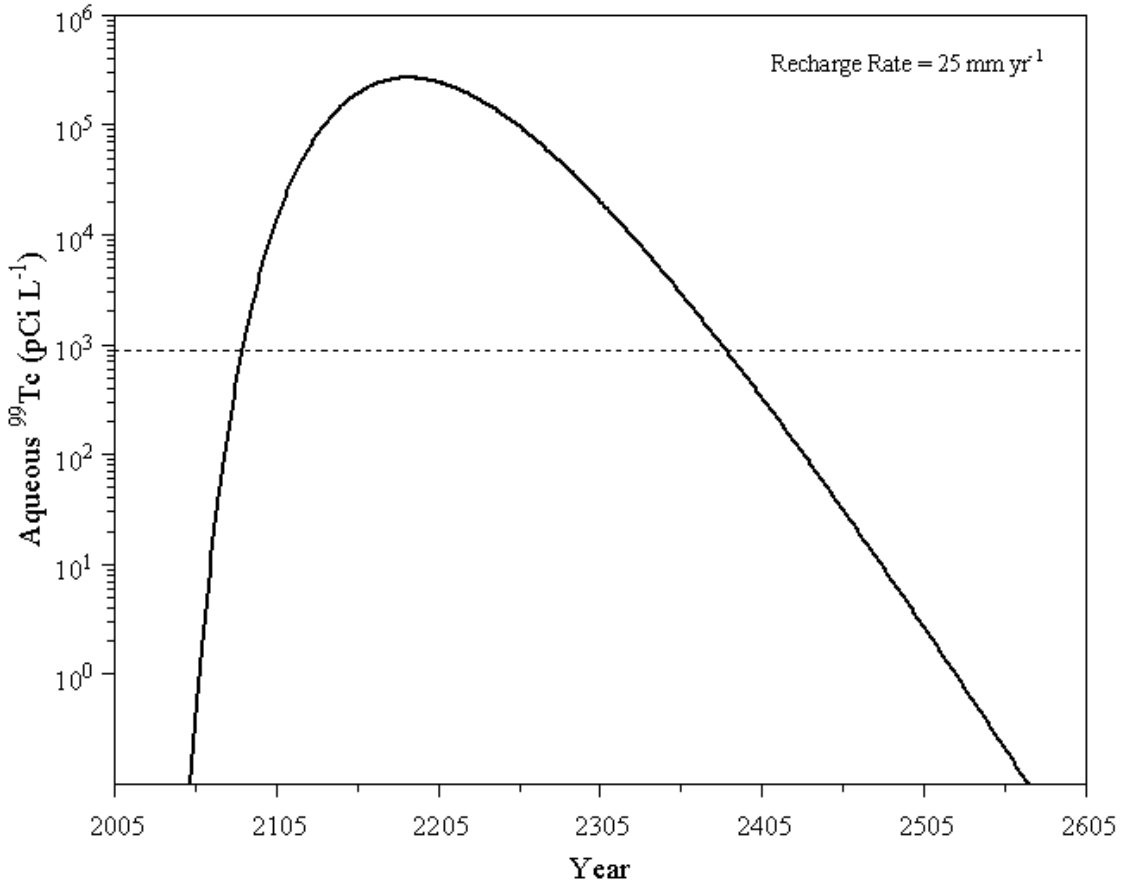


**Figure 5.6. Calculated Distributions for $^{99}Tc$ at the Water Table Under a Recharge Rate of 25 mm/yr Using the 1-D Convolution Solution**

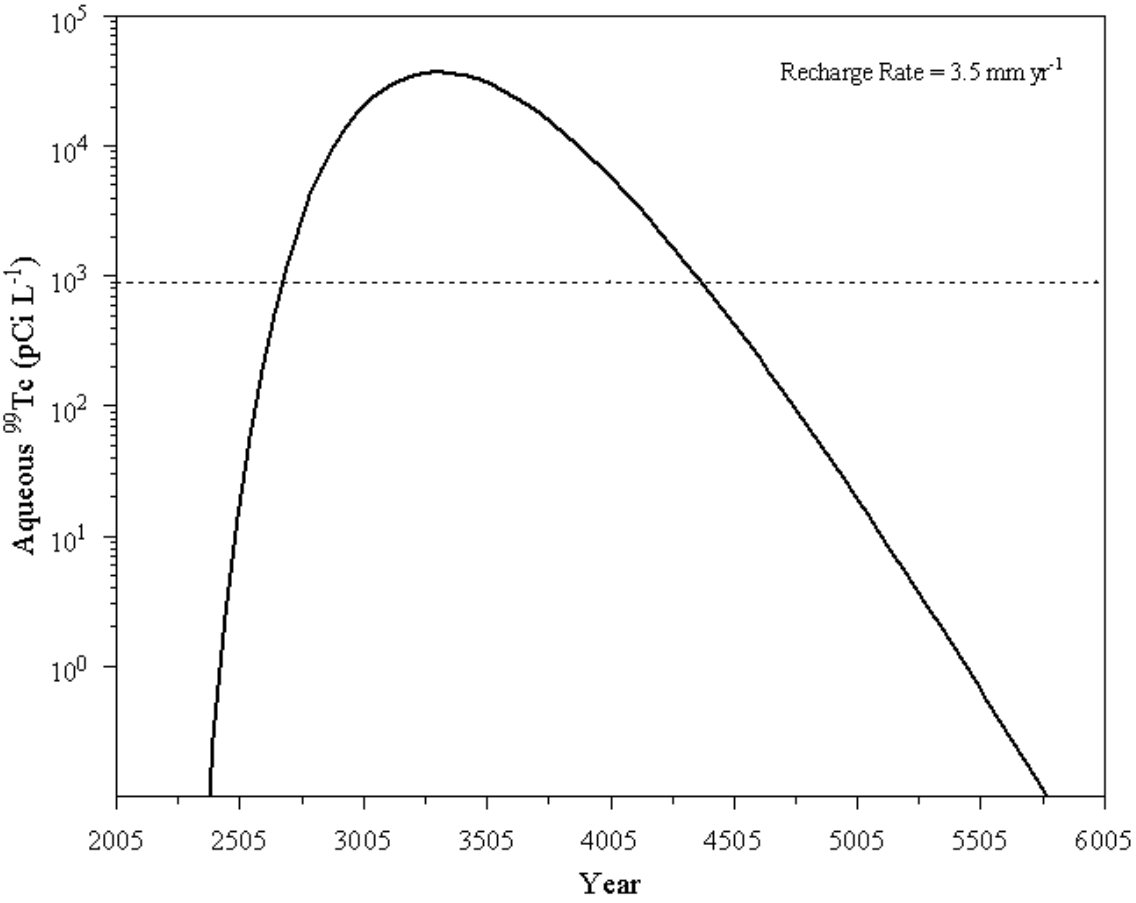


**Figure 5.7. Calculated Distributions for $^{99}$Tc at the Water Table Under a Recharge Rate of 3.5 mm/yr Using the 1-D Convolution Solution**

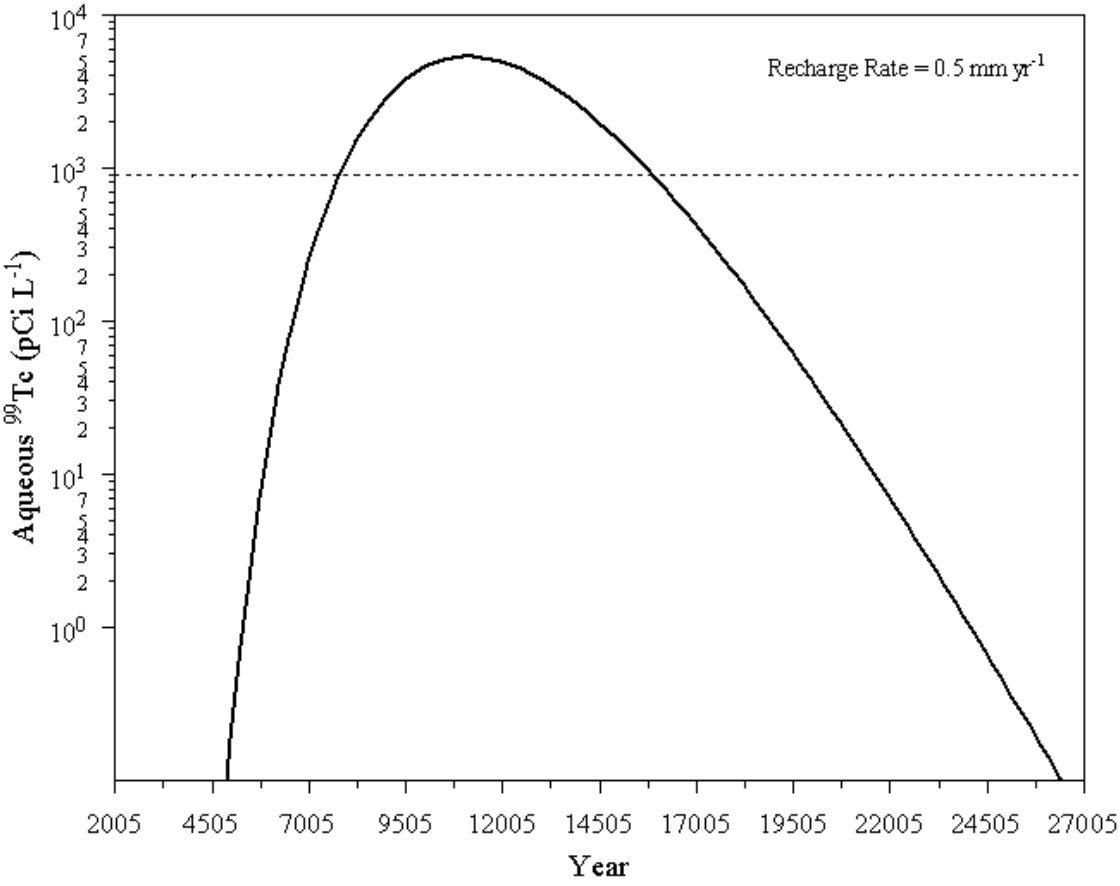


**Figure 5.8. Calculated Distributions for $^{99}$Tc at the Water Table Under a Recharge Rate of 0.5 mm/yr Using the 1-D Convolution Solution**

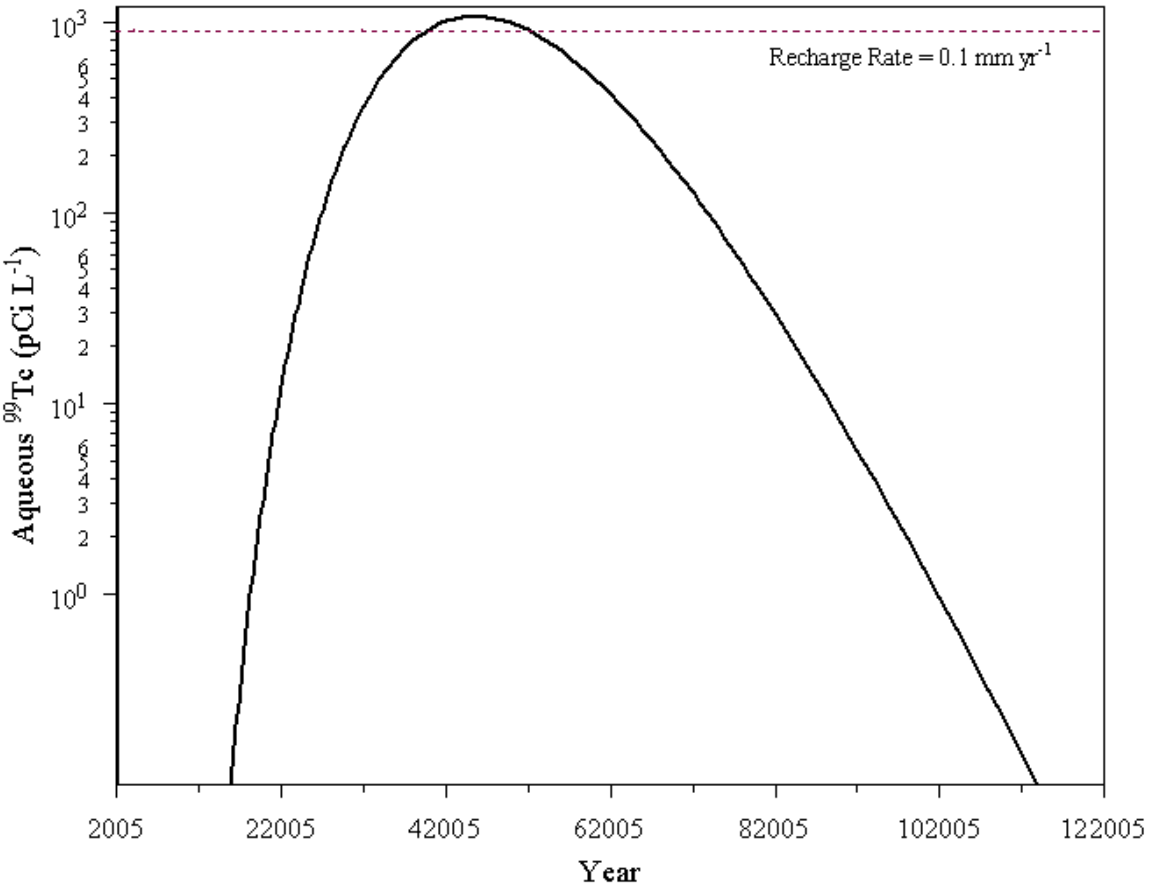


**Figure 5.9. Calculated Distributions for $^{99}$Tc at the Water Table Under a Recharge Rate of 0.1 mm/yr Using the 1-D Convolution Solution**

**Table 5.3. Predicted Peak $^{99}$Tc Concentrations (pCi/L) and Arrival Times at the Groundwater Table Beneath the BC-Trenches Based on a 1-D Convolution Solution**

| Recharge Rate (mm/yr) | MCL Arrival Time (yr) | Peak Arrival Time (yr) | Peak Concentration (pCi/L) | Mean Arrival Time (yr) | Arrival Time Variance ($yr^2$) |
|---|---|---|---|---|---|
| 25.0 | 2083.93 | 2133 | 3.740E+05 | 2142.85 | 1.008E+03 |
| 3.5 | 2218.56 | 3328 | 3.729E+04 | 3392.55 | 1.00E+05 |
| 0.5 | 7791.90 | 11218 | 5.336E+03 | 11723.58 | 4.93E+06 |
| 0.1 | 39686.45 | 45000 | 1.067E+03 | 48589.67 | 1.28E+08 |

The 1-D convolution model is easy to apply and can easily accommodate initial contaminant inventory depth distributions of any complexity (Elrick et al. 1997). The model can also handle depth-dependent water-content profiles. However, the results are somewhat conservative in that the model does not take credit for stratification and its dimensionality effects. Nevertheless, these relatively simple equations based on the assumption of steady-state flow as an approximation to the more complex transient flow problem typical of natural environments may be useful to provide quick estimates of soil screening levels and groundwater concentrations. The concentrations reaching the water table can be used to predict

concentrations at a receptor well using the dilution attenuation factors derived above or by using the results as input to an analytical ground water transport model. Although the concentrations arriving at the water table exceed the MCL, concentrations reaching a hypothetical receptor well down-gradient of the trench site would be significantly less that the MCLs.

## 5.2 Transient Transport Simulation Results

The dispersion of contaminants in the vadose zone and groundwater is an inherently 3-D process. At the field scale, even low-order transverse dispersion acting over a long distance can substantially affect the configuration of a contaminant plume (Domenico and Robbins 1984; Burnett and Frind 1987). Burnett and Frind (1987) found that in vertical-plane simulations, the dimensionality effect became noticeable at a transverse dispersivity of only 1 cm and could result in significant overestimation of a plume length. Only transient multidimensional simulations are capable of producing the actual concentration values that drive local processes, including chemical reactions. In the sections that follow, results of the transient simulations performed with the STOMP simulator are presented. A summary description and comparison of results follows the individual case descriptions summarized in Table 4.1.

In the transient simulation problem, the characteristics of saturation field are controlled by lithostratigraphy, hydraulic properties, and the presence of subsurface features, e.g., sloped or pinched layers that can focus or redirect flow. Natural precipitation and its temporal distribution may also play an important role as short-term fluctuations can cause localized extreme saturation changes. Such effects are not evident in this analysis as the stratigraphic model is of the layer-cake type and a mean recharge rate is used for the simulations.

### 5.2.1 Initial Conditions and Saturation Distributions

In the first phase of the transient simulations, the model was run from time zero to the year 1956 with a recharge rate of 3.5 mm $yr^{-1}$. This was necessary to establish pre-Hanford conditions to initialize the model. Since the exact time at which the trenches were excavated is unknown, the recharge rate from 1945 to 1956 is assumed to remain unchanged at 3.5 mm $yr^{-1}$. Figure 5.10 shows the predicted volumetric water content in 1956, just before trench operations. Because this stratigraphic model is

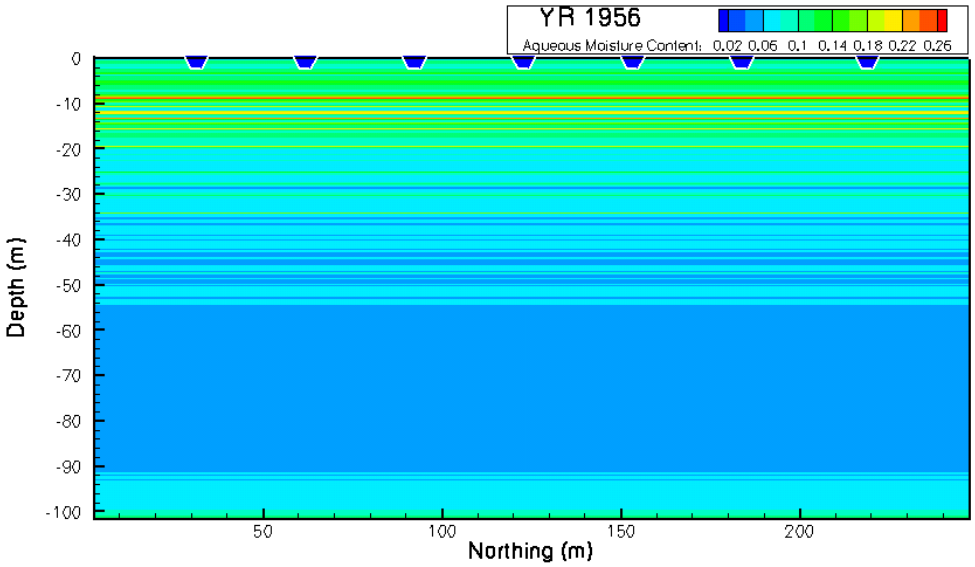


**Figure 5.10. Calculated Distributions of Soil Volumetric Water, $\theta(x,z)$ in 1956, Before Trench Installation and Operation, Assuming Perfect Stratification**

based on a single borehole (C4191), the model is perfectly stratified and therefore shows none of the horizontal discontinuities observed in Figure 2.2. Simulations with this stratigraphic model resulted in spatially continuous capillary breaks. When simulated with anisotropy, this model resulted in extensive lateral flow, likely because the capillary breaks extended to the boundaries and a constant recharge rate did not lead to water potentials that could overcome the entry pressure of the underlying coarse layers.

Figure 5.11 shows the predicted aqueous saturation in 1956 based on the **SGSIM** derived stratigraphic model. This stratigraphic model takes into account the spatial correlation structure of soil moisture and therefore the heterogeneity. The saturated zone at the base of the domain represents the 5-m thick confined aquifer. All subsequent simulations were based on the stratigraphic model derived from the **SGSIM** results.

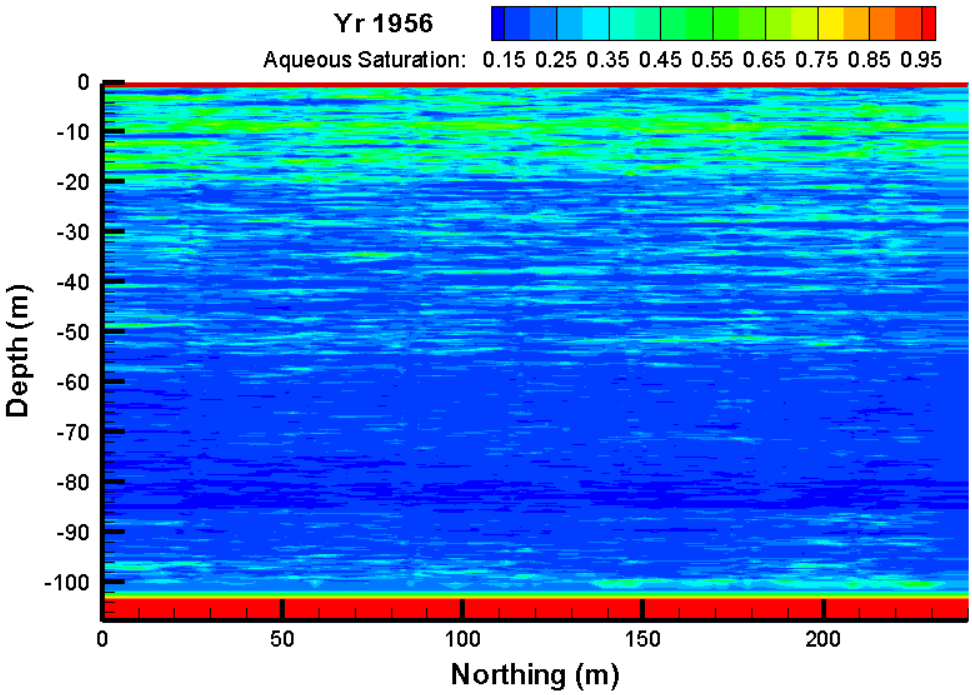


**Figure 5.11. Calculated Aqueous Saturation in 1956, Before Trench Operations, Assuming Spatial Correlation Structure from the 299-E24-111 Field Site**

A clearer picture of the moisture distribution and the effects of the small-scale lithostratigraphy can be obtained from a vertical water-content profile. Figure 5.12 shows a simulated moisture-content profile through the center of Trench 216-B-26. As can be expected, the layers of finer texture are highest in moisture while the coarser layers tend to be drier. The increase in moisture toward the bottom of the profile is caused by the approach to the water table, which is located at 103 m. The simulated water contents range from a low of around 0.05 $m^3$ $m^{-3}$ to a high of just over 0.25 $m^3$ $m^{-3}$. This simulation yielded a mean water content of 0.090 $m^3 m^{-3}$ over the 103-m depth.

Figure 5.13 is a direct comparison among the observed moisture profiles measured by neutron probe during the installation of borehole C4191 in December 2003. The small-scale changes in simulated moisture are quite similar to the moisture contents measured by neutron probe. Furthermore, the range and mean values are quite similar to the observed values. The model does tend to over-predict water content relative to the neutron probe, and the discrepancy appears to increase with depth. This may be due to a probe calibration problem. The borehole was logged in three sections with a different diameter well casing and different casing thickness in each section. These changes are not considered in the model but could be taken care of with a depth-dependent calibration for the neutron probe. Nevertheless, the ability of the model to capture the spatial trends in moisture is quite encouraging and the results provide a measure of confidence in the application of the model to predict field-scale water flow.

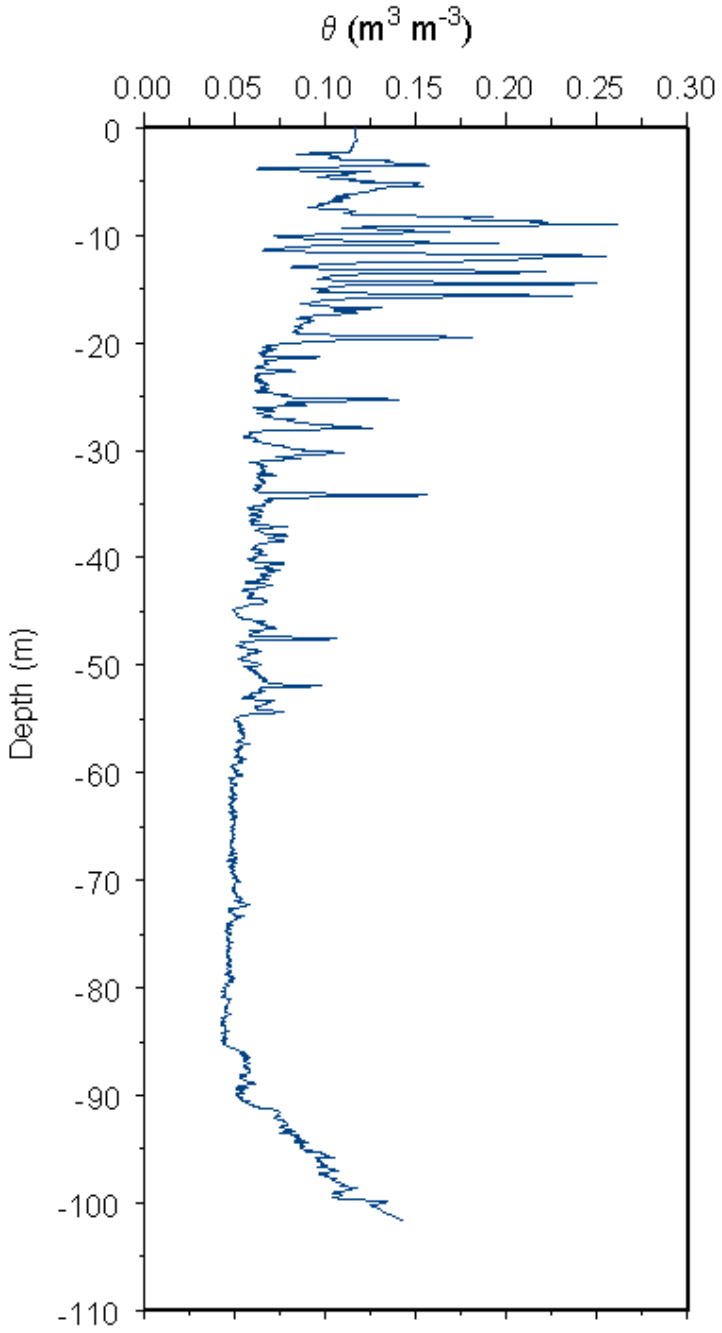


**Figure 5.12. Calculated Profile of Soil Volumetric Water, $\theta(z)$, Through the Center of Trench 216-B-26 in 1956**

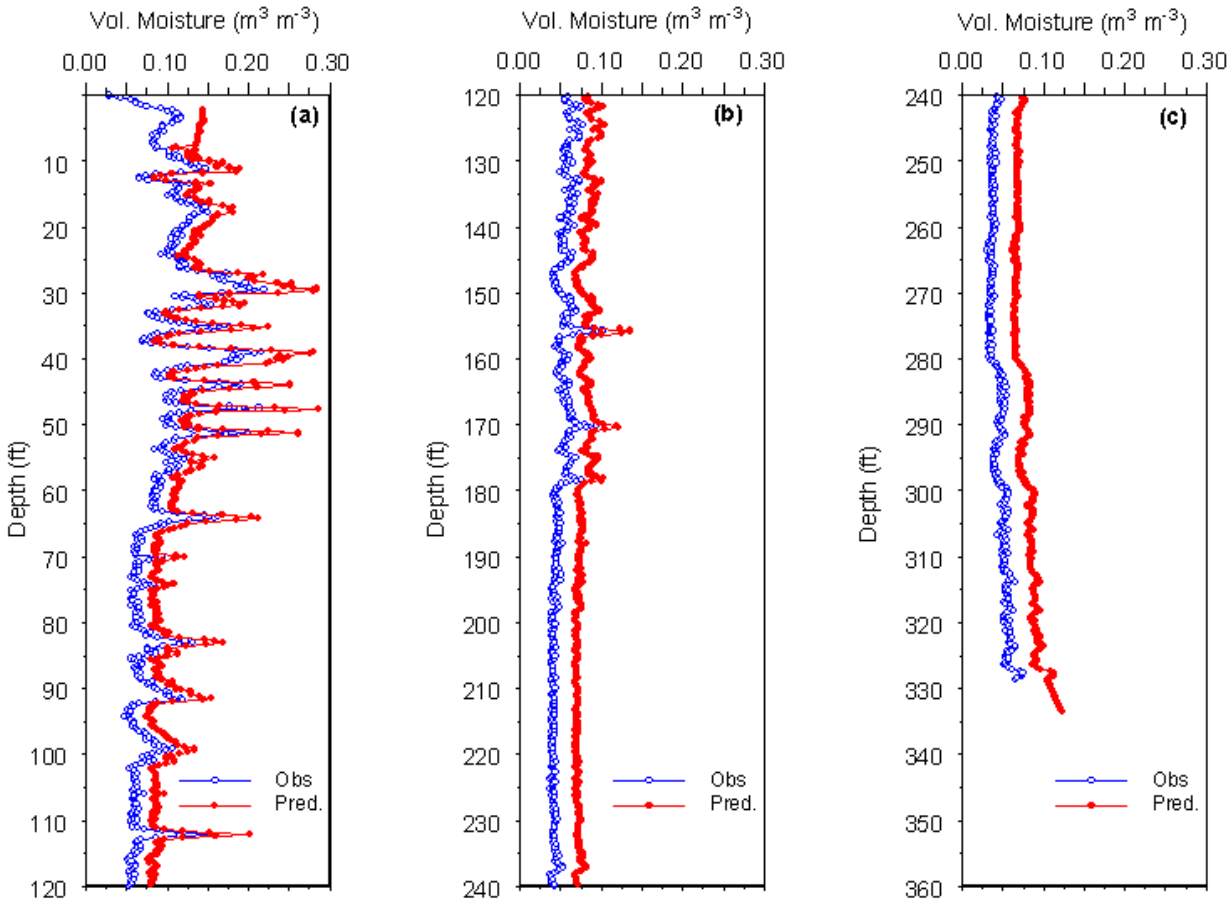


**Figure 5.13. Calculated Profile of Soil Volumetric Water, $\theta(z)$, Through the Center of Trench 216-B-26 in 2004**

### 5.2.2 Distribution of Water During Trench Operations

In a typical study of contaminant fate and transport to support the identification of remedial actions, contaminant distributions are needed from multiple locations to establish the initial condition. In this study, the only available data came from a single borehole installed at 216-B-26. Thus, the approach taken was to simulate the present day contaminant inventory distribution before the effects of the different remedies could be evaluated. This approach is different from that used with the 1-D model where the existing contaminant inventory was used in a convolution solution to predict future migration.

It is known that several waste discharges occurred within the 200-TU OU beginning in 1956 and continuing into early 1958. For this part of the simulation, waste-release information was used to generate the necessary boundary conditions for each trench, and the water and dissolved contaminants were injected at the base of each trench at the appropriate rate. Figure 5.14 through Figure 5.17 show different stages of the injection process. Figure 5.14 shows the distribution of moisture in early December 1956 (t = 1956.837) shortly after the discharge to 216-B-25 started and just before the discharges to 216-B-24 ceased. Flow is mostly lateral to south, and even at this early stage, the wetting fronts from the two

adjacent trenches have already merged. Figure 5.15 shows the distribution of moisture in early February 1957 (t=1957.089). Discharges to 216-B-26 had just ceased and had only just started in 216-B-27. The pattern of moisture distribution persisted with flow controlled by the finer-textured layers. Figure 5.16 shows the moisture distribution on towards the end of June 1957. Discharges to 216-B-28 were coming to a close after a 90-day run in which 5049.8 $m^3$ were discharged. Then discharge to 216-B-28 was 6 percent higher than the discharge to 216-B-26 and by this time there is an increase in the amount of water crossing the simulation boundary. Figure 5.17 shows the distribution on January 01, 1958, just after the discharges to 216-B-52 had ended. This trench received almost twice the average volume received by the other six trenches. Despite some 37,045 $m^3$ of water having been added at this time, it is still mostly in the top 20 m of sediments. As the figure clearly shows, most of the waste water appears to have been redistributed laterally in the shallow subsurface.

A clearer picture of the rate and extent of lateral redistribution can be inferred from the mass flux of water across the north and south boundaries of the simulation domain. The flux of water across the water table was also tracked for comparison. Figure 5.18 shows the water mass flux across the water table during and after trench operations. The mean flux density (recharge rate) across the water table remained at the pre-Hanford value of 3.5 mm $yr^{-1}$ until 1988. After 1988, the simulations show a sharp increase in the flux density at the water table. However, this water is not the water discharged to the trenches but is most likely the antecedent moisture that was pushed ahead by the trench discharges. Recall that it was estimated that the recharge rate from natural precipitation just prior to trench closure was 77 mm $yr^{-1}$ so the moisture content of the soil profile would have been elevated. The concept of a specific retention dictates that a soil column can only hold a finite amount of water against the force of gravity and any water in excess of this amount will drain. The flux density continued to increase, reaching a maximum of about 56 mm $yr^{-1}$ in the year 2004. The simulations show a subsequent decrease in flux density at the water table with the value returning to around 3.5 mm $yr^{-1}$ by 2345. These results are based on the assumption of a mean recharge rate of 3.5 mm $yr^{-1}$ at the surface from 1982 onward and will be discussed further as one of the no-action alternatives. The only evidence of the large 37,045 $m^3$ discharge of waste water might have been an increase in the concentrations of some ions in the groundwater as the resident pore water entered the water table. However, the simulations show that none of the waste water crossed the water table.

The simulated domain was assumed to have a 3 percent dip to the south, which was accommodated in the simulations with a tilted grid. Results show that this dip played an important role in the redistribution of water in the subsurface and as such, the mass flux of water across the north and south boundaries are quite different from that observed at the water table. Figure 5.19 shows a plot of water mass flux across the south (south of B-28) boundary. Owing to the dip to the south, flow was predominantly to south, even though the sequence of trench filling appears to have near the north; 216-B-23 and 216-B-24 were the first to become operational. Flow across the south boundary quickly reached a peak rate of about 17.5 L $day^{-1}$ in early July (t = 1957.56), shortly after 216-B-26 ceased operations. Flow across the boundary has since shown a steady decline except for a few spikes in response to changes in surface boundary conditions.

Thus, these results should be interpreted and treated within the limits of uncertainty of the stratigraphic model and hydraulic parameters. Nevertheless, the model provides useful insight into the transport processes and is best used to provide an indication of the relative contributions of the different

mechanisms rather than absolute contributions. It is expected that as more data become available, these uncertainties will decline.

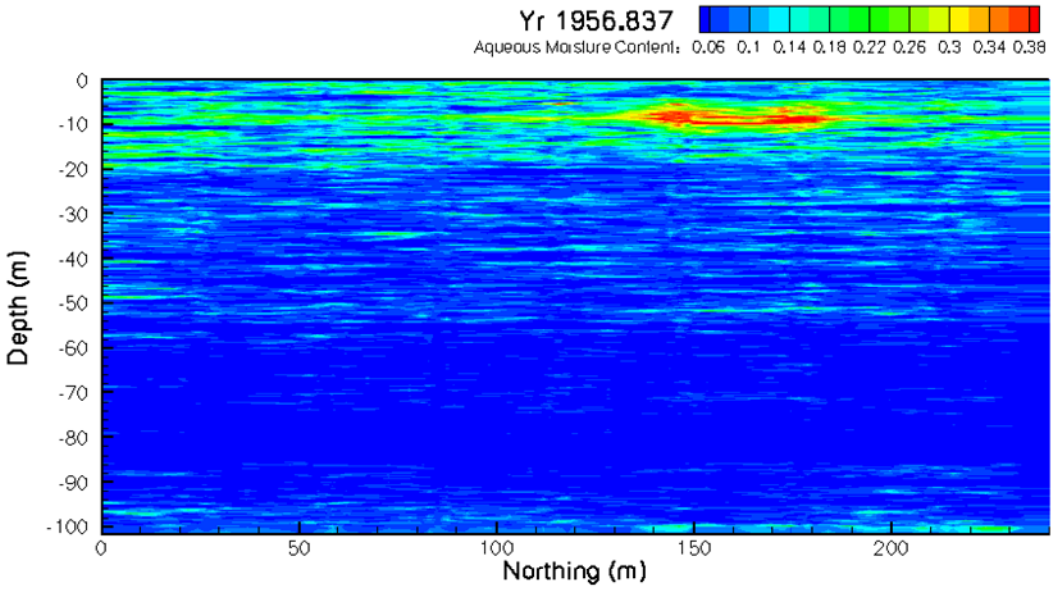


**Figure 5.14. Calculated Distributions of Water Content at year 1956.837 Along a North-South Transect During Trench Operations**

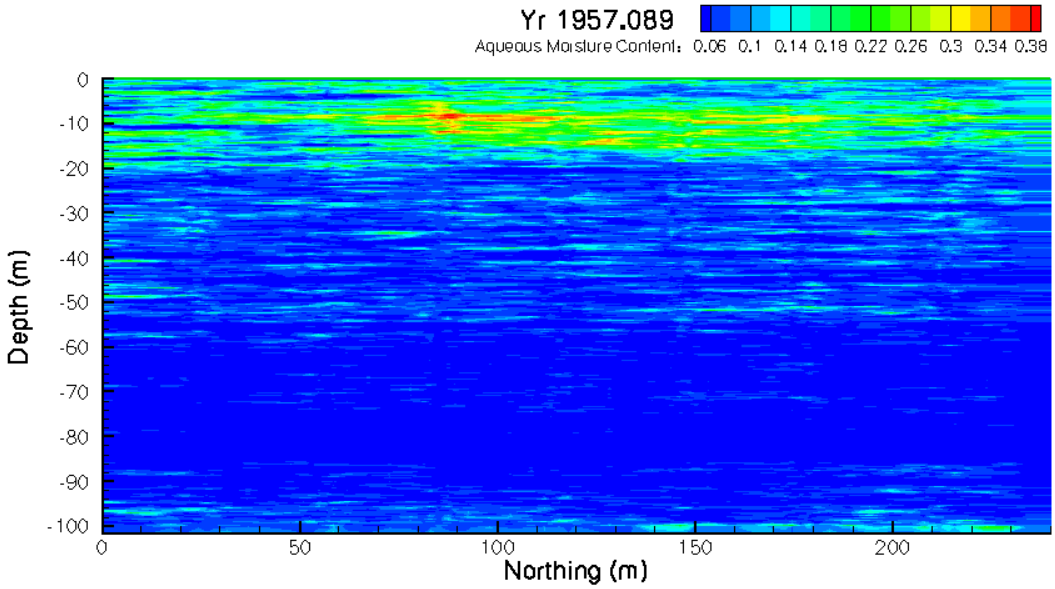


**Figure 5.15. Calculated Distributions of Water Content at time = 1957.089 Along a North-South Transect During Trench Operations**

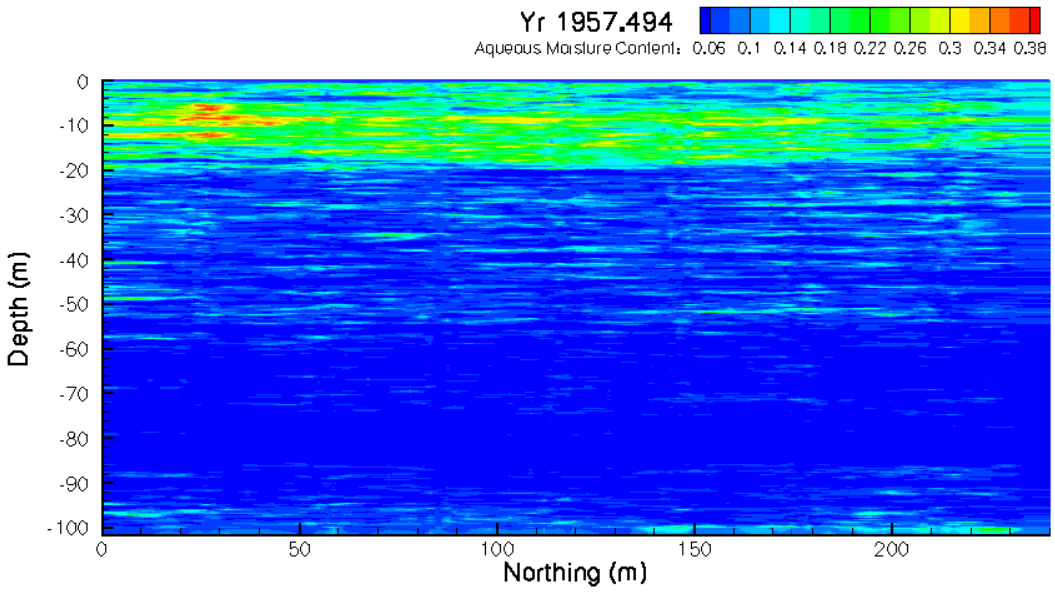


**Figure 5.16. Calculated Distributions of Water Content at time = 1957.494 Along a North-South Transect During Trench Operations**

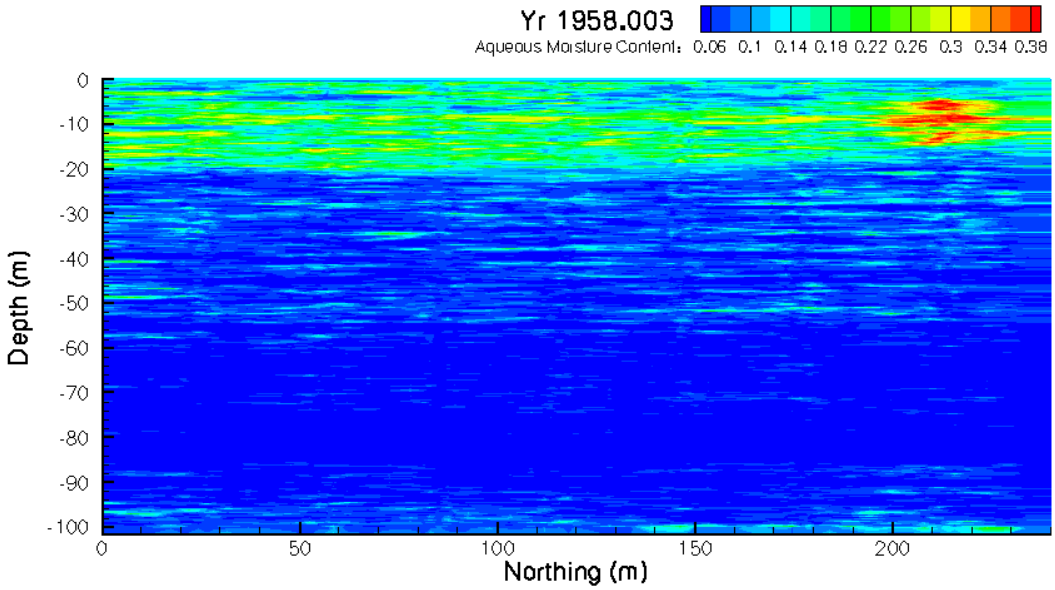


**Figure 5.17. Calculated Distributions of Water Content at year 1958.003 Along a North-South Transect During Trench Operations**

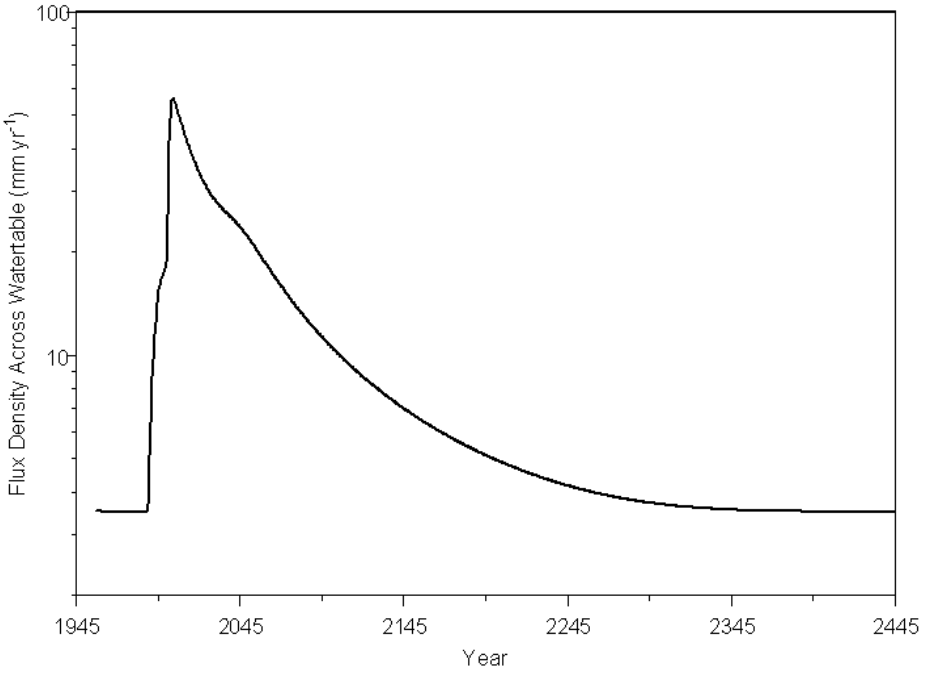


**Figure 5.18. Predicted Mass Flux of Water Across the Water Table During and After Trench Operations**

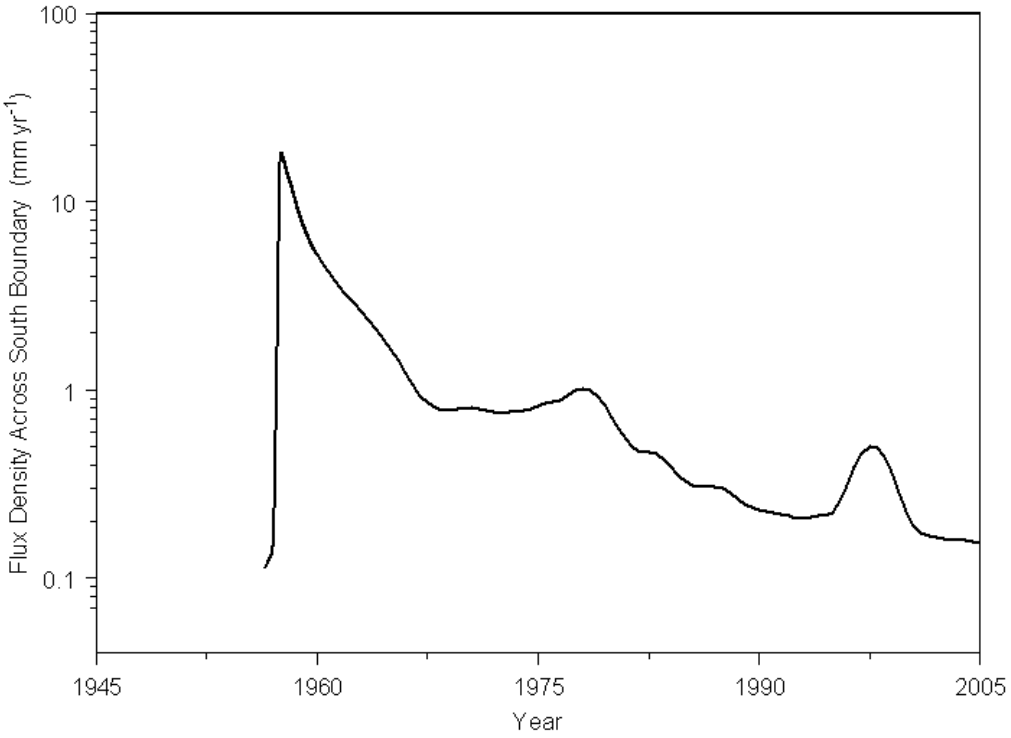


**Figure 5.19. Predicted Mass Flux of Water Across the South (South of B-28) Boundary in Response to Trench Operations**

### 5.2.3 Distribution of Contaminants During Trench Operations

The spatial distribution of contaminants and their mass flux across the different boundaries are examined in a fashion similar to that used for water in the previous section. Figure 5.20 shows the distribution of $^{99}Tc$ in the pore water in early January 1958 (t=1958.003) shortly after the end of discharges to the 216-B-52 trench. This corresponds to the water distribution shown in Figure 5.17. By this time all trench activities had ceased. The $^{99}Tc$ is assumed to be completely in the dissolved in water and assumed to be conservative with zero $K_d$. The same assumptions apply to $NO_3^-$ and because the two species are assumed to have identical diffusion coefficients, the spatial distributions should be similar (Figure 5.21). For both species, sorption and anion-exclusion effects are ignored. The spatial distribution of $^{238}U$ shows a bit more heterogeneity than the $NO_3^-$ and $^{99}Tc$ plumes (Figure 5.22). This is because the $K_d$ of $^{238}$ U was allowed to vary with soil texture with the finer textured sediments having a higher $K_d$, than the coarser sediments. The result is a distribution that shows slightly increased mobility in the coarser materials than in the fine-textured lenses.

Unlike previous analyses in which small-scale stratigraphic changes are ignored, these simulations show that the mobile species ($^{99}Tc$ and $NO_3^-$) moves laterally with the water and remains high above the water table, even after 47 years in the ground. The pattern of migration of $^{99}Tc$ and $NO_3^-$ across the boundaries should therefore mimic that of water to a large extent. Figure 5.23 shows a plot of the time distribution of $^{99}Tc$ crossing the south boundary in response to trench discharges. There was a general increase in the flux of $^{99}Tc$ over time, which is consistent with the sequential nature of trench operations. Figure 5.23 show several sharp changes in concentration that coincide with those observed in the water flux. In general, high fluxes of water resulted in reductions in the $^{99}Tc$ concentration. This can be expected since $^{99}Tc$ is transported in the water. These changes are mostly due to changes in surface boundary conditions. However, the multimodal features are also partly related to the heterogeneity. Lateral flow could be expected to dominate until the potential gradients were sufficient to overcome the entry pressure of underlying coarse layers. The dependence of the flow network on saturation would give rise to transient effects rand the features observed in Figure 5.19and Figure 5.23. Simulations show that the peak in mass flux occurred several years after the discharges ended. The peak $^{99}Tc$ crossing the south boundary occurred in mid 1985 with a aqueous concentration of $1.79 \cdot 10^6$ pCi $L^{-1}$. This is about an order of magnitude higher than the peak concentration of $3.2 \cdot 10^5$ pCi $L^{-1}$ observed in 1962 shortly trench discharges ceased.

An obvious question is why the water flux and $^{99}Tc$ flux patterns are so different. It is likely that water present in the soil would have been displaced ahead of the discharged fluids thereby crossing the boundary before the actual waste water did. However, the same would not happen for $^{99}Tc$ because the initial concentration of $^{99}Tc$ in the soil was assumed to be zero and any antecedent water initially displaced would have been free of $^{99}Tc$. Because transport of solutes occurs via both advection and dispersion, it is possible that even though advection has essentially ceased, diffusion could still be occurring, especially given the large concentration gradient. However, movement by diffusion would be very difficult to observe in the field. It should be noted that nitrate distributions showed a similar pattern to behavior to $^{99}Tc$; migrations was primarily to the south and none entered the groundwater.

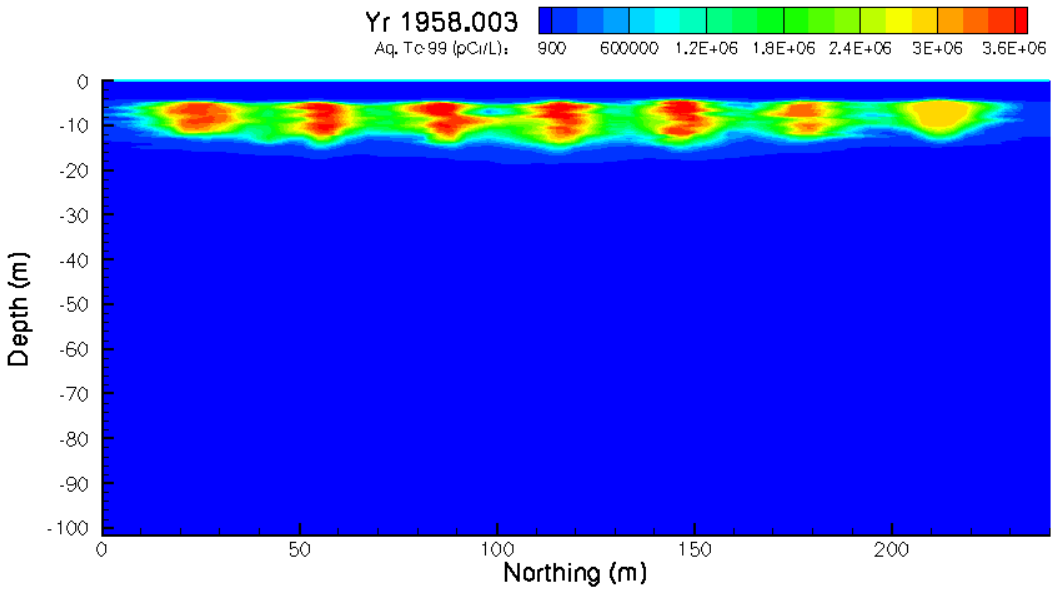


**Figure 5.20. Calculated Distributions of Aqueous $^{99}$Tc in the Year 1958.003**

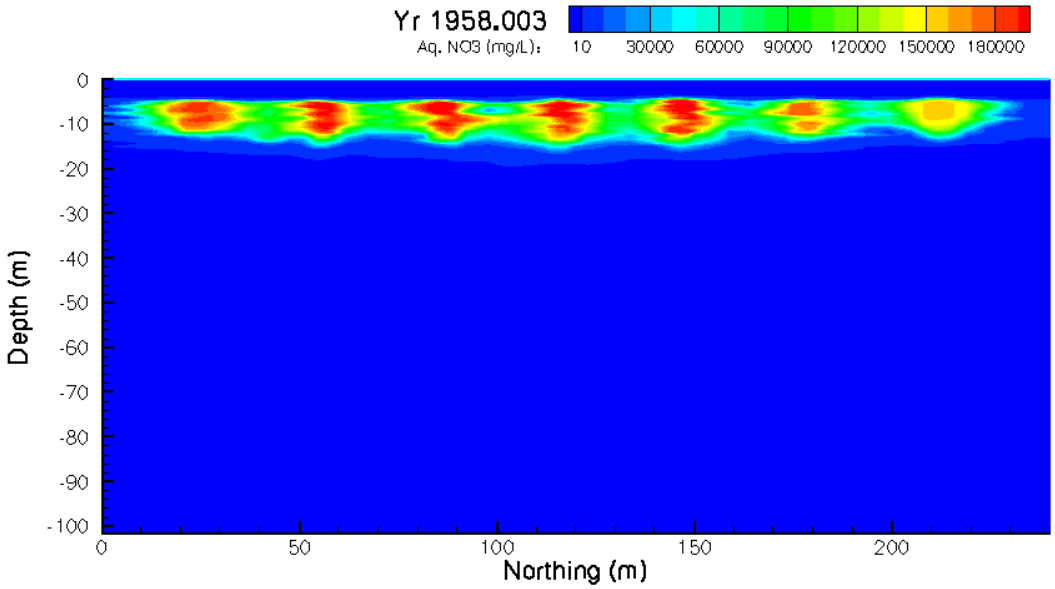


**Figure 5.21. Calculated Distributions of Aqueous $NO_3^-$ in the Year 1958.003**

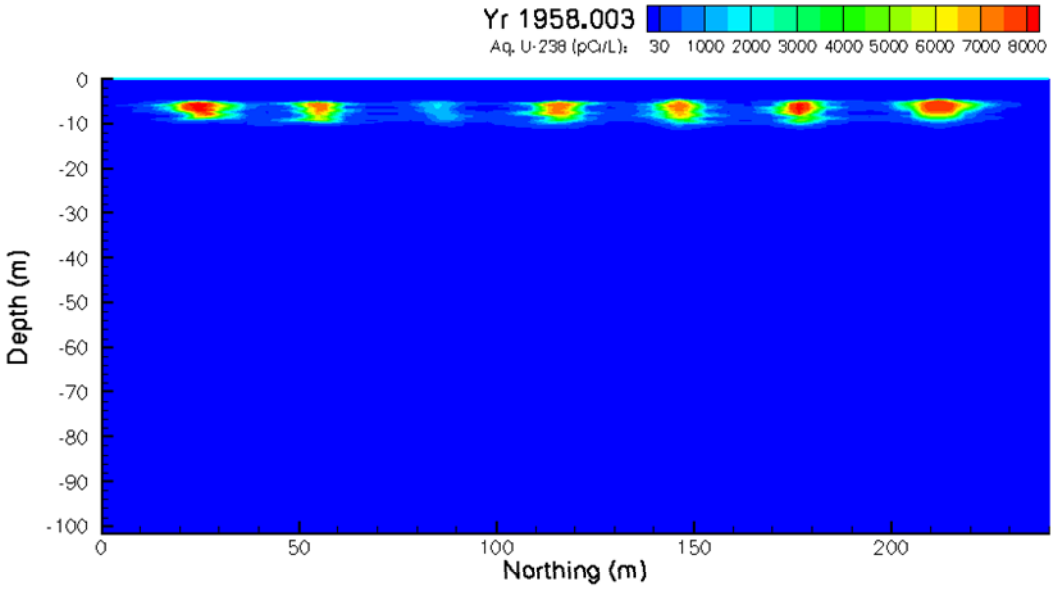


**Figure 5.22. Calculated Distributions of Aqueous $^{238}U$ in the Year 1956.9172**


**Figure 5.23. Predicted Mass Flux of $^{99}Tc$ Across the South Boundary From Trench Operations**

The presence of small-scale textural discontinuities such as those observed in Figure 2.2 is responsible for the variations in moisture contents observed in the neutron-probe measurements. These heterogeneities may have led to the development of complex flow networks whose impacts dominate those resulting from the large-scale heterogeneity that is typically the focus of transport simulations on site. The characteristics of these flow networks appear to vary with input flux and boundary type. The results provide new insight into the interpretation of existing contaminant distribution, field-scale experiments, and the design of remedial systems for contaminated soils. Changes in saturation can completely change the subsurface flow network, thereby influencing the spatial correlation structure of relative permeability and the location of fast paths. This suggests that solute transport may be strongly dependent on saturation in a way more complicated than the simple effect on the pore-water velocity. In such systems, the amount of lateral spreading observed would strongly depend on the flow regime. There is experimental evidence that shows that the horizontal permeability of laminated silts from the Hanford vadose zone can be over 70 times the vertical permeability (Ward and Gee 2003).

These factors have important consequences for field-scale transport and remediation. Contaminants deposited under a massive leak or discharge of waste water, as with the BC cribs and trenches, would show preferential lateral movement initially due to a combination of large lateral potential gradients and large horizontal saturated conductivities. At the much lower natural recharge rates, lateral potential gradients would be significantly smaller. Even though saturation-dependent anisotropy predicts an increased tendency for lateral migration, the hydraulic conductivity at low water contents may be too low to significantly affect redistribution at the low potential gradients. This is of particular importance to the fine-textured lenses that currently show higher water contents in the field. Even though the hydraulic conductivity is higher than that of drier adjacent sands, the actual values of conductivity are such that continued lateral migration would be at very low rates. However, significant vertical migration would also require conditions that were wet enough to overcome the natural capillary breaks.

### 5.2.4 Current Distribution of Contaminants

Figure 5.24 shows the predicted distribution of $^{99}$Tc at the beginning of year 2005. In general the predicted plume is located mostly between 20 and 50 m. The current conceptual model suggests that the discharges from the seven trenches initially moved laterally to merge into a single plume. Natural recharge then leached the trailing edge of the plume downward effectively reducing the concentration of the mobile contaminants in the 0 to 20-m depth to background levels. The plume shows some effects of the heterogeneity in that it is asymmetric. Under 216-B-26 where the C4191 borehole was installed (northing =110 m) the plume is located between 23 and 50 m. In the absence of multidimensional plume distribution data, comparisons between the simulated and observed $^{99}$Tc distribution are based on data from the C4191 borehole. In order to make this comparison, we extracted a 1-D profile beneath the 216-B-26 trench at the approximate location of the C4191 borehole. Figure 5.25 through Figure 5.29 compare the predicted depth profiles for the three contaminants on which this study was focused.

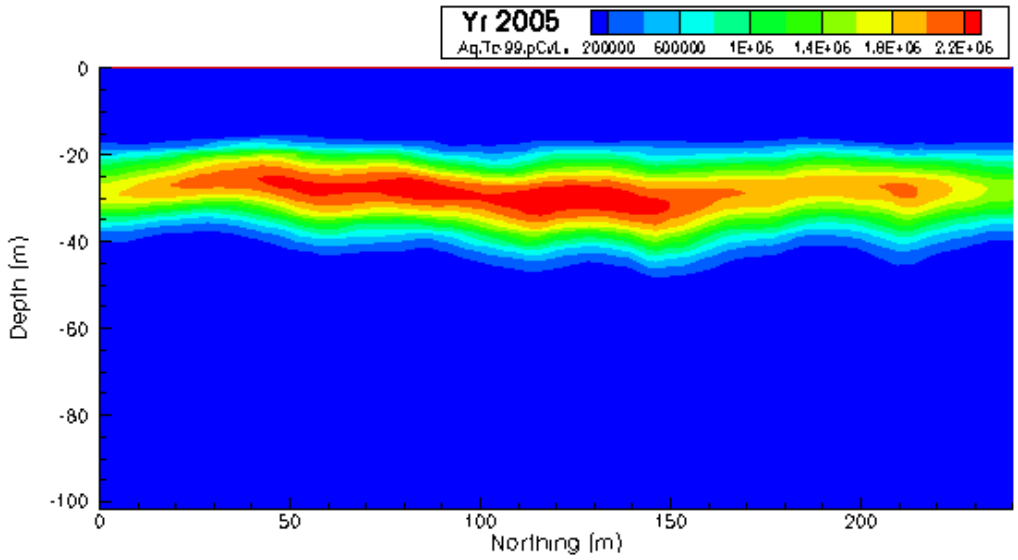


**Figure 5.24. Calculated Distributions of Aqueous $^{99}$Tc in the Year 2005**

Figure 5.25 compares the predicted and observed $^{238}$U profiles. Field observations show a bimodal distribution with peaks at 6 and 13 m. However, the predicted profile does not show this feature. The distribution is single peaked and centered around 12 m with a maximum concentration that is about 1/3 of the observed concentration. The difference between the predicted and observed distributions could be due to at least two factors. First, the higher observed concentration just beneath the bottom on the trench could be due to an elevated $K_d$. Data from this borehole show relatively large pH values at the bottom of the trench which could cause $^{238}$U to precipitate. In fact, the observed profile of total acid extractable U is indicative of high sorption just beneath the trench. However, the current conceptual model is based a simple linear sorption isotherm for $^{238}$U. The $K_d$ values were derived from the estimates published by Cantrell et al. (2003) but does not account for pH in any way. A lower than expected $K_d$ in the model would lead to higher mobility in the predicted plume. Predictions of both pore-water and total concentrations show an under-prediction by the model. The discrepancy in total $^{238}$U suggests that the median values of $^{238}$U inventory used as model inputs and derived from the SIMS model may be too low. In addition, the deeper depth of penetration of the predicted plume suggests that the $K_d$ values used in the model may have been too low. It may also be indicative of an over-simplified model for the sorption of $^{238}$U. Nevertheless, the distribution of $^{238}$U provides some insight into the actual depth of penetration of the original scavenged waste fluids. Owing to the relatively high $K_d$ of $^{238}$U, it is unlikely that it could have been leached to its current position by natural recharge. Inverse modeling with an ion-exchange model could provide some further insight.

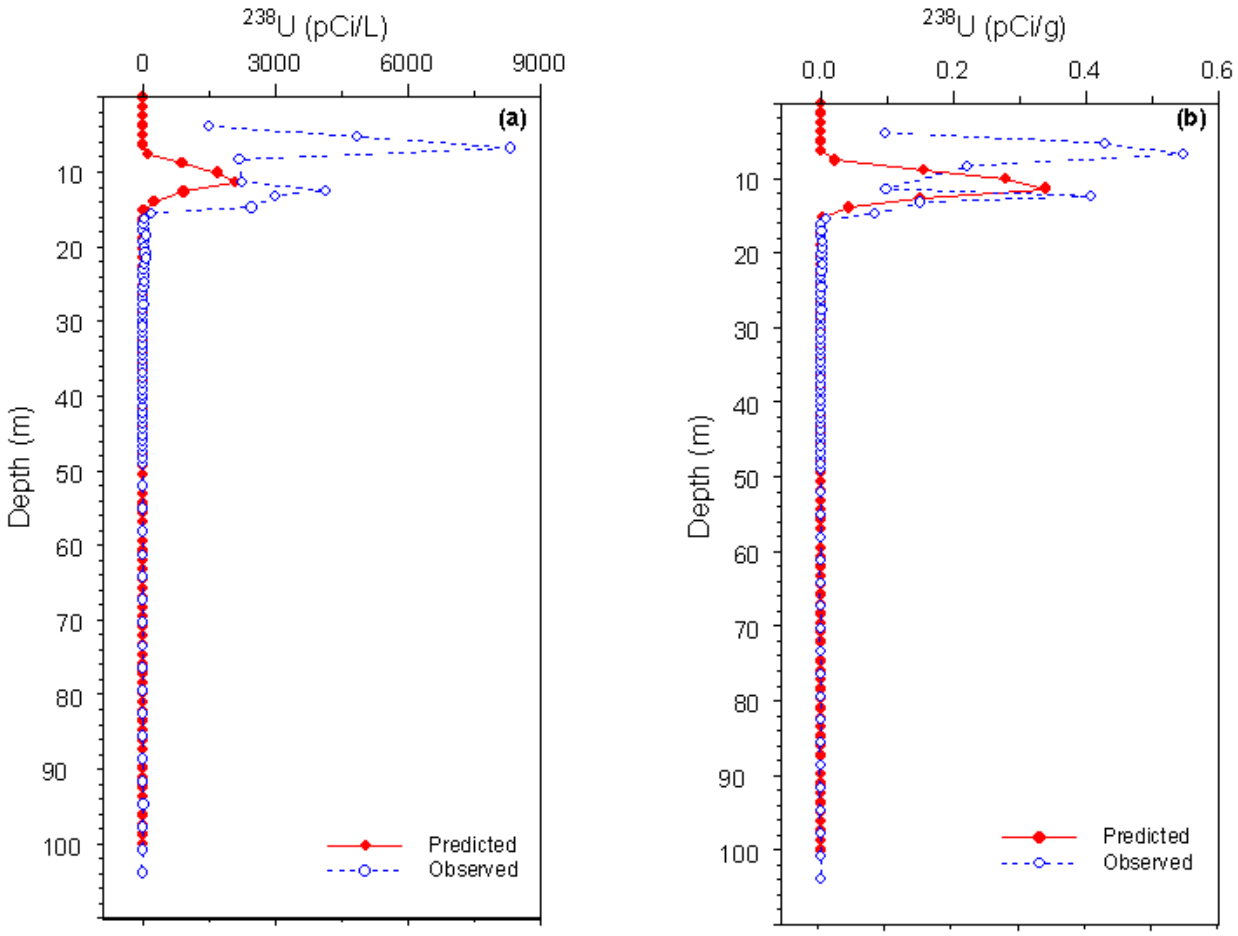


**Figure 5.25. Observed and Predicted Distributions of (a) Aqueous $^{238}U$, and (b) Total $^{238}U$ in Yr 2005 at Borehole C4191**

Figure 5.26 compares the predicted and observed $^{99}Tc$ profiles. The general trends are remarkably similar given the uncertainty in hydrologic properties and the lack of characterization data. The center of mass of the predicted $^{99}Tc$ is located around 30 m, and the leading edge of the plume extends to around 50 m as in the case of the measured plume. However, there are major differences, particularly in the spatial distribution about the mean depth and the peak concentration. These discrepancies can be easily explained.

First, we deal with the absence of the multimodal distributions in the lab data in Figure 5.26. This may be an artifact of the sampling method as it is unusual for a contaminant profile, expressed in terms of mass units per volume of pore water, to show such a feature. Pore-water extracts are typically determined in terms of the mass of contaminant per unit mass of soil and are converted to concentration per unit volume of pore by multiplying by the volumetric water content dividing by the bulk density. If water content and bulk density varies with depth, as is usually the case in natural soils and sediments, then scaling by these

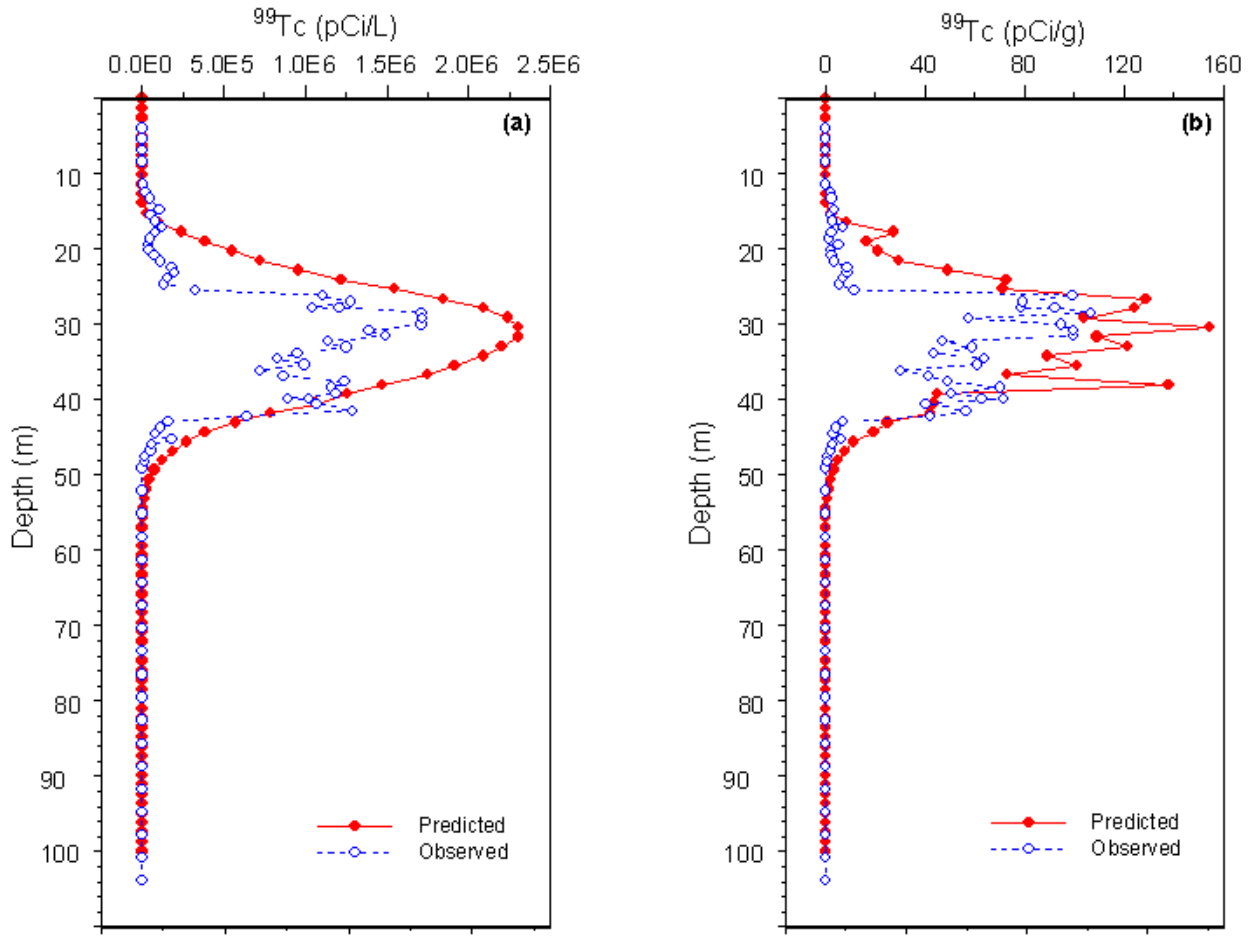


**Figure 5.26. Observed and Predicted Distributions of (a) Aqueous $^{99}$Tc, and (b) Total $^{99}$Tc in Yr 2005 at Borehole C4191**

variables should produce a smooth bell-shaped curve as seen in the model predictions. In contrast, the assumption of a mean bulk density or under-estimation of the water content could lead to the bimodal curve. Because our model takes the depth variations in bulk density and water content into account, a smooth curve is generated for the aqueous $^{99}$Tc. When concentration is expressed as the total $^{99}$Tc concentration, i.e. concentration per unit volume of soil, the effects of depth variations in water content and bulk density are readily apparent (Figure 5.26b). This plot clearly shows the effects of small-scale heterogeneities on the spatial distribution of total $^{99}$Tc.

The next issue relates to the difference in dispersion and peak concentrations. While the model captures the leading edge of the plume quite well, the trailing edge appears to have been insufficiently leached, thereby giving an apparently larger value of dispersion. Yet, the model predicts a higher peak concentration. There are features of transport in unsaturated soils that are often reported in the literature and have been observed at Hanford that can explain these discrepancies. First, the local longitudinal (vertical) dispersion of contaminants is strongly dependent on the measuring volume. Consequently,

dispersion typically appears smaller when derived from small sampling volumes, such as boreholes, than for the volume of field samples at which large-scale results are desired (Hammel et al. 1999). Thus, the apparent dispersion derived from measurements in the C4191 borehole can be expected to be smaller than those predicted by the model. Another factor that could contribute to this discrepancy is the dimensionality effect. In the field, horizontal redistribution leading to solute mass accumulation where local flow converges and depletion where it diverges is entirely possible. However, using a 2-D profile for the simulations limits the extent to which redistribution can occur. As noted by Burnett and Frind (1987), only transient multidimensional simulations are capable of producing the actual concentration values that are observed in the field that drive local processes, including chemical reactions and diffusion.

While both of these factors may be responsible for the higher predicted concentrations, the simultaneous prediction of higher apparent dispersion with a higher peak concentration creates a dilemma. The fact that predicted total $^{99}Tc$ is higher than the observed, even though dispersion is greater, suggests that the inventory used as input may be too high. The input values for $^{99}Tc$ is based on the median values derived from the SIMS model. Given that the solution to the transport equation is linear, it can be solved for a unit mass of input and scaled to the appropriate input value until the actual concentrations match. An adequate match between the observed and predicted can be achieved by reducing the input inventory by around 50 percent. Nevertheless, the fact that the difference in peak concentration is only 50 percent, even with uncertainty in inventory and model dimensionality, is again quite remarkable.

Figure 5.27 compares the predicted and observed profiles for $NO_3^-$. As with the $^{99}Tc$ distribution, the general trends are remarkably similar, except in this case the model underestimates the concentrations relative to the observed. The explanations advanced above for the discrepancies in the $^{99}Tc$ are also applicable for $NO_3^-$. The predicted center of mass is quite similar but the predicted peak concentrations based on the input inventory is less than the observed. In fact, the predicted peak concentration is only 1/3 that of the observed. Given that the transport behavior of $^{99}Tc$ and $NO_3^-$ are expected to be similar, the amount of dispersion in an advection dominated environment can be expected to be similar. Thus, the only possible explanation for the lower predicted $NO_3^-$, in the absence of decreased dispersion, is an underestimation of the input $NO_3^-$ inventory. As with the $^{238}U$ and $^{99}Tc$ predictions, $NO_3^-$ predictions are based on the median value from the SIMS model runs.

The C4191 borehole cannot provide any validation of the extent of spreading predicted by the model. Confirmation can come only from further sampling or from non-invasive geophysical logging that can delineate the extent of the plume. It is expected that as such data become available revisions would be made to the conceptual model to minimize any discrepancies between observations and model simulations.

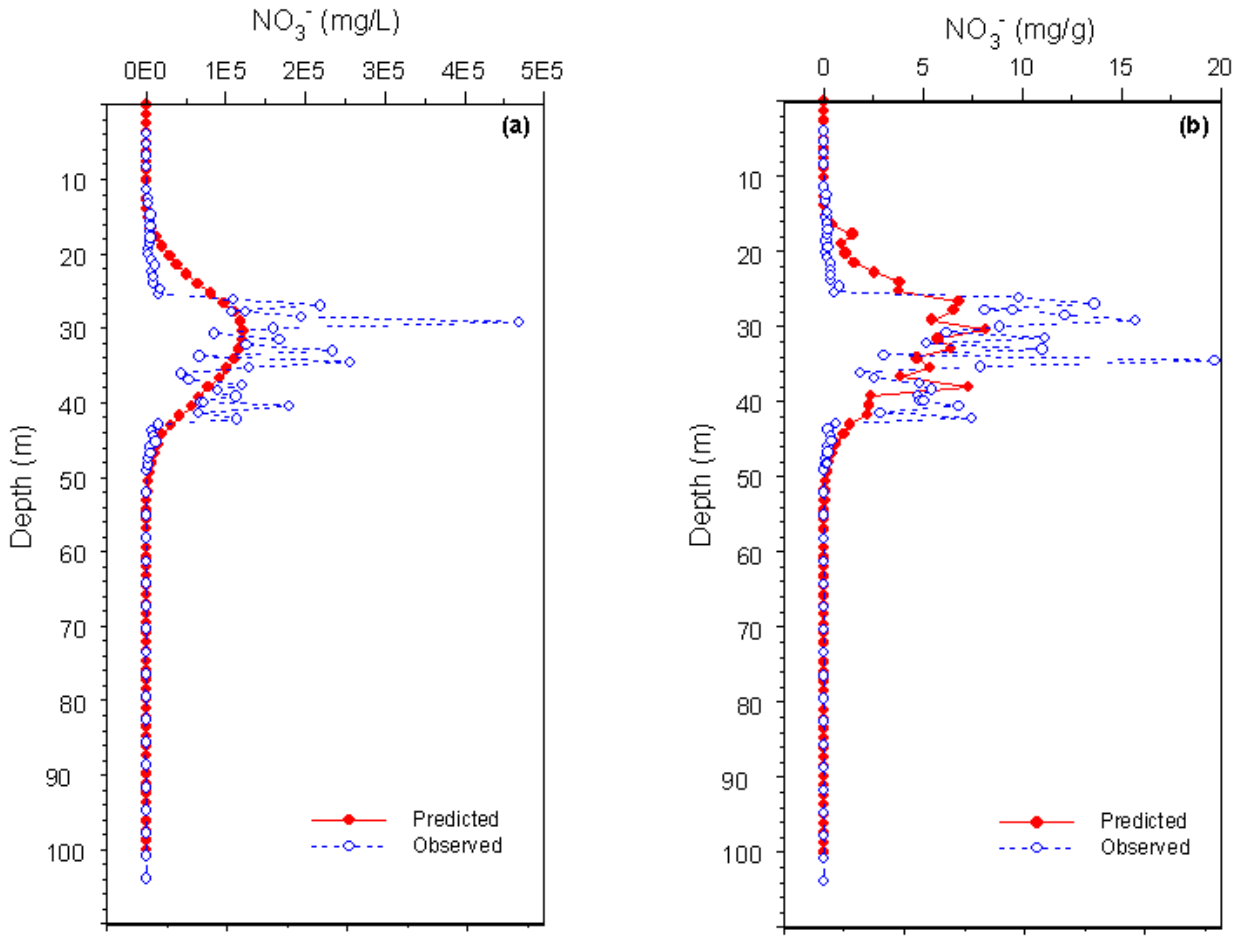


**Figure 5.27. Observed and Predicted Distributions of (a) Aqueous $NO_3^-$, and (b) Total $NO_3^-$ in Yr 2005 at Borehole C4191**

### 5.2.5 Soil-Screening Levels Following the No-action Alternative

Figure 5.28 shows the predicted pore-water concentrations for $^{99}Tc$ in the year 2400 shortly after the arrival of the MCL (900 pCi L-1) at the water table in year 2324 under the no-action alternative of 3.5 mm $yr^{-1}$. The first arrival (arrival of 10 percent of the MCL) at the water table occurred in 2127 and at the receptor well in 2353 (Table 5.4). Figure 5.29 and shows the predicted pore-water concentrations for $^{99}Tc$ in the year 3000, after the arrival of the peak at the same recharge rate. The peak concentration reaching the receptor well is 3147 pCi/L, which exceeds the MCL for $^{99}Tc$. The same applies to $NO_3^-$ with a concentration of 165 pCi/L arriving at the receptor well. When compared to the 1D model, a multidimensional model allows redistribution of the plume in the longitudinal and transverse horizontal directions. Although such redistributions bring about reductions in concentrations, significant changes do not occur for $^{99}Tc$ simply because of the large inventory of $^{99}Tc$ and the long half life. Thus, in all cases of no-action, soil-screening levels are exceeded and the concentration reaching the water table and receptor would likely exceed the MCL.

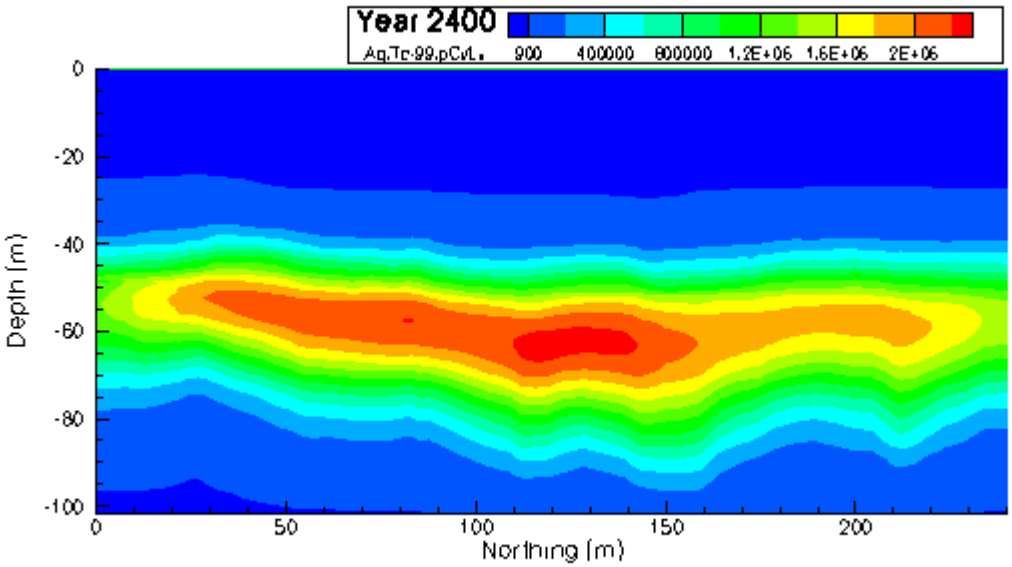


**Figure 5.28. Calculated Distributions of Aqueous $^{99}$Tc in the Year 2400 (3.5 mm/yr)**

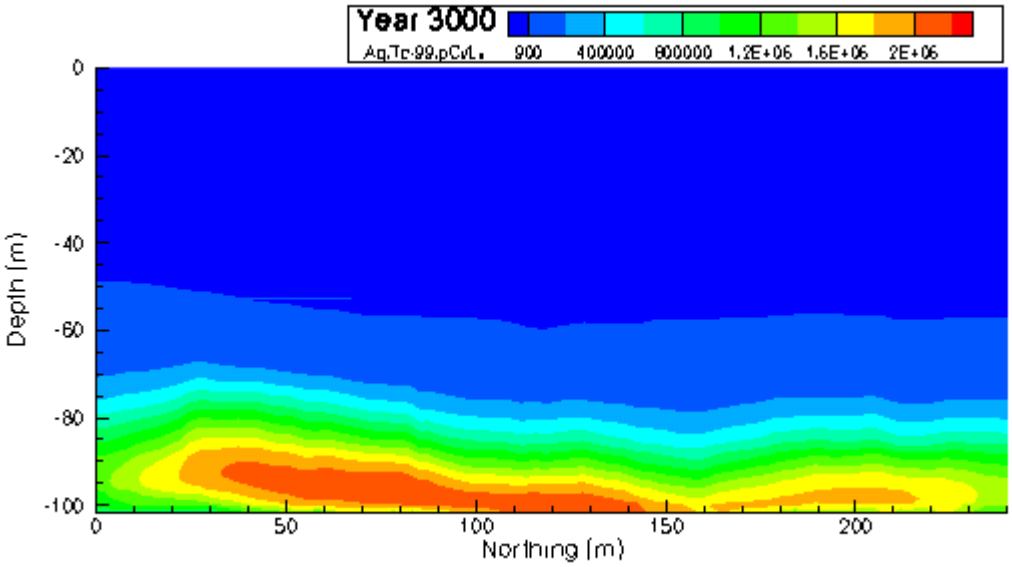


**Figure 5.29. Calculated Distributions of Aqueous $^{99}$Tc in the Year 3000 (3.5 mm/yr).**

### 5.2.6 Arrival Times and Concentrations Under the No-action Alternative

Figure 5.30 through Figure 5.33 show the mass flux of $^{99}Tc$ and $NO_3^-$ at a receptor 100 m down-gradient of the source under the no-action alternatives. A summary of arrival time and concentrations at the water table and a receptor is provided in Table 5.4. With the current conceptualization and model parameters, the first arrival of $^{99}Tc$ occurs at the receptor in 2118 at the 25 mm/yr recharge rate. A peak concentration of $2.09 \cdot 10^4$ pCi/L arrives in 2228. A recharge rate of 25 mm $yr^{-1}$ leads to a peak $^{99}Tc$ concentration of $3.6 \cdot 10^5$ pCi $L^{-1}$ reaching the water table in the year 2095. At the 3.5 mm $yr^{-1}$ recharge, first arrival of $^{99}Tc$at the receptor is in 2353 with the MCL arriving in 2600 and a peak of 3147 pCi/L arriving in 2991. Nitrate shows similar trends although the first arrival is generally earlier due to the larger concentrations of $NO_3^-$ and the relatively low MCL. At the 25 mm/yr, the MCL for $NO_3^-$ reaches the water table in 2125 but is delayed for another 295 years, arriving in 2420 under a recharge of 3.5 mm $yr^{-1}$. In all cases, the concentration reaching the water table increased with a decreasing recharge. The increase in concentration can be expected because a reduction in pore water velocity would cause a reduction the dispersion coefficient. A smaller amount of dispersion would mean higher peak concentrations. However, as shown in Table 5.4, concentrations arriving at the receptor decreased significantly as the recharge rate decreased.

These results are consistent with the 1-D simulations in which the existing plume was allowed to migrate under steady flow to the water table. However, as pointed out earlier, it would have been impossible to make independent predictions of the current inventory distribution based on 1-D simulations. An important point to note is the sensitivity to recharge estimates for the no-action alternative. As shown by the simulation results, accurate predictions of the initial distribution of the plume were strongly influenced by the quality of information available for the discharge volumes and contaminant inventory and the conceptual model. However, subsequent redistribution of the contaminants is strongly influenced by the assumed recharge, which is an unknown in this analysis.

Recharge rates used in the simulations were also assumed to be time invariant. This may explain the relatively symmetric nature of the breakthrough curves compared to that observed on the south boundary that was subject to the short-term effects of changes in water flux. It is expected that the use of recharge that is a percentage of precipitation, such that episodic high-flux events can be captured, may produce somewhat different distributions. Such a scenario could see moisture conditions in the soil reaching a level at which the water-entry pressure of coarse layers could be overcome and deep drainage rates increase to bring about episodic entries of $^{99}Tc$ and $NO_3^-$ into the groundwater.

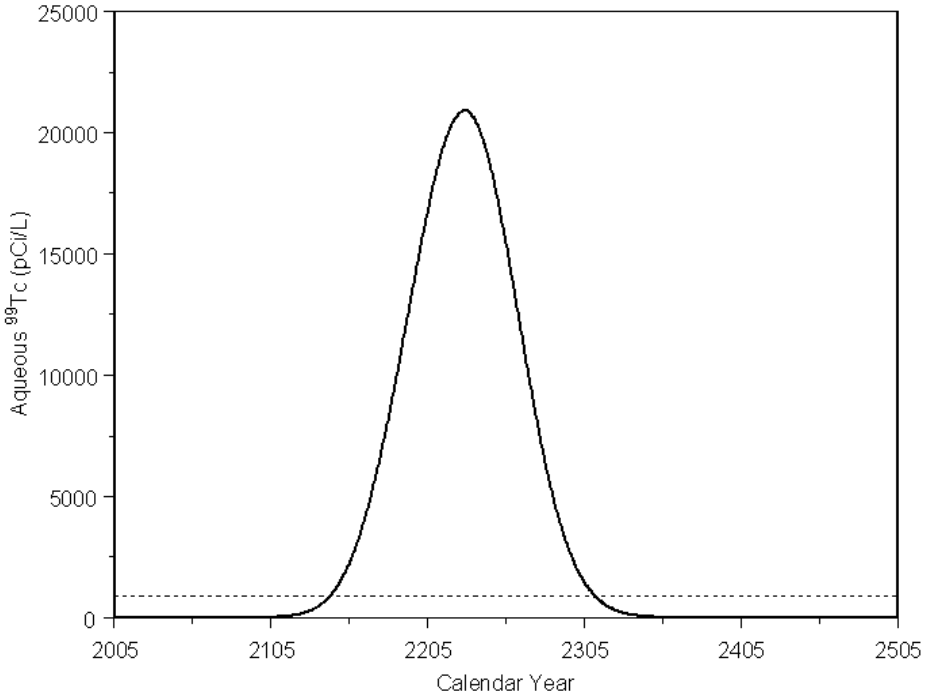


**Figure 5.30. Calculated Distributions for $^{99}$Tc at a Hypothetical Receptor well Under a Recharge Rate of 25 mm/yr Based on STOMP Simulations. The dotted line is the MCL of 900 pCi/L.**

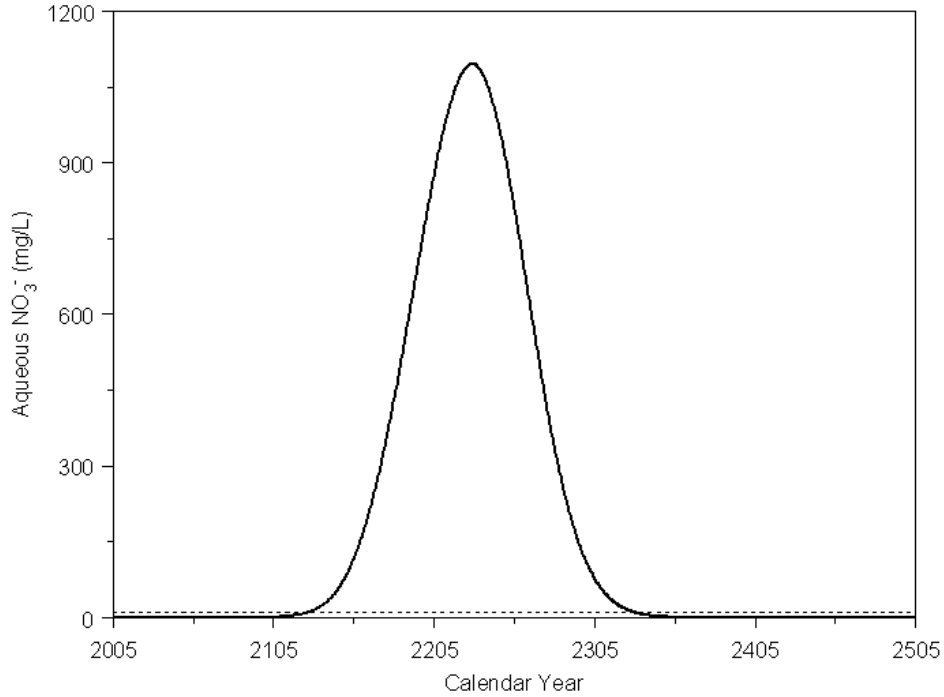


**Figure 5.31. Calculated Distributions for $NO_3^-$ at at a Hypothetical Receptor well Under a Recharge Rate of 25 mm/yr Based on STOMP Simulations. The dotted line is the MCL of 10 mg/L.**

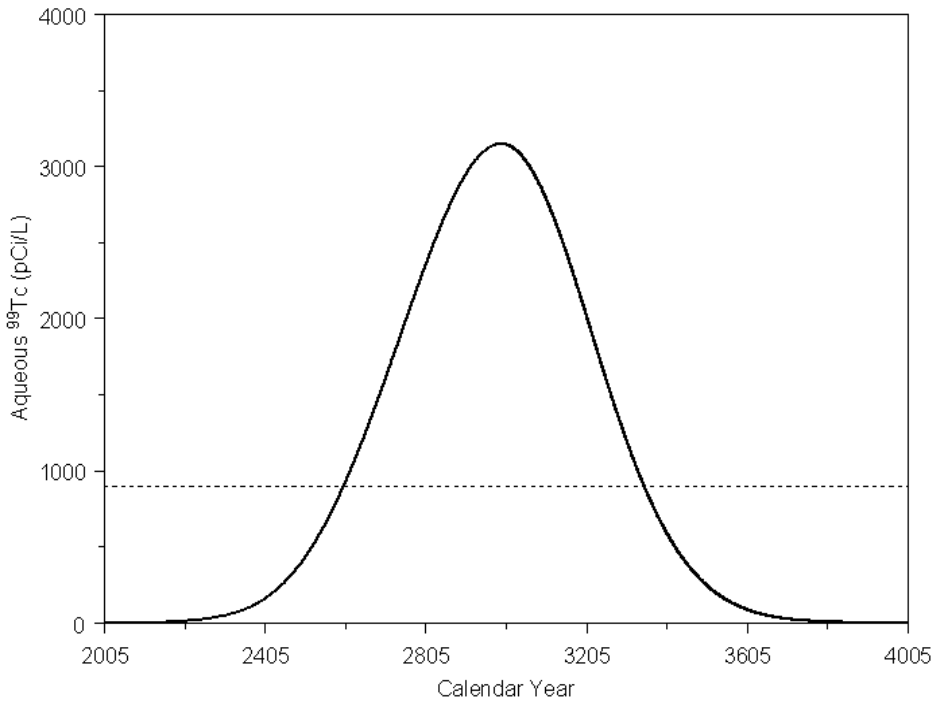


**Figure 5.32. Calculated Distributions for $^{99}$Tc at at a Hypothetical Receptor well Under a Recharge Rate of 3.5 mm/yr based on STOMP Simulations. The dotted line is the MCL of 900 pCi/L.**

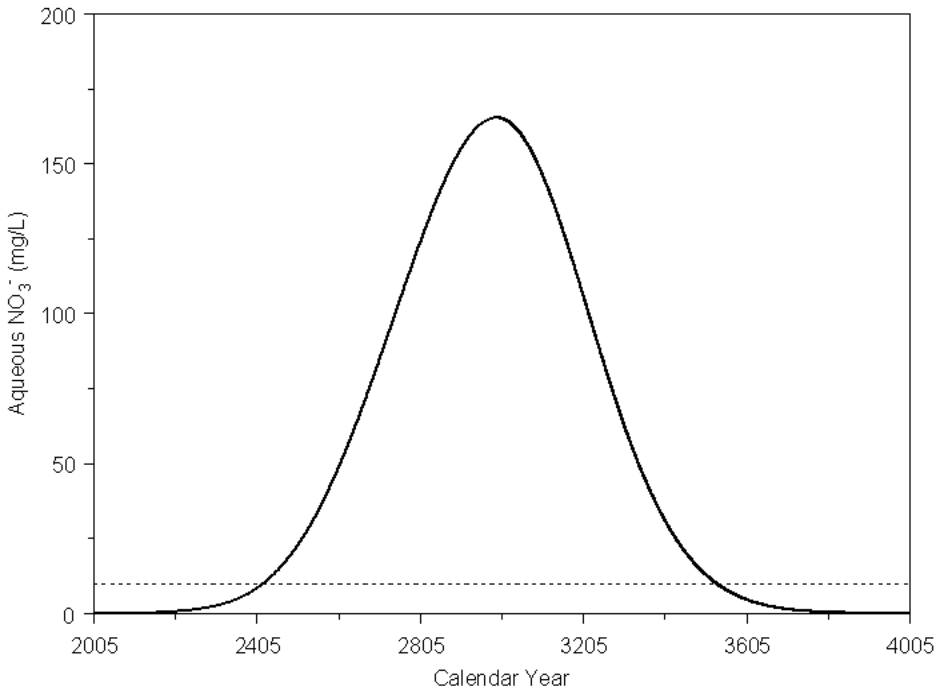


**Figure 5.33. Calculated Distributions for $NO_3^-$ at a Hypothetical Receptor well Under a Recharge Rate of 3.5 mm/yr based on STOMP Simulations. The dotted line is the MCL of 10 mg/L.**

### 5.2.7 Soil-Screening Levels Under the Capping Alternatives

Spatial distributions of $^{99}Tc$, $NO_3^-$, and $^{238}U$ were simulated over time for three hypothetical caps that limited recharge to 0.5, 0.1 and 0.0 mm $yr^{-1}$. Figure 5.34 shows the predicted pore-water concentrations for $^{99}Tc$ in the year 2400 shortly after the arrival of the MCL at the water table under the 0.5 mm $yr^{-1}$ barrier. Figure 5.35 shows a similar plot after the arrival of the peak. Although the first arrival, arrival of the MCL, and arrival of the peak all occur considerably later than in the no-action alternative, there is no significant change in peak concentrations. Although the concentrations reaching the water table are higher than the no action alternative, the values observed at the receptor well are much smaller and are actually below the MCLs. To gain further insight into the impact of capping alternative on the contaminant inventory and groundwater quality, we calculated the concentrations of $^{99}Tc$ and $NO_3^-$ entering the water and receptor well for the different capping strategies. The mass flux of contaminant at the water table was calculated according to Equation 3.20.

### 5.2.8 Arrival Times and Concentrations Under the Capping Alternatives

Figure 5.36 shows the mass flux of $^{99}Tc$ while the mass flux of $NO_3^-$, is shown in Figure 5.37. The plots represent contaminant breakthrough at the receptor well under a 0.5 mm $yr^{-1}$ barrier based on the STOMP simulations. Similar plots are shown for the 0.1 mm $yr^{-1}$ barrier in Figure 5.38 and Figure 5.39. Results for the hypothetical 0.0 mm $yr^{-1}$ barrier are shown for $^{99}Tc$ and $NO_3^-$ in Figure 5.40 and Figure 5.41, respectively. Table 5.4 summarizes the characteristics of the of $^{99}Tc$ and $NO_3^-$ breakthrough curves providing information on the time to first arrival (10 percent of MCL), the arrival time of the MCL, peak concentration and mean concentrations at the water table and receptor. In the current conceptualization, the hypothetical barriers were assumed to extend to the boundary of the simulation domain so as to avoid issues related to the design and performance of side slopes on above grade covers. For $^{99}Tc$, simulation results show the arrival of the MCL at the receptor occurs in year 2660 for a 0.5 mm $yr^{-1}$ barrier; in year 2740 for the 0.1 mm $yr^{-1}$ barrier and not much later in year 2761 for the 0.0 mm $yr^{-1}$ barrier. With the 0.5 mm $yr^{-1}$ barrier, the peak concentration of 458 pCi $L^{-1}$ arrived at the water table in the year 5975. The relatively early arrivals even with barriers is due to the combined effects of plume depth and the recharge rate assumed to exist until the assumed barrier deployment in 2012. A significant amount of water in the profile would have to redistribute before the full effects of the barrier were felt. Another unknown but very important factor is the extent of lateral spreading. The current model assumes a maximum spatial continuity of 100 m, which could easily be an under-estimation of the actual degree of spreading. A more accurate assessment would require additional characterization data.

The $NO_3^-$ plume shows similar behavior. The first arrival occurred in year 2263 under the 0.5 mm $yr^{-1}$ barrier; in year 2266.29 for the 0.1 mm $yr^{-1}$ barrier and 2266.86 for the 0.0 mm $yr^{-1}$ barrier. Peak concentrations occurred significantly later. Neither the 0.1 mm $yr^{-1}$ barrier nor the 0.0 mm $yr^{-1}$ barrier resulted in peak concentrations reaching the water table even after the year 12005. However, the peak in water flux from the antecedent moisture was discernable bringing the peak concentrations significantly less than the MCLs to the receptor (Table 5.4, ). These results are consistent with the 1-D simulations in which the existing plume was allowed to migrate under steady flow to the water table.

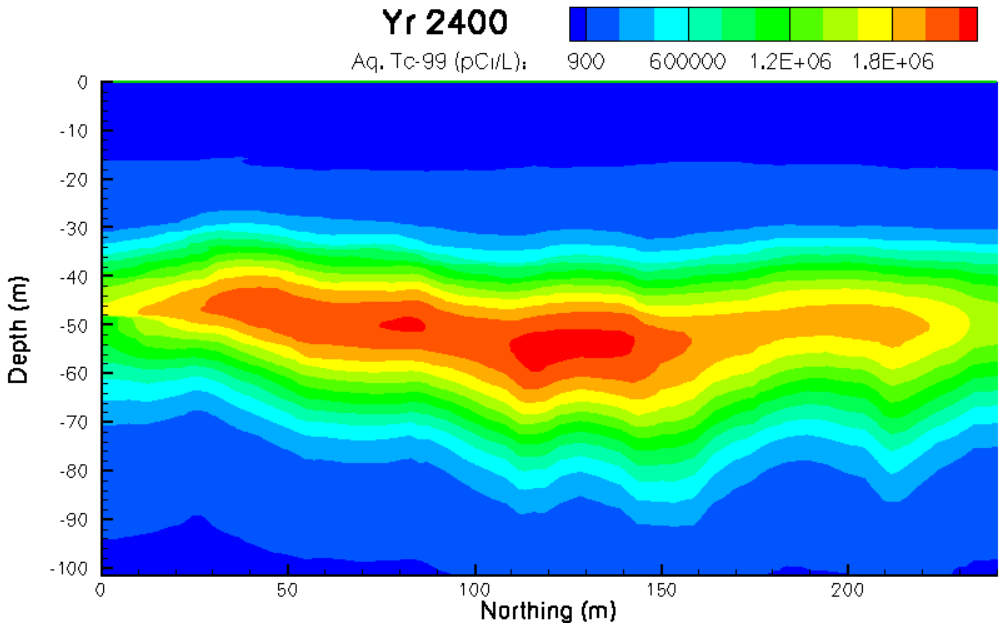


**Figure 5.34. Calculated Distributions of Aqueous $^{99}$Tc in the Year 2400 (0.5 mm/yr)**

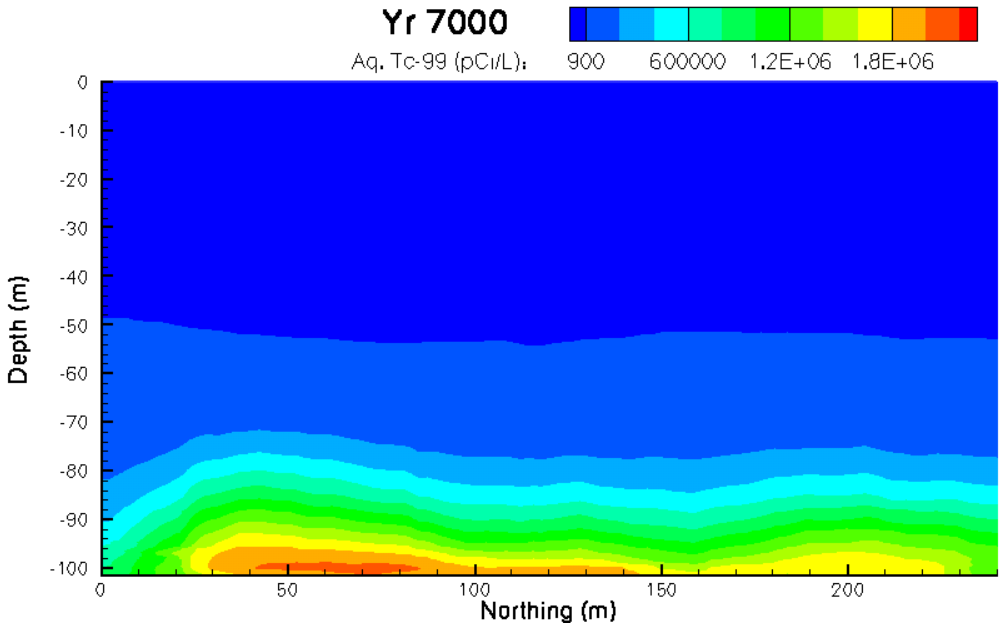


**Figure 5.35. Calculated Distributions of Aqueous $^{99}$Tc in the Year 7000 (0.1 mm/yr)**

**Table 5.4. Predicted Arrival Times and Concentrations for $^{99}Tc$ at Compliance Points**

| Point of Compliance | Solute | Recharge Rate (mm/yr) | First Arrival (yr) | MCL Arrival Time (yr) | Peak Arrival Time (yr) | Peak Concentration (pCi/L) | Mean Arrival Time (yr) |
|---|---|---|---|---|---|---|---|
| Receptor Well | $Tc^{99}$ | 25.0 | 2118.67 | 2142.46 | 2228.50 | 2.09E+04 | 2227.24 |
| | $Tc^{99}$ | 3.5 | 2353.67 | 2600.40 | 2991.50 | 3.15E+03 | 2977.98 |
| | $Tc^{99}$ | 0.5 | 2660.19 | NA | 5975.00 | 4.58E+02 | 5857.26 |
| | $Tc^{99}$ | 0.1 | 2740.01 | NA | 3573.00 | 1.15E+02 | 7034.05 |
| | $Tc^{99}$ | 0.0 | 2761.24 | NA | 3441.00 | 1.09E+02 | >8000.00 |
| Water Table | $Tc^{99}$ | 25.0 | 2095.13 | 2113.36 | 2228.31 | 3.68E+05 | 2228 |
| | $Tc^{99}$ | 3.5 | 2127.68 | 2199.60 | 2991.31 | 3.83E+05 | 2991 |
| | $Tc^{99}$ | 0.5 | 2128.40 | 2205.42 | 5974.30 | 3.88E+05 | 5974 |
| | $Tc^{99}$ | 0.1 | 2129.02 | 2206.46 | >12005 | 3.84E+05 | >8000 |
| | $Tc^{99}$ | 0.0 | 2129.05 | 2206.59 | >12005 | 4.11E+05 | >8000 |

NA—not achieved by the end of the simulation.

**Table 5.5. Predicted Arrival Times and Concentrations for $NO_3^-$ at Compliance Points**

| Point of Compliance | Solute | Recharge Rate (mm/yr) | First Arrival (yr) | MCL Arrival Time (yr) | Peak Arrival Time (yr) | Peak Concentration (mg/g) | Mean Arrival Time (yr) |
|---|---|---|---|---|---|---|---|
| Receptor Well | $NO_3^-$ | 25.0 | 2105.77 | 2125.80 | 2228.50 | 1.09E+03 | 2227.23 |
| | $NO_3^-$ | 3.5 | 2237.17 | 2420.39 | 2991.50 | 1.65E+02 | 2978.11 |
| | $NO_3^-$ | 0.5 | 2263.83 | 3640.35 | 5982.00 | 2.43E+01 | 5865.82 |
| | $NO_3^-$ | 0.1 | 2266.29 | NA | 3590.50 | 6.02E+00 | 7062.64 |
| | $NO_3^-$ | 0.0 | 2266.86 | NA | 3453.50 | 5.74E+00 | >8000.00 |
| Water Table | $NO_3^-$ | 25.0 | 2084.37 | 2100.97 | 2228.31 | 1.93E+04 | 2227.24 |
| | $NO_3^-$ | 3.5 | 2100.12 | 2146.82 | 2991.31 | 2.01E+04 | 2977.98 |
| | $NO_3^-$ | 0.5 | 2100.59 | 2148.88 | 5982.31 | 2.06E+04 | 5857.26 |
| | $NO_3^-$ | 0.1 | 2100.64 | 2149.07 | >12005 | 2.07E+04 | 7034.26 |
| | $NO_3^-$ | 0.0 | 2100.65 | 2149.12 | >12005 | 2.22E+04 | >8000 |

NA—not achieved by the end of the simulation.

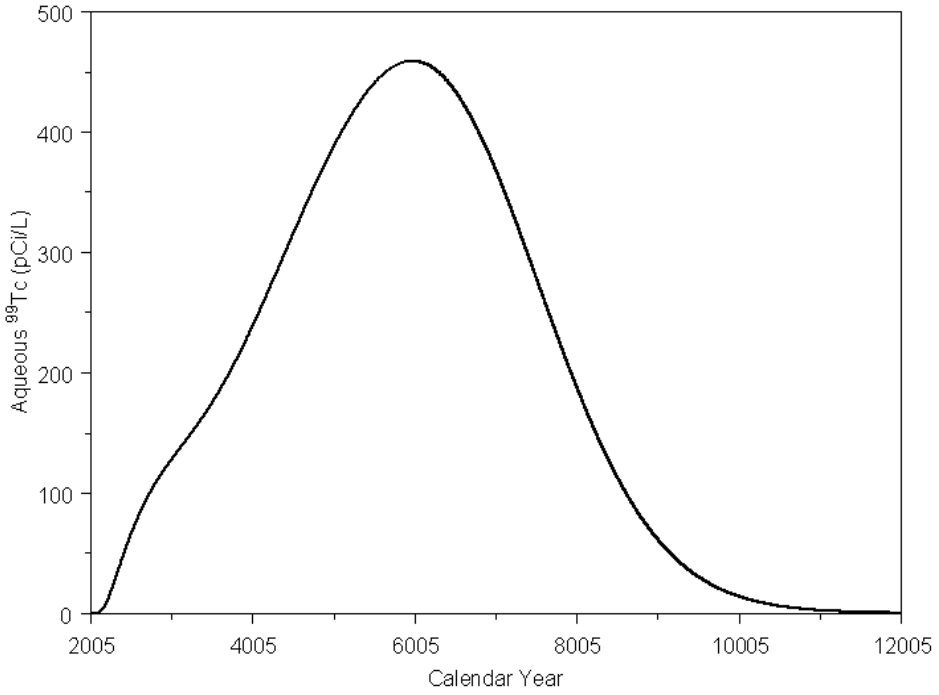


**Figure 5.36. Calculated Distributions for $^{99}$Tc at a Hypothetical Receptor well Under a Recharge Rate of 0.5 mm/yr Based on STOMP Simulations**

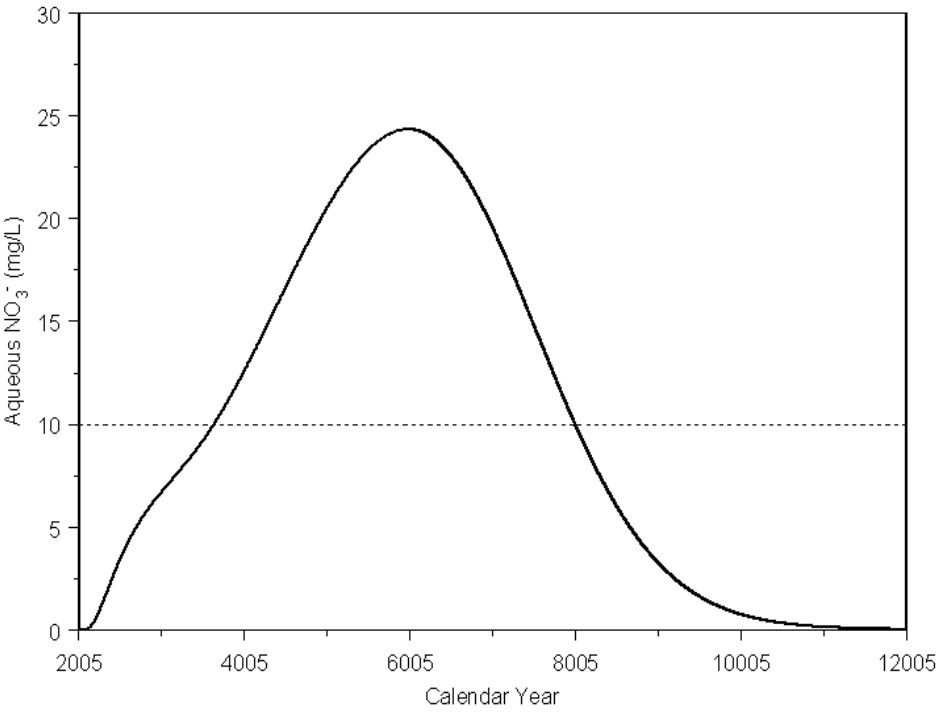


**Figure 5.37. Calculated Distributions for $NO_3^-$ at a Hypothetical Receptor well Under a Recharge Rate of 0.5 mm/yr Based on STOMP Simulations. The dotted line is the MCL of 10 mg/L.**

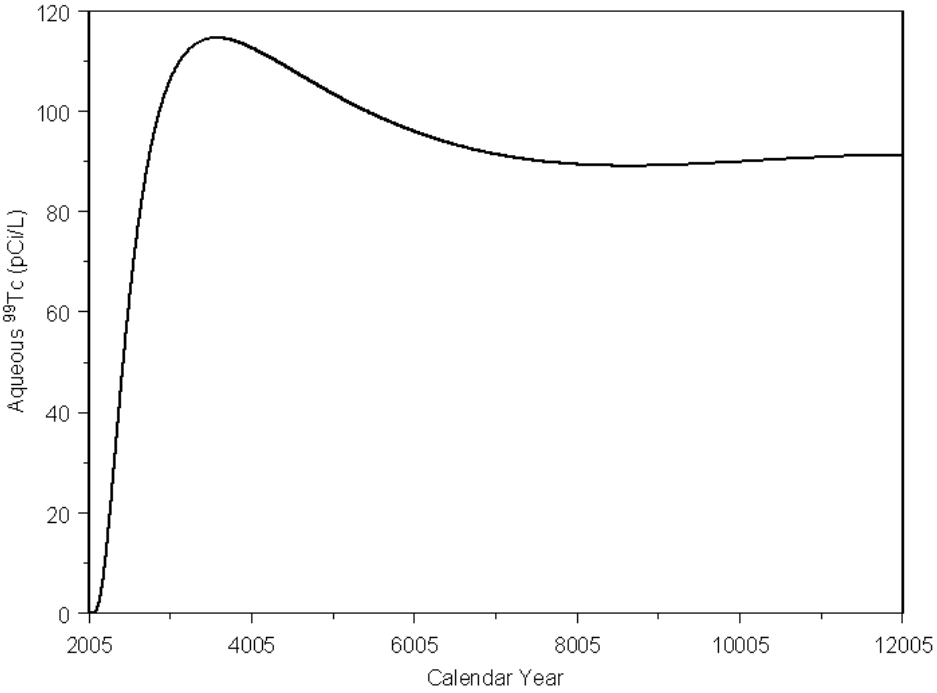


**Figure 5.38. Calculated Distributions for $^{99}Tc$ at a Hypothetical Receptor well Under a Recharge Rate of 0.1 mm/yr Based on STOMP Simulations**

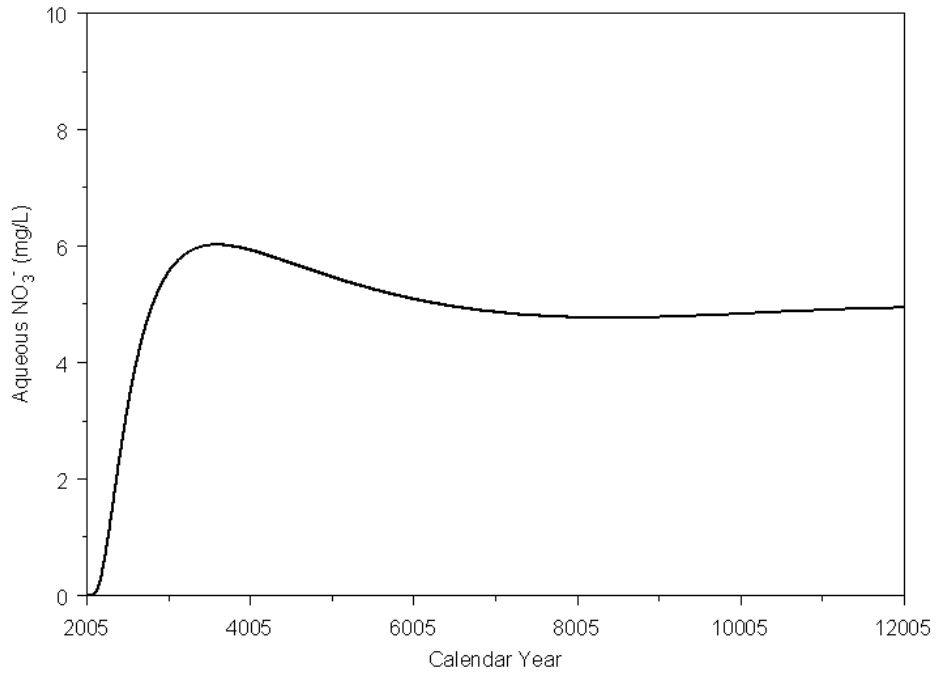


**Figure 5.39. Calculated Distributions for $NO_3^-$ at a Hypothetical Receptor well Under a Recharge Rate of 0.1 mm/yr Based on STOMP Simulations**

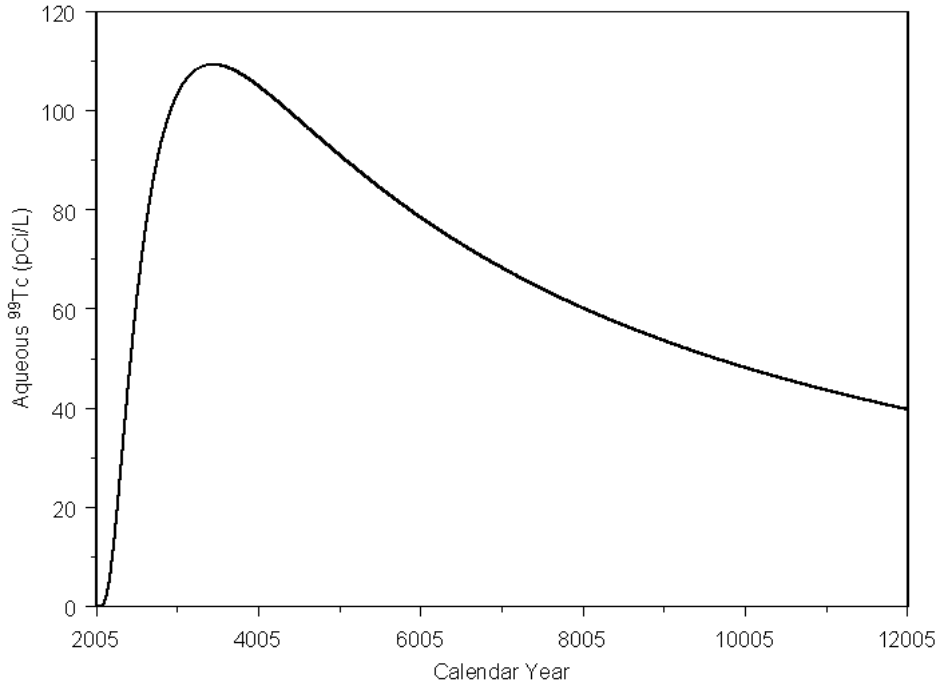


**Figure 5.40. Calculated Distributions for $^{99}Tc$ at a Hypothetical Receptor well Under a Recharge Rate of 0.0 mm/yr Based on STOMP Simulations**

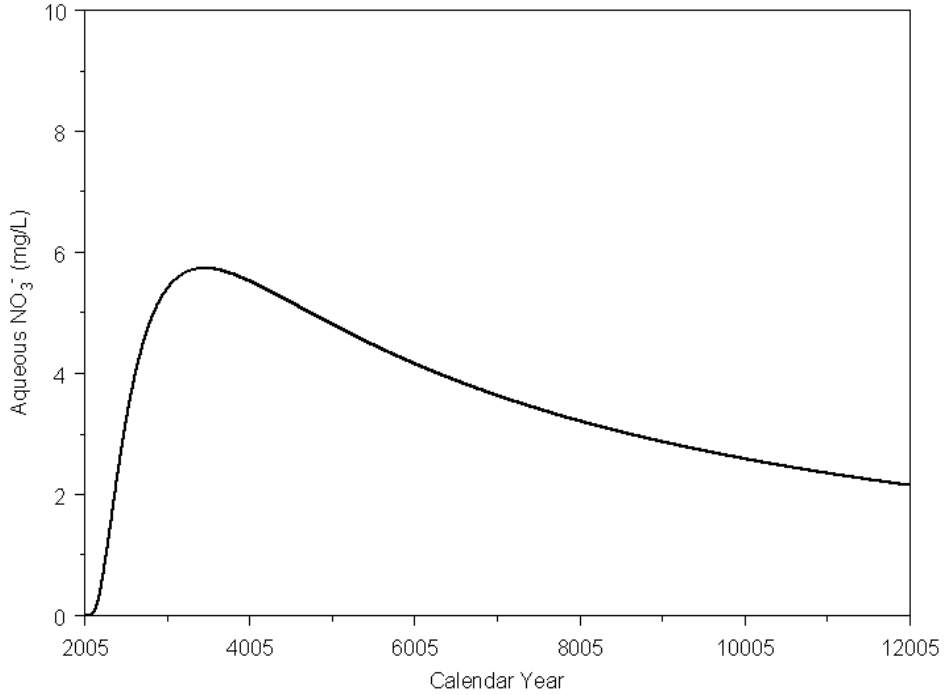


**Figure 5.41. Calculated Distributions for $NO_3^-$ at a Hypothetical Receptor well Under a Recharge Rate of 0.0 mm/yr Based on STOMP Simulations**

Owing to the large inventory of $^{99}Tc$ and $NO_3^-$; the high mobility of the two contaminants; and the long half life of $^{99}Tc$, the no action case would not remove the threat to groundwater and would be less desirable than capping. Based on the foregoing analyses, capping would significantly delay the arrival of mobile contaminants at the water table but leachate concentrations reaching the water table would be in excess of the MCLs. However, application of the soil screening level (SSL) analysis and calculation of dilution attenuation factors for the different recharge rates show that all of the capping alternatives would reduce concentrations of $NO_3^-$ and $^{99}Tc$ at a receptor well to levels significantly below their MCLs. Both modeling approaches show consistency in the results.

# 6.0 Summary and Conclusions

The possibilities and advantages of simulating the fate and transport of mobile contaminants at the BC trench site to aid in the selection of remedial options have been demonstrated using two approaches. The different approaches were used to evaluate two remedial alternatives to determine whether a given alternative eliminated, reduced, or controlled threats to the groundwater, thereby providing protection of human health and the environment over time. The options chosen for comparison were the no-action alternative, in which the site is left in its current state, and a capping alternative, in which caps of different degrees of robustness were compared. In this study, we analyzed the impact of hypothetical caps offering varying degrees of protection. Simulated caps limited recharge to 0.5 mm $yr^{-1}$, 0.1 mm $yr^{-1}$ and 0.0 mm $yr^{-1}$ and were all assumed to be installed in the year 2102. All of the simulations ignored cap degradation, failure, any contribution of side slopes to peripheral recharge.

The first approach, based on a simple analytical convolution solution to the convective-dispersive equation, assumed steady flow and allowed for spatially averaged water content or one that varied with depth to calculate the pore water velocity. Fitting of field sampling data to the model produced excellent results, and the fitted parameters were used to predict the redistribution of the existing contaminant inventory over time under the different remedial options. Using this approach to analyze the impact of surface barriers demonstrated the dramatic impact that surface barriers could have on arrival times. Based on the 1-D convolution model, all of the capping alternatives were superior to the no-action alternatives, significantly delaying arrival times at a compliance point and reducing concentrations to values below the MCLs.

The limitations of applying a 1-D steady-flow analysis to an inherently 3-D transient problem were recognized. Thus, in the second approach the comparison of the remedial alternatives was repeated for transient flow in a multidimensional domain using the STOMP simulator. Transient water flow was simulated based on the Richards' equation with gravity and capillary potential gradients while transport was described by the convective-dispersive equation with a linear-distribution coefficient. Initial conditions were established by allowing the pressure head to reach equilibrium conditions under a constant flux of 3.5 mm $yr^{-1}$ up to the year 1956. Initial contaminant concentrations were assumed to be zero, and the plume distribution at the time of characterization in December 2003 was first simulated. The resulting plume was then exposed to different remedial actions to control recharge, and its remobilization was examined.

Unlike previous analyses in which small-scale stratigraphic changes are ignored, the mobile species ($^{99}Tc$ and $NO_3^-$) moved laterally with the water and remained high above the water table, even after 47 years in the ground. STOMP simulations show significant movement of water and contaminants to the south the 216-B-28. Antecedent moisture from the soil column was pushed ahead by the waste water discharges but contained no contaminants. Results show a strong dependence of the structure of subsurface flow networks on recharge rate and saturation with lateral flow dominating under certain conditions. Results also suggest that some regions of the porous medium that were accessible during the initial high-flux discharges may have become relatively inaccessible as desaturation occurred. These regions may again become accessible to infiltrating water only if saturations and fluxes similar to those at the time of trench operations reoccur. This appears unlikely under current and expected recharge scenarios. This combination of factors may explain why $^{99}Tc$, almost 50 years after being discharged to the shallow

subsurface, is still over 50 m above the water table. Model predictions of the current plume distribution were remarkably similar to field observations. The predicted peak concentration under 216-B-26 was less than 20 percent higher than the peak observed in C4191 samples. The discharges from the multiple trenches appear to have commingled to form a single plume in zone between 20 and 50 m. This is also similar to the observed zone 25 to 50 m zone of contamination observed in the C4191 borehole. Having successfully predicted the current location of the plume, the STOMP model was used to predict its behavior under the two remedial alternatives.

All of the hypothetical caps significantly delayed first arrival, arrival of the MCL and arrival of the peak when compared to no-action alternative. Although leachate concentrations were in excess of the MCls, soil screening levels and calculated concentrations at a hypothetical receptor located 100 m down gradient show that drinking water standards would be protected. First arrival and arrival of the MCLs were identifiable for all the caps. However, in spite of running the model out to year 12005, peak concentrations for the 0.1 and 0.0 mm $yr^{-1}$ barriers were indeterminable. In general, the results of the 1-D convolution solution were in agreement with the STOMP simulations. However, it would have been impossible to make independent predictions of the current inventory distribution based using this approach. Thus, the 1-D convolution approach may be most useful at sites with characterization data that allows estimation of the extent of lateral spreading or that provides information on the distribution of the contaminant inventory. Alternatively, the potential impact of lateral spreading could be obtained from characterized sites with similar depositional environments or by characterizing the spatial correlation structure of the site of interest. Both approaches confirm on-site capping to be an effective technology for increasing the residence time of mobile contaminants in the vadose zone. Undoubtedly, all of the capping alternatives delayed the arrival times of $^{99}Tc$ and $NO_3^-$ at the water table significantly beyond those predicted for the no-action alternatives. In this regard, capping is the superior alternative offering protection to human health and the environment simply by increasing the residence time for $^{99}Tc$ and $NO_3^-$ in the vadose zone.

Based on the foregoing analyses and the comparison of projected concentrations of mobile contaminants reaching the water table no-action alternatives would fail to reduce contaminant concentrations to soil screening levels. Consequently, concentrations reaching a receptor 100 m down gradient of the waste site would exceed the MCLs and the no-action alternative would fail to eliminate the threat to groundwater. Owing to the large inventory of $^{99}Tc$ and $NO_3^-$, the high mobility of the two contaminants, and the long half life of $^{99}Tc$, additional measures would therefore be required to meet the appropriate screening levels or to further increase residence time. The capping alternatives would be successful in removing this threat though an increase in the residence time and a reduction in mass flux. As a result concentrations reaching the receptor would fall below the MCLs with all of the capping alternatives.

# 7.0 References


Bear J. 1972. *Dynamics of fluids in porous media.* American Elsevier, NY.

Beven KJ, DE Henderson, and AD Reeves. 1993. "Dispersion parameters for undisturbed partially saturated soil." *J. Hydrol.* 143:19-43.

Bramley R, and X Wang. 1995. *SPLIB: A Library of Iterative Methods for Sparse Linear Systems*. Indiana University, Bloomington.

Brooks RH, and AT Corey. 1964. "Hydraulic properties of porous media." *Hydrol. Pap. 3*, Colorado State University, Fort Collins, CO.

Bruch JC. 1970. "Two-dimensional dispersion experiments in a porous medium." *Water Resour. Res.* 6(3):791-800.

Burnett RD, and EO Frind. 1987. "Simulation of contaminant transport in three dimensions 2. Dimensionalty effects." *Water Resour. Res.* 23(4):675-705.

Campbell GS. 1974. "A simple method for determining unsaturated conductivity from moisture retention data." *Soil Sci.* 117:311-314.

Cantrell KJ, RJ Serne, and GV Last. 2003. *Hanford Contaminant Distribution Coefficient Database and User's Guide*. PNNL-13895, Rev. 1, Pacific Northwest Laboratory, Richland, WA.

Carsel, RF. and RS. Parrish. 1988. "Developing joint probability distributions for soil water retention characteristics." *Water Resour. Res.* 24:775-769.

Connelly MP, BH Ford, and JV Borghese. 1992. *Hydrogeologic Model for the 200 West Groundwater Aggregate Area*. WHC-SD-EN-TI-014, Rev 0, Westinghouse Hanford Company, Richland, WA.

Deutsch CV, and AG Journel. 1998. *GSLIB: Geostatistical Software Library and User's Guide.* 2nd ed., Oxford University Press, NY.

Domenico PA, and GA Robbins. 1984. "A dispersion scale effect in model calibrations and field tracer experiments." *J. Hydrol.* 70:123-132.

Elrick DE, MI Sheppard, A Mermoud, and T Monnier. 1997. "An analysis of surface accumulation of previously distributed chemicals during steady-sate evaporation." *J. Environ. Qual.* 26:883-888.

Fayer MJ, and TB Walters. 1995. *Estimated Recharge Rates at the Hanford Site*. PNL-10285, Pacific Northwest Laboratory, Richland, WA.

Fayer MJ, and JE Szecsody. 2004. *Recharge Data Package for the 2005 Integrated Disposal Facility Performance Assessment*. PNNL-14744, Pacific Northwest Laboratory, Richland, WA.

Fecht KR, GV Last, and MC Marratt. 1978. *Granulometric Data 216-B and C Crib Facilities Monitoring Well Sediments*. RHO-LD-45, Rockwell Hanford Operations, Richland, WA.

Francis AJ, CJ Dodge, and GE Meinken. 2002. "Biotransformation of pertechnetate by Clostridia." *Radiochim. Acta.* 90:791-797.

Gee GW, MK Rockhold, and JL Downs. 1988. *Status of the FY 1988 Soil-water Balance Studies on the Hanford Site.* PNL-6750, Pacific Northwest Laboratory, Richland, WA.

Haines R I, DG Owens, and TT Vandegraaf. 1987. "Technetium-iron oxide reactions under anaerobic conditions: a Fourier transform infrared, FTIR study." *Nucl. J. Can.* 1:32-37.

Hammel K, J Gross, G Wessolek, and K Roth. 1999. "Two-dimensional simulation of bromide transport in a heterogeneous field soil with transient unsaturated flow." *Euro. J. Soil Sci.* 50:633-647.

Harlem DRF, and RR Rumer. 1963. "Longitudinal and lateral dispersion in an isotropic porous medium." *Fluid Mech.* 16:385-394.

Haney, W.A. and J.F. Honsted. 1958. *A History and Discussion of Specific Retention Disposal of Radioactive Liquid Wastes in the 200-Areas.* HW-54599, Hanford Atomic Products Operation, Richland, WA.

Hartman MJ, LF Morasch, and WE Webber. 2004. *Hanford Site Groundwater Monitoring for Fiscal Year 2003*. PNNL-14548, Pacific Northwest National Laboratory, Richland, WA.

Jury WE, and K Roth. 1990. *Transfer functions and solute movement through soil: Theory and applications.* Birkhauser Verlag, Basel.

Kellogg WW, RD Cadle, ER Allen. 1972. "The sulfur cycle." *Science* 175:587-596.

Kemper WD. 1986. *Solute Diffusivity in Methods of Soil Analysis, Part 1.* Ed. A Klute, pp. 1007-1024. American Society of Agronomy, Madison, WI.

Khaleel R, and EJ Freeman. 1995. *Variability and scaling of hydraulic properties for 200 Area soil,Hanford Site.WHC-EP-0883* Westinghouse Hanford Company, Richland, Washington.

Kincaid CT, MP Bergeron, CR Cole, MD Freshley, NL Hassig, VG Johnson, DI Kaplan, RJ Serne, GP Streile, DL Strenge, PD Thorne, LW Vail, GA Whyatt, and SK Wurstner. 1998. *Composite Analysis for Low-Level Waste Disposal in the 200-Area Plateau of the Hanford Site.* PNNL-11800, Pacific Northwest National Laboratory, Richland, WA.

Kramer JH, SJ Cullen, and LG Everett. 1995. "Vadose zone monitoring with the neutron probe." In: *Handbook of Vadose Zone Characterization and Monitoring*. LG Wilson, LG Everett, and SJ Cullen, Editors, Geraghty & Miller Environmental Science and Engineering Series.

Last, G. V., E. J. Freeman, K. J. Cantrell, M. J. Fayer, G. W. Gee, W. E. Nichols, B. N. Bjornstad, and D. G. Horton. 2004. *Vadose Zone Hydrogeology Data Package for the 2004 Composite Analysis*. PNNL-14702. Pacific Northwest National Laboratory, Richland, Washington.

Leij FJ, TH Skaggs, and MTh van Genuchten. 1991. "Analytical Solutions For Solute Transport In 3-Dimensional Semi-Infinite Porous-Media." *Water Resour. Res.* 27:2719-2733.

Lieser KH, and C Bauscher. 1987. "Technetium in the hydrosphere and in the geosphere. I. Chemistry of technetium and iron in natural waters and influence of the redox potential on the sorption of technetium." *Radiochim. Acta.* 42:205-213.

Liu CL, SS Li, XY Wang, ZM Wang, CT Xin, HF Wang, RJ Li, B Li, LT Tang, and L Jiang. 2001. "Migration of $^{99}$Tc in unsaturated Chinese loess under artificial rainfall condition: an *in situ* test.." *Radiochim. Acta*. 89:643-645.

Marshall E. 1987. "Hanford's Radioactive Tumbleweed." *Science* 236:1616-1620.

Meyer RE, WD Arnold, FI Case, and GD O'Kelly. 1991. "Solubilities of Tc(IV) oxides." *Radiochim. Acta.* 55:11-18.

Millington RJ, and JP Quirk. 1961. "Permeability of Porous Media." *Nature* 183:387-388.

Perfect E, MC Sukop, and GR Haszler. 2002. "Prediction of dispersivity for undisturbed soil columns from water retention parameters." *Soil Sic. Soc. Am. J.* 66(3):696-701 MAY-JUN 2002.

Prych EA. 1998. *Using Chloride and Chlorine-36 as Soil-Water Tracers to Estimate Deep-Percolation at Selected Locations on the U.S. Department of Energy Hanford Site, Washington*. Open File Report 94-514, U.S. Geological Survey, Tacoma, WA.

Rawls, WJ, DL Brakensiek, and KE Saxton. 1982 "Estimating soil water retention from soil physical properties and characteristics." *Adv. Soil Sci.* 16:213-234.

Reidel, S. P., and D. G. Horton. 1999. *Geologic Data Package for 2001 Immobilized Low-Activity Waste Performance Assessment. PNNL-12257,* Rev. 1., Pacific Northwest National Laboratory, Richland, Washington

Runnells DD. 1995. "Basic Contaminant Fate and Transport Processes in the Vadose Zone-Inorganics." In: *Handbook of Vadose Zone Characterization and Monitoring*. LG Wilson, LG Everett, and SJ Cullen, Editors, Geraghty & Miller Environmental Science and Engineering Series.

Saiers JE, and GM Hornberger. 1996. "Migration of cesium through quartz sand." *J. Contam. Hydrol.* 163: 271-288.

Schoen R, JP Gaudet, and DE Elrick. 1999. "Modeling of solute transport in a large undisturbed lysimeters during steady-state water flux." *J. Hydrol.* 215:82-93.

Schroeder NC, D Morgan, DJ Rokop, and J Fabryka-Martin. 1993. "Migration of technetium-99 in the alluvial aquifer at the Nevada Test Site, Nevada, USA." *Radiochim. Acta* 60:203-209.

Serne, RJ and FM Mann 2004. *Preliminary Data From 216-B-26 Borehole in BC Cribs Area*. RPP-20303, Rev. 0. CH2MHill Group, Richland, Washington.

Simpson BC, RA Corbin, and SF Agnew. 2001. *Hanford Soil Inventory Model*. BHI-01496 Rev 0 (also LA-UR-00-4050), Bechtel Hanford Inc., Richland, WA.

Sparks DL. 1989. Kinetics of Soil Chemical Processes. Academic Press, NY.

U.S. Department of Energy-Richland Operations (DOE-RL). 1998. *Groundwater/Vadose Zone Integration Project Background Information and State of Knowledge.* DOE/RL-98-48 Vol. II Rev. 0, Richland, WA.

U.S. Environmental Protection Agency (EPA). 1996. *Soil Screening Guidance: Technical Background Document.* EPA/540/R-95/128, Washington D.C.

U.S. Environmental Protection Agency (EPA). 2000. *Soil Screening Guidance for Radionuclides: Technical Background Document.* EPA/540-R-00-006, Washington D.C.

van Genuchten MTh, and WJ Alves. 1982. *Analytical solutions of the one-dimensional convective-dispersive solute transport equation*. USDA ARS Technical Bulletin Number 1661. U.S. Salinity Laboratory, 4500 Glenwood Drive, Riverside, CA.

Ward AL, GW Gee, and MD White. 1997. *A Comprehensive Analysis of Contaminant Transport in the Vadose Zone Beneath Tank SX-109.* PNNL-11463, Pacific Northwest National Laboratory, Richland, WA.

Ward AL, GW Gee, ZF Zhang, and JM Keller. 2002. *Vadose Zone Transport Field Study: FY 2002 Status Report.* PNNL 14180, Pacific Northwest National Laboratory, Richland, WA.

White MD, and M Oostrom. 2000. *STOMP Subsurface Transport Over Multiple Phases, Version 2.0, User's Guide.* PNNL-12034, Pacific Northwest National Laboratory, Richland, WA.

Yanagisawa K, and Y Muramatsu. 1993. "Transfer factors of technetium from soil to vegetables." *Radiochim. Acta* 63:83-86.

Zhuang HE, JS Zeng, and LY Zhu. 1988. "Sorption of radionuclides technetium and iodine on minerals. *Radiochim. Acta* 44/45:143-145.

Zhaung HE, JS Zheng, DY Xia, and ZG Zhu. 1995. "Retardation of technetium and iodine by antimony- and mercury-containing minerals." *Radiochim. Acta* 68:245-249.

# Distribution

**No. of Copies**

**ONSITE**

7 Fluor Hanford
- M. E. Todd (2) E6-35
- M. W. Benecke (5) E6-35

10 Pacific Northwest National Laboratory
- A. L. Ward (5) K9-33
- F. Zhang (1) K9-33
- G. W. Gee (1) K9-33
- J. M. Keller (1) K9-36
- Information Release (2)